LIQUID PHASE SINTERING OF TUNGSTEN-NICKEL-COBALT HEAVY ALLOYS

A THESIS SUBMITTED TO
THE GRADUATE SCHOOL OF NATURAL AND APPLIED SCIENCES
OF
MIDDLE EAST TECHNICAL UNIVERSITY

BY

ONUR DİNÇER

IN PARTIAL FULLFILLMENT OF THE REQUIREMENTS
FOR
THE DEGREE OF MASTER OF SCIENCE
IN
METALLURGICAL AND MATERIALS ENGINEERING

JANUARY 2014

Approval of the thesis:

LIQUID PHASE SINTERING OF TUNGSTEN-NICKEL-COBALT HEAVY ALLOYS

Submitted by **ONUR DİNÇER** in partial fulfillment of the requirements for the degree of **Master of Science in Metallurgical and Materials Engineering Department**, **Middle East Technical University** by,

Prof. Dr. Canan ÖZGEN
Dean, Graduate School of **Natural and Applied Sciences** ______________

Prof. Dr. C. Hakan GÜR
Head of Department, **Metallurgical and Materials Engineering** ______________

Prof. Dr. Ali KALKANLI
Supervisor, **Metallurgical and Materials Engineering Dept., METU** ______________

Prof. Dr. İshak KARAKAYA
Co-Supervisor, **Metallurgical and Materials Engineering Dept., METU** ______

Examining Committee Members:

Prof. Dr. İshak KARAKAYA
Metallurgical and Materials Engineering Dept., METU ______________________

Prof. Dr. Ali KALKANLI
Metallurgical and Materials Engineering Dept., METU ______________________

Assoc. Prof. Dr. Arcan F. DERİCİOĞLU
Metallurgical and Materials Engineering Dept., METU ______________________

Assist. Prof. Dr. Merve ERDAL ERDOĞMUŞ
Mechanical Engineering Dept., METU ______________________

Assist. Prof. Dr. Bilge İMER
Metallurgical and Materials Engineering Dept., METU ______________________

Date: **13.01.2014**

I hereby declare that all information in this document has been obtained and presented in accordance with academic rules and ethical conduct. I also declare that, as required by these rules and conduct, I have fully cited and referenced all material and results that are not original to this work.

Name, Last name : Onur DİNÇER

Signature :

ABSTRACT

LIQUID PHASE SINTERING OF TUNGSTEN-NICKEL-COBALT HEAVY ALLOYS

DİNÇER, Onur
M. Sc., Metallurgical and Materials Engineering
Supervisor: Prof. Dr. Ali KALKANLI
Co-Supervisor: Prof. Dr. İshak KARAKAYA

January 2014, 128 pages

The aim of this thesis study was to investigate the effects of composition and sintering variables on the microstructural characteristics of W-rich W-Ni-Co heavy alloys. W-Ni-Co alloys containing 90 to 97 wt% W and different Ni/Co ratios were investigated in the study. The alloys studied were produced by applying conventional powder metallurgy methods and subjected to microstructural and mechanical characterization by using suitable techniques. All of the alloys investigated reached almost full density when sintered at and above 1475 °C, except Co-rich alloys. Co-rich alloys reached full density only when sintered at 1600 °C and could not be densified by liquid phase sintering (LPS) due to the lack of the liquid phase. The microstructures of the Ni-rich alloys were found to consist of rounded, nearly pure W grains and a Ni-Co-W binder matrix phase. A microstructure consisting of nearly pure W grains and a two-phase binder matrix was observed in all of the alloys with Ni/Co ratio 1/1. X-ray diffraction and energy dispersive spectroscopy (EDS) analysis have shown that one phase of the binder matrix of Ni/Co ratio 1/1 alloys was Ni-containing Co_7W_6 and the other phase was a Ni-Co-W solid solution. The binder matrix phase in the Ni-rich alloys was observed to dissolve relatively large amounts of W (up to 43 wt %). EDS line scan analysis showed that W was dissolved in the binder matrix homogenously. For these alloys, in general, the areal percentage of the binder matrix phase was determined to increase with increasing sintering temperature and decreasing alloy W content. In Ni-rich alloys, the average W grain size was found to increase with increasing sintering temperature and alloy W content, when sintered above 1525 °C. Hardness measurements have revealed that the hardness of the alloys with Ni/Co ratio 1/1 was greater than all of the remaining alloys. This beneficial behavior was attributed to the presence of a two-phase binder matrix in these alloys.

Keywords: Tungsten heavy alloys, Cobalt, Liquid phase sintering

ÖZ

TUNGSTEN-NİKEL-KOBALT AĞIR ALAŞIMLARININ SIVI FAZ SİNTERLENMESİ

DİNÇER, Onur
Yüksek Lisans, Metalurji ve Malzeme Mühendisliği Bölümü
Tez Yöneticisi: Prof. Dr. Ali KALKANLI
Ortak Tez Yönetici: Prof. Dr. İshak KARAKAYA

Ocak 2014, 128 Sayfa

Bu yüksek lisans tezinin amacı, kompozisyon ve sinterleme sıcaklığının W-yoğun W-Ni-Co alaşımlarının mikroyapısal özellikleri üzerine etkilerinin incelenmesidir. Bu çalışmada ağırlıkça % 90 ve 97 arasında W içeren ve farklı Ni/Co oranlarına sahip W-Ni-Co alaşımları araştırılmıştır. Bu alaşımlar geleneksel toz metalurjisi yöntemleri kullanılarak hazırlanmıştır. Hazırlanan numunelerin mikroyapısı ve bazı mekanik özellikleri uygun karakterizasyon yöntemleri kullanılarak incelenmiştir. Numuneler 1475°C üzeri sıcaklıklarda, Co-yoğun alaşımlar hariç, hemen hemen tam yoğunluğa ulaşmıştır. Co-yoğun alaşımlar sadece 1600°C'de tam yoğunluğa ulaşmış ve bu sıcaklık altında bu alaşımlarda sıvı faz sinterlenmesi görülmemiştir. Ni-yoğun alaşımlar içyapılarında yuvarlanmış, saf W taneleri ve Ni-Co-W içerikli bir bağlayıcı matris faz içermektedirler. Ni/Co oranı 1/1 olan alaşımlar ise saf W tanelerinin yanı sıra çift fazlı bir bağlayıcı matrise sahiptir. X-ışını kırınım ve enerji dağılım spektroskopi (EDS) analizleri Ni/Co oranı 1/1 olan alaşımların bağlayıcı fazlarından birinin Ni-içeren Co_7W_6, diğerinin ise Ni-Co-W katı çözeltisi olduğunu göstermiştir. Ni-yoğun numuneler bağlayıcı matrislerinde yüksek miktarda (ağırlıkça % 43' e kadar) W çözmektedir. EDS çizgi tarama yöntemi ile yapılan analiz, W' nin bağlayıcı matris içerisinde homojen bir şekilde çözündüğünü göstermektedir. Bu alaşımlarda, genel olarak, bağlayıcı matris faz alanı yüzdesi sinterleme sıcaklığının artması ile artmakta ve W miktarının artması ile düşmektedir. Ni-yoğun alaşımlarda ortalama W tane boyu, 1525°C üzerinde, sinterleme sıcaklığı ve W miktarı ile artmaktadır. Ni/Co oranı 1/1 olan tüm alaşımlar diğerlerine göre daha yüksek sertlik değerine sahiptir. Bu durumun sebebinin Ni/Co oranı 1/1 olan alaşımların çift fazlı bir bağlayıcı matrise sahip olmasından kaynaklandığı değerlendirilmektedir.

Anahtar Kelimeler: Tungsten Ağır Alaşımlar, Kobalt, Sıvı Faz Sinterleme

To My Wife
And
Our Beloved Families

ACKNOWLEDGEMENTS

I would like to express my gratitude to Prof. Dr. Ali KALKANLI, Prof. Dr. İshak KARAKAYA and Dr. M. Kaan PEHLİVANOĞLU for their guidance, advice, criticism, encouragement and insight throughout the completion of the thesis.

I am indebted to all of my friends and colleagues, especially, Dr. N. Kaan ÇALIŞKAN, İlker ATİK, Hakan DER, Önder SOYER, Egemen VARLI, Mustafa AKTAŞ, Fatih KOCA and Levent KUTLUCAN for their support and encouragements. I am also grateful to TÜBİTAK SAGE for the facilities that made my work easier.

I would like to acknowledge the financial and technical support of TÜBİTAK SAGE and its staffs.

Finally, I am grateful to my wife, Ayşe DİNÇER, and our families for their continuous support and encouragements.

TABLE OF CONTENTS

CHAPTERS

APPENDICES

LIST OF FIGURES

FIGURES

LIST OF TABLES

TABLES

CHAPTER 1

INTRODUCTION

Tungsten (W) is a high melting temperature and high density refractory metal, but it has a brittle nature. It is hard to obtain a W product by conventional manufacturing techniques. W can be used in different forms in industrial applications. One of the W forms with additives is tungsten heavy alloys (WHA), which are the combination of high density and ductility in one material. WHAs are typically composite materials, which contain W grains and a relatively low melting point matrix phase in their microstructure. WHAs contain 90 to 98 wt % W in order to increase the density. Mostly, these alloys consist of Ni-Fe, Ni-Cu, Ni-Co, Ni-Co-Fe elemental metallic powder mixes in order to be densified. Generally, WHAs have high strength, high density, and good wear and corrosion resistance. These properties make WHAs a good candidate for radiation shields, counter weight balances, kinetic penetrators, electrical contacts and damping devices.

In order to produce WHAs, Ni and other suitable metals are added to W. It is known that Ni in the composite structure can dissolve up to 40 wt% W in its liquid phase at around 1500°C. As the liquid melt is formed, solid W particles can become rounded due to a decrease in the surface energy. In addition, capillary forces pull W particles closer and bring rearrangement into play as a transport medium for solid W grains. Dissolution of W in the matrix phase enhances the densification of WHA. Liquid formation increases the densification rate of WHA and enables it to reach full density [1]. On the other hand, liquid phase sintering (LPS) of WHA can cause slumping and distortion, which may obstruct the near net shape production benefits. High liquid formation initiates the shape loss and composition and property differences. More than 20 volume percent liquid affects the solid skeleton of W particles and causes solid-liquid segregation.

To produce W and WHAs, many techniques can be used such as arc casting, hot extrusion, hot pressing and powder metallurgy (P/M). P/M is a suitable method for the production of WHAs to obtain near net shaped products and at relatively low temperatures compared to casting. Traditional P/M steps can also be used for producing WHAs. At the beginning, elemental metallic powders were mixed and compacted into required shape. These compacted parts are then sintered under suitable conditions. Generally, liquid phase sintering (LPS) is preferred for the densification of WHAs. Basically, in LPS, relatively low melting temperature metallic additions melt and the liquid formed wets the W particles. This liquid helps W particles to come closer and increase the densification rate.

For many civil and military applications, improved mechanical properties are required. In order to satisfy the required mechanical properties, the production process during LPS should be well controlled. In addition, mechanical properties can be predicted from the microstructure of liquid phase sintered alloys. As can easily be appreciated, the microstructure of sintered WHAs has important effects on the mechanical properties of such alloys. This is one of the reasons why there is a lot of work in the literature on microstructural and mechanical characterization of WHAs. In order to improve the mechanical properties of WHAs, it is very important to understand and describe the microstructural characteristics of such alloys.

The alloy systems W-Ni-Cu, W-Ni-Fe and W-Ni-Co have been developed in chronological order. Consequently, W-Ni-Co is a newer alloy system when compared to other WHAs and studies on microstructural characterization of this alloy system is relatively scarce in the literature. In this work, the effects of composition and sintering variables on the microstructural characteristics of several selected W-Ni-Co alloys have been studied. The alloys investigated were selected from the W-rich part of the W-Ni-Co ternary system. Conventional P/M methods were used to produce the alloy specimens. For the production of the alloy samples, elemental W, Ni and Co metallic powders were first mixed,and cold isostatically pressed, and then sintered at different temperatures under pure hydrogen atmosphere. Characterization studies of the prepared alloys were based on several selected microstructural, physical and mechanical properties. The results of the study were discussed by taking relevant sintering, diffusion and coarsening theories into consideration

In what follows, the results of the thesis study is presented and discussed. A survey of the literature related to the subject is given in Chapter 2. In Chapter 3, the experimental procedure applied and characterization methods used in the study are described. The results obtained were presented and discussed in Chapter 4, and finally, the conclusions drawn from the results of the study are given in Chapter 5. Relevant experimental data that could not be included within the main context of the manuscript is presented in Appendix A to Appendix F.

Hereafter in the manuscript, all alloy compositions will be presented in weight percentages (wt%), unless otherwise stated.

CHAPTER 2

THEORY

2.1 Introduction to Tungsten (W) and Tungsten Based Alloys

Tungsten is a high density, high melting point refractory metal. The name of “tungsten” comes from the Swedish term that means “heavy stone”. Similarly, the chemical symbol of tungsten “W” was assigned based on the German name “Wolfram”. Most of the W ores are mined from China and North America. Tungsten has a large nucleus that consists of 74 protons and 110 neutrons. This is why tungsten metal has high density. Some physical properties of tungsten are shown in Table 1.

Fabrication of pure tungsten has some difficulties due to its brittle characteristics. W can be used in different forms in industrial applications. These forms are carbides, alloys with additions and pure forms.

Table 1 Some Physical Properties of Tungsten

Properties	
Density	19.35 g/cm^3
Crystal Structure	BCC
Melting Point	3410 °C
Poisson’s Ratio at 25°C	0.28
Elastic Modulus	400 GPa

Mostly, W is used in carbide form with addition of cobalt as a binder. The binder makes tungsten carbide densification easier. These cemented carbides are used as cutting tools and in tribological applications. In addition, W is often used in thermocouples, electronic devices and lamp wires. Moreover, owing to its high density and high melting point, W can find wide use for heat and radiation shield applications.

W can also be used in many fields as tungsten heavy alloys. These alloys have compositions ranging between 90 and 98 wt% W balanced with Ni, Co, Fe, Cu and various other additions. Tungsten heavy alloys have high densities ranging from 16.8 to 18.5 g/cm^3. The advantages of these alloys are easy machining, higher mechanical properties, low thermal properties, low thermal expansion and excellent corrosion resistance. Tungsten heavy alloys can be used in a wide range of industries such as:

- Balance weight in devices
- Ordnance applications such as kinetic penetrators and fragments on warheads
- Radiation shields
- Electrical contacts

Typically, tungsten heavy alloys (WHAs) contain 90 to 98 wt % W. To produce WHAs, powder metallurgy has been used mostly. These alloys generally include two phases in their microstructure, namely a binder matrix phase and an almost pure W phase. This composite structure exhibits the compromised properties of both the matrix and W phase. The typical microstructure of a WHA is given in Figure 1.

The composition of WHAs can be adjusted by varying the relative content of W and other additives. In industrial uses, the WHA composition to be chosen depends on the requirement of the particular application. Generally, the primary consideration in adjusting the composition is tailoring the density of WHAs. In these alloys, the density is determined mainly by the varying W composition in the alloy. In Table 2, the variation of the theoretical densities of WHAs with changing W wt % in the alloy are given.

In general, W-based alloys are used in most of the technological applications due to their unique properties. Alloying elements have a significant effect in changing the properties of WHAs. W-Ni-Cu, W-Ni-Fe and W-Ni-Co are the most widely used alloy systems in the production of WHAs.

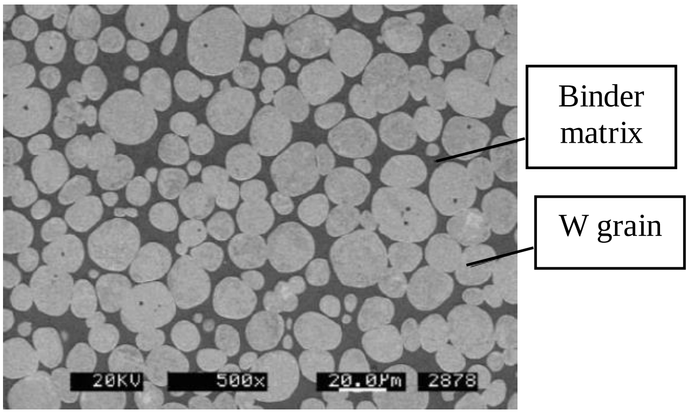

Figure 1 Typical microstructure of WHA [2]

Table 2 Density Variation with Increasing W Content in WHAs

Tungsten Content (wt%)	**Density (g/cm^3)**
90	17.1
92.5	17.6
95	18.1
97	18.6

W-Ni-Cu based alloys are non-magnetic composite structures and show high electrical conductivity. In these alloys, the Ni/Cu ratio in the binder matrix phase ranges between 3/2 and 4/1. Mechanical properties of these alloys are lower than W-Ni-Fe alloys in terms of strength and ductility. On the other hand, W-Ni-Cu alloy system has resistance to most common acids and corrosive atmospheres. In addition, these alloys have high oxidation resistance up to 400°C [3].

W-Ni-Fe based alloys are ferromagnetic. This type of WHAs consists of 1/1 to 4/1 Ni/Fe ratio. Mostly preferred Ni/Fe ratio is 7/3 due to the elimination of intermetallic phases during sintering. Their mechanical properties, namely strength and ductility are high. W-Ni-Fe alloys can be deformed up to 60% without any heat treatment process.

W-Ni-Co based alloys are also ferromagnetic. Mostly preferred Ni/Co ratio is 9/1 and 8/2. These types of WHAs are used when improved mechanical properties are needed. W-Ni-Co alloys have higher strength than W-Ni-Cu and W-Ni-Fe alloys in deformed and heat-treated condition. Based on this phenomenon, W-Ni-Co alloys are mostly used in defense applications.

In WHAs, the selection of the alloy composition is determined by several considerations. Density requirement is the first factor for the choice of a WHA. Other requirements are corrosion resistance, magnetic properties and mechanical characteristics.

2.2 Processing of W Based Alloys

There are several methods that can be applied for the processing of W based alloys such as electron beam melting, arc casting, chemical vapor deposition, hot extrusion and powder metallurgy [3]. In this study, the powder metallurgy technique was used to investigate the W-Ni-Co alloy system and this production method will be explained in detail.

2.2.1 Powder Metallurgy

Powder metallurgy (P/M) can be defined as a near-net or net shape production process that consists of basically shaping and consolidation steps [4]. With P/M, one can fabricate complex, fine featured parts in an economical way. From an engineering point of view, P/M can be defined as the study of processing of metallic powder that comprises production and characterization [5].

P/M is one of the oldest manufacturing methods. It has been known that in Africa and Egypt, P/M methods were used to make “sponge iron” for making tools in 3000 B.C. From these days to now, various products have been manufactured with P/M process. There are lots of examples in which P/M has been used. In the modern era, Coolidge used P/M methods to produce tungsten lamp filaments for Edison. In the beginning of the 19th century, P/M grew as a new production method for copper and iron production with low cost [6]. Nowadays, due to the ability to fabricate high quality parts with narrower tolerances, P/M has become a preferred technique in economic reasons [5]. Briefly, for example; automotive transmission gear parts, armor piercing projectiles, orthopedic implants, machine parts, friction materials and dental amalgams can be produced by P/M methods [5].

Generally, P/M produced near-net shape parts with minimal or non-machining operation can be produced mainly in three steps, as conceptually depicted in Figure 2. Firstly, the characteristics of the powder such as size, shape, morphology, chemistry and purity become a concern. Typically, mixed or blended powders need to be compacted and sintered with conventional P/M routes. In this stage, densification, forming and machining should be controlled in the expected tolerances. Finally, the properties of the final product become important. Density, strength, microstructure etc. affect the final product properties.

P/M production method is preferred to manufacture components, parts etc. mainly for economic reasons. In addition, with P/M, unique properties can be obtained when

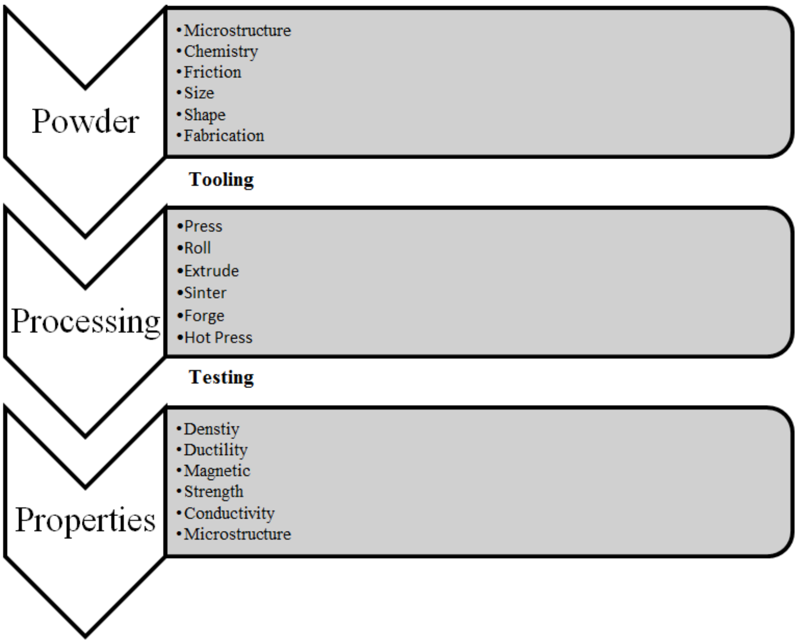

Figure 2 Conceptual flow chart for P/M [5]

compared to casting. Some porous metals, cemented carbides and cermets can be manufactured by P/M to obtain both unique properties and low cost.

In particular, some reactive and refractory metals have to be produced by P/M due to their high melting temperature. It is very hard to produce these materials by conventional manufacturing methods and this is not practical.

The P/M process consists of compacting to the required shape and heating of the powders, as a result of which the powders consolidate into the required shape with improved properties. This manufacturing process can be considered to involve three general steps, which are powder mixing, powder compaction and sintering [3].

2.2.2 Powder Blending and Mixing

During the pre-compaction stage, powders may need to be blended and mixed in order to combine them into a homogenous mass. The general purpose for powder mixing is modifying the powder characteristics for easier processing [5]. Powder blending is generally aimed at achieving a desired particle size distribution. For example, fine and coarse particles may be combined together in order to increase the sintering rate, because compaction of fine particles is harder and coarse particles show poor sintering strength. Also, for producing alloys with homogeneous properties via P/M methods, it may be needed to mix elemental powders. Powders can also be mixed with lubricants in order to decrease die friction during compaction with rigid dies. There are some lubricants used for lubrication of powders such as stearates of Al, Li, Zn and some waxes and cellulose additives [5].

Mixing and blending operation must be done carefully. Otherwise, the mixed powder can segregate and undesirable composition fluctuations may be encountered. The type of the material to be mixed, mixer type, mixing speed and time and container size and shape are some of the variables that must be taken into consideration for a successful mixing and blending operation.

2.2.3 Powder Compaction

Blended or mixed powders need to be compacted to achieve enough density and strength for full densification. In order to increase the density of powders, an external force can be applied. Blended powders can be compacted, generally, by die compaction and cold isostatic pressing. In addition, injection molding, extrusion and hot isostatic pressing can also be used for compaction. The purpose of pressing is packing powders and decreasing the porosity. By this way, the green density, which affects the final density, will be increased and near net shaped parts can be produced. Pressed parts can shrink by 10 to 20% in linear direction. Due to this fact, pressing dies should be designed by considering the shrinkage of the final part. Moreover, increasing compaction pressure increases the density of the powder up to theoretical limits. This limit depends on the powder characteristics. Schematic drawing for density variation with compaction pressure is given in Figure 3.

As also seen in Figure 3, during pressing, the density is nearly equal to the apparent density of the powder initially. Powders become rearranged due to the application of pressure. Voids get increasingly smaller and packing coordination increases.

Increasing pressure decreases the porosity and helps to better packing. Finally, increasing pressure further causes deformation on particles and lately the whole system becomes compressed [5]. The pressing behavior of the metallic powder with increasing compaction pressure is schematically shown in Figure 4.

Compaction of mixed powders by a rigid die is a low cost method and involves easy tooling. However, compacted parts may have density variations due to the friction between the powder mass and the mold wall [7], as shown in Figure 5.

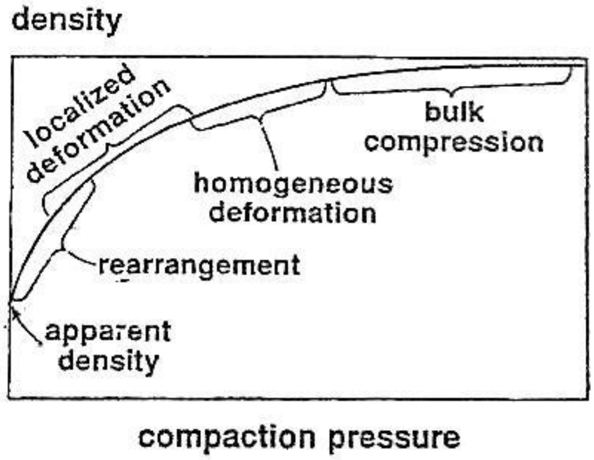

Figure 3 Sketch of density variation with increasing compaction pressure [5]

The main difference between die compaction and cold isostatic pressing lies in the uniformity of compacted parts. Isostaticaly pressed parts have lower friction and are compacted uniformly on all surfaces of the flexible die. Generally, elastomeric materials are used as a mold. These types of molds make parts compactable with any height-to-diameter ratio. The saturation pressure of some metal powders to compact powders into a desired shape are given Table 3. Typical WHAs can be compacted between 200 and 450 MPa pressures.

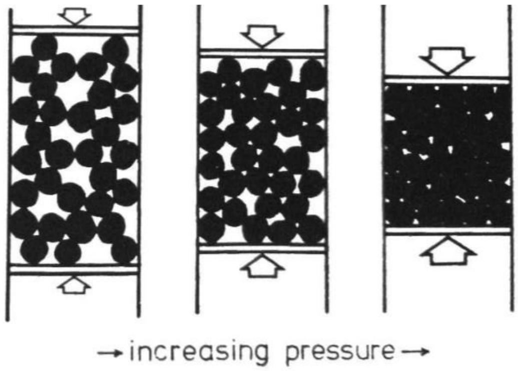

Figure 4 Basic steps of metallic powder compaction [5]

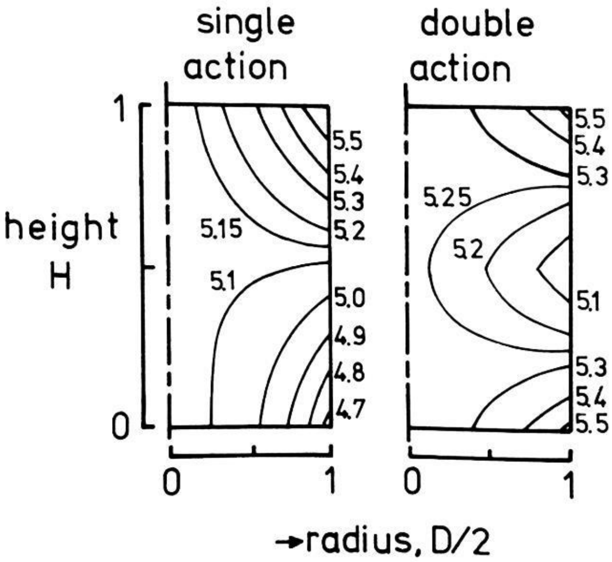

Figure 5 The density variation in die pressing [5]

Table 3 Saturation Pressure Ranges for Some Metallic Powders Compacted by Cold Isostatic Pressing [7]

Powder Material	Pressure Range (MPa)
Iron	310-415
Copper	140-275
Aluminum	55-140
Stainless Steel	310-415
Titanium	310-415
Tungsten	240-415
Tungsten Carbide	170-205

2.2.4 Sintering

Sintering is a thermal treatment for bonding particles into a principally coherent solid structure with mass transport events that usually take place at an atomic level. In order to reach full density, solid state sintering (SSS), activated sintering (AS) and liquid phase sintering (LPS) can be applied. For the requirements of near net shape properties, SSS and AS methods are preferred. In order to get improved mechanical properties, LPS should be used in the consolidation of compacted parts.

Sintering methods used for WHAs, namely solid state sintering (SSS), activated sintering (AS) and liquid phase sintering (LPS), are described in detail as follows:

2.2.4.1 Solid State Sintering

In solid state sintering (SSS), sintering can be accomplished by the consolidation of small solid particles by heating. As an example, the refractory metal W can be densified at temperatures near 2200°C (approximately 0.7 of its absolute melting temperature) in its pure form in the solid state. In order to densify at lower temperatures like 1800°C, compacted W powders should be held for a long period of time at the given temperature. The important difference in SSS is that the powder compact is sintered at a temperature below the melting point of the constituent materials. During the sintering process, contact points decrease the surface energy by removing free surfaces, meanwhile grain boundary area is eliminated via grain growth.

In order to understand the phenomenon of SSS, a single elemental model can be expressed, which is discussed below. Before going on further, it should be emphasized that, in an alloy system, powders can form intermetallic compounds and also powders may dissolve in each other. Therefore, the single elemental model to be discussed here might not be applicable for such a system.

Small, irregularly shaped powder particles have higher surface area/volume ratios and this will increase the total surface energies. For the single elemental model mentioned above, assume that two spherical particles come into contact with each other as shown in Figure 6. There will be a neck formation between these two particles. Sintering continues with the neck growth and, at the same time, some other morphological changes occur. Firstly, interatomic bonds forms at initial contact points and generate cohesive necks, which grows along the neck diameter, which can be seen in Figure 6. Growing occurs with different mass transport mechanisms such as surface diffusion, grain boundary diffusion, lattice/volume diffusion, evaporation-condensation and viscous flow. Solid-state diffusion is the dominant mechanism for sintering of many metallic materials. Following neck formation, neck growth occurs with atoms diffusing from the volume of each contact point to the neck region. Grain boundaries and surfaces of particles also provide mass transport paths that are less blocked for atoms diffusing to the neck area. In addition, vapor-evaporation-condensation may also contribute to bonding and growth process in some powder systems. For sintering to take place, these mass transport mechanisms must be activated by energy like heat.

For sintering, the required energy to activate the mass transport mechanisms enforces an activation energy barrier. This energy barrier must be surpassed for sintering to occur. In the energy-state diagram given in Figure 7, the schematic plot for energy reductions occurring during sintering stages can be seen.

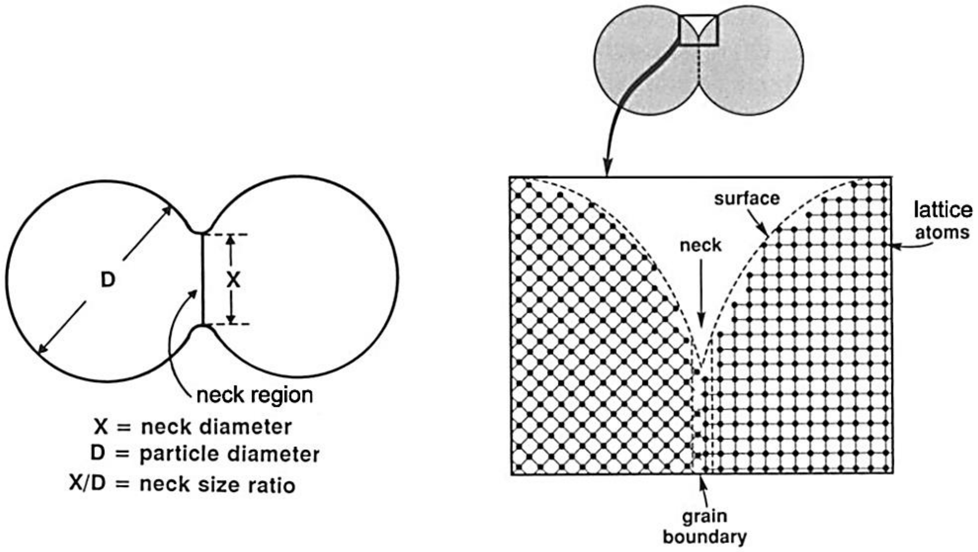

Figure 6 Neck region and schematic drawing of grain boundary formation

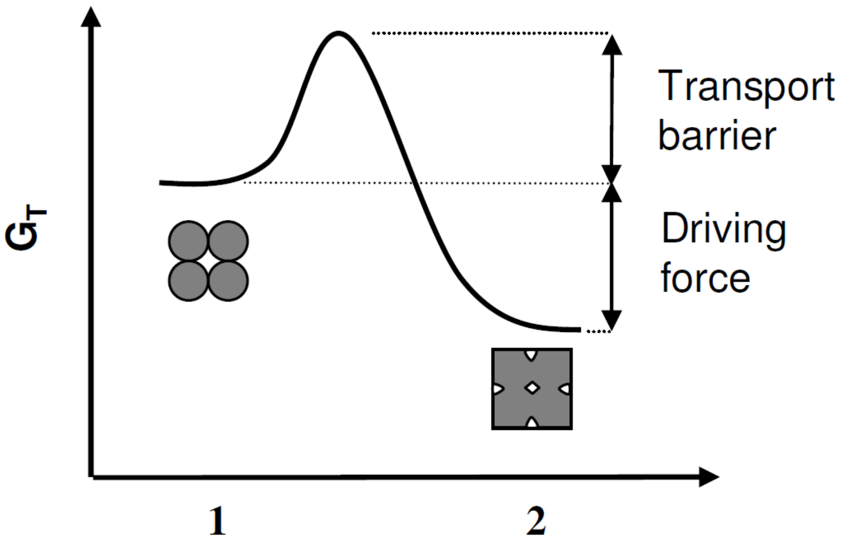

Figure 7 Schematic energy-state diagram for: (1) initial pre-sintered, and (2) final post-sintered condition

The driving force for sintering can be expressed by using Equation 1 given below:

$$\Delta G_T = \Delta G_v + \Delta G_b + \Delta G_s \tag{1}$$

Where $\Delta G_T$is the total free energy of the powder system and it contains the terms ΔG_v for volume, ΔG_b for grain boundary and ΔG_s for free surface energy reduction, respectively [8]. The total surface area of powder materials is higher when compared to bulk materials due to the high portion of internal powder surfaces. ΔG_v can be omitted for sintering processes involving non-interacting powders with no phase transformations. In addition, ΔG_b is relatively small when compared to the free surface energy, ΔG_s. Consequently, for non-interacting powder systems, the dominant driving force for sintering is the reduction of the surface free energy of particles. The surface atoms of the powder particles have higher energy than those in the particle. This is because the atoms on the surface have lower restriction by other atoms, whereas atoms within the particle are hindered by inside atoms. In this respect, small grain size particles promote the densification rate due to their higher surface area per unit volume. In the light of this discussion, it can be said that fine powder particles have higher driving force for sintering compared to coarse particles due to their higher surface area [8].

The fundamental theory for the solid state sintering (SSS) investigates the process within three stages. These stages are named as; initial, intermediate and final stage. The morphological changes and density variations occurring during these stages are given in Figure 8. For providing a practical example to SSS systems, the SSS stages observed in a sintered Ni powder system is depicted in Figure 9, and the geometrical changes occurring during these three stages is shown in Figure 10. As can be seen in Figure 8, in the initial stage, neck formation is observed among contacted particles. The growth of these necks depends on the mass transportation. Then, in the intermediate stage of sintering, the curvatures on particle surfaces become smoother and particles become interconnected to each other. In the final stage, pores between particles get smaller and become closed, and also larger grains are obtained.

In the initial stage, the sharp curvature gradients located near the inter-particle neck dominates the kinetics of the process. Although the pore structure is not smoother, the pores have an interconnected and open structure [9], [10]. The curvature gradient at the neck point dominates the mass flow. In this stage, around 10% increase can be seen in the densification. The neck formation and growth observed in a practical powder system can be seen in Figure 9.

In the intermediate stage, neck growth can be seen. The main difference between the initial and intermediate stages is decreasing surface energy. Moreover, pores become much smoother when compared to the initial stage. At this stage, the grain-pore structure becomes more important than the inter-particle neck growth. As can also be seen in Figure 8, the highest amount of densification is observed in the intermediate stage. For this stage, interfacial energy, which consists of the surface and grain boundary energy, is the dominant driving force.

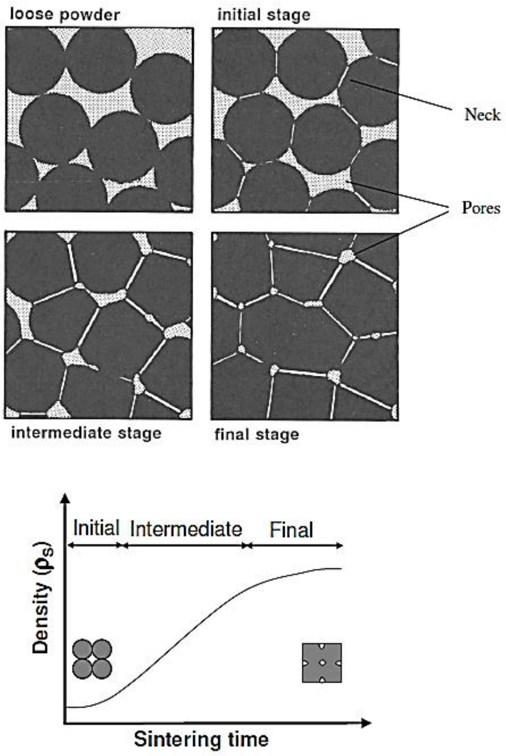

Figure 8 Schematic drawings showing the geometrical changes and densification behaviour during sintering stages [8]

In the final stage, pores become closed with a minimal speed, but grain growth is detected. In order to fill the three-dimensional space efficiently, the grains may assume an appropriate geometrical form, such as a tetrakaidecahedron, as shown in Figure 10.

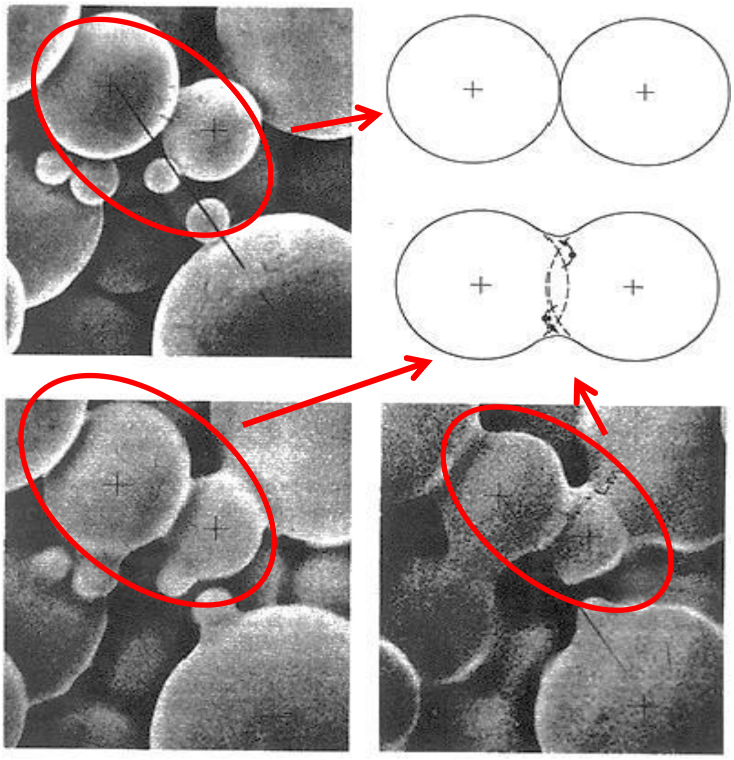

Figure 9 Neck formation and growth observed in a practical Ni powder system [11]

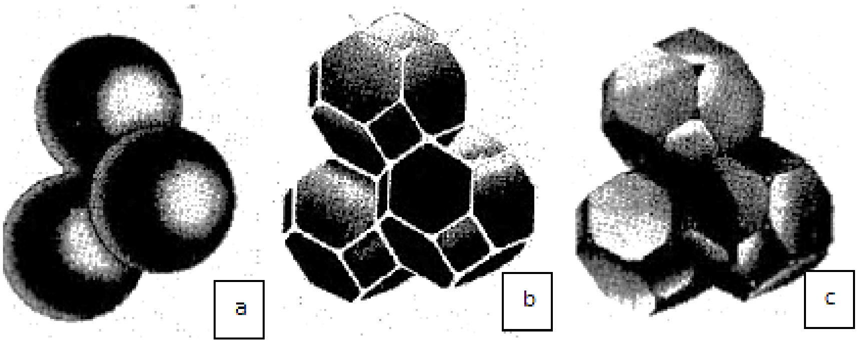

Figure 10 Stage of sintering showing geometrical changes from spherical shape to tetrakaidecahedron, a) initial, b) intermediate, and c) final stages [12]

As mentioned above, the driving force for sintering is the reduction of surface energy (γ). This surface energy gives growth to what can be termed as a sintering stress (σ), which grows from the energy difference between high and low radius of curvature. The relation between sintering stress and radius of curvature is given in Equation 2 below;

$$\sigma \propto \frac{\gamma}{r} \qquad (2)$$

It can be concluded that smaller particles will have higher sintering stress due to high degrees of curvature. This high stresses, during sintering, leads the mass transport in directions, which contribute to particle bonding and growth of neck.

Mass transport mechanisms must be activated for sintering of powder materials. Thermal activation energy for atomic mobility that is required for sintering to occur is activated by applied heat. Hence, surface stresses/energy and atomic mobility are important parameters for sintering. In single elemental powder systems, the atomic mobility is related to the diffusional coefficient of the constituent atoms. The diffusion coefficient is a strongly temperature-dependent variable and has an Arrhenius type of temperature relationship, as given in Equation 3 below;

$$D = D_0 e^{\frac{-Q}{RT}} \qquad (3)$$

Where D is diffusion coefficient, D_0 is pre-exponential factor, Q is activation energy, R is gas constant and T is absolute temperature. As a result, for SSS, the sintering rate is dependent on diffusion rate and increases with temperature exponentially.

2.2.4.2 Activated Sintering

Addition of some minor metal into the major metal powder increases the densification rate at a relatively low temperature with respect to the melting point of pure metals. This phenomenon is known as activated sintering. In the activated sintering process, the liquid phase does not appear. Small amounts of minor metal addition may decrease the onset temperature of sintering to as low as 15-40% of the eutectic or peritectic temperature [13].

The melting temperature of materials affects the diffusion coefficients. In order to densify a high melting temperature material, relatively higher temperatures are required for achieving higher self-diffusion rates. However, low melting temperature materials have higher diffusion coefficients when compared to high melting temperature ones. Consequently, activated sintering can take place in systems where a high melting temperature material is soluble in a low melting temperature material [8]. An idealized binary phase diagram suitable for activated sintering is given in Figure 11. In this figure, an appropriate powder mixture composition and sintering temperature combination for activated sintering is shown by dotted lines.

In activated sintering, small activator additions of such as 1 wt% make a radical change on sintering rate [14]. Added activators provide a means for rapid mass transport and this affects the sintering process. For example, the addition of 1.5 wt% Pd into the chromium powder and sintering at 1400°C can produce bulk metal with up to 96% density. However, sintering of pure chromium powder at 1400°C produces only 78% dense metal.

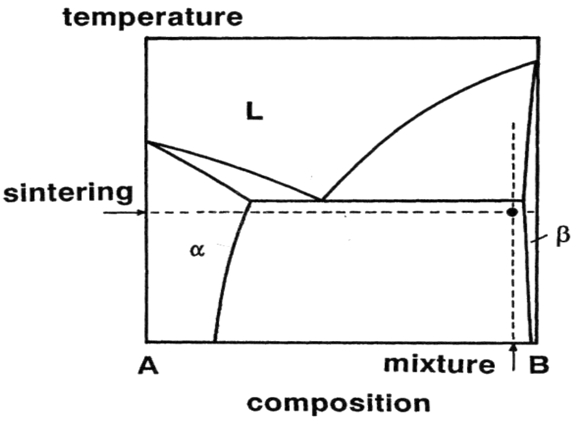

Figure 11 Idealized phase diagram for activated sintering [8]

As another example, in the densification of tungsten powders, relatively small amounts of transition metals such as Ni, Co, Fe, Pd, Pt can be used as activators. In Figure 12, the effect of such activators on the shrinkage and fractional density of tungsten can be seen.

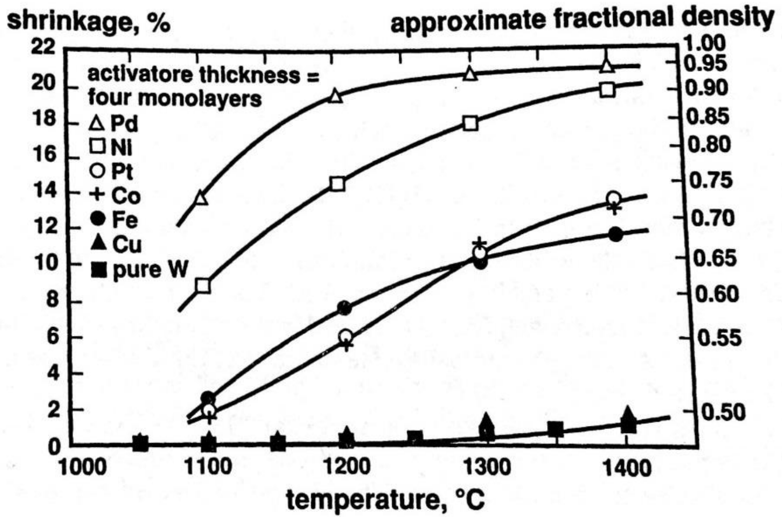

Figure 12 Activated sintering behaviour of tungsten with some metallic additions [8]

2.2.4.3 Liquid Phase Sintering

Liquid phase sintering (LPS) is another consolidation method for compacted powders. In the LPS process, the densification rate is greater than that in SSS and activated sintering due to presence of a liquid phase. The formation of the liquid decreases the surface energy of particles and this increases the driving force for sintering. Most of the powder systems are suitable for densification by LPS. In order to obtain densification by LPS, the liquid in the system should have an ability to wet the particles. Moreover, solid particles must dissolve in the liquid [9]. By

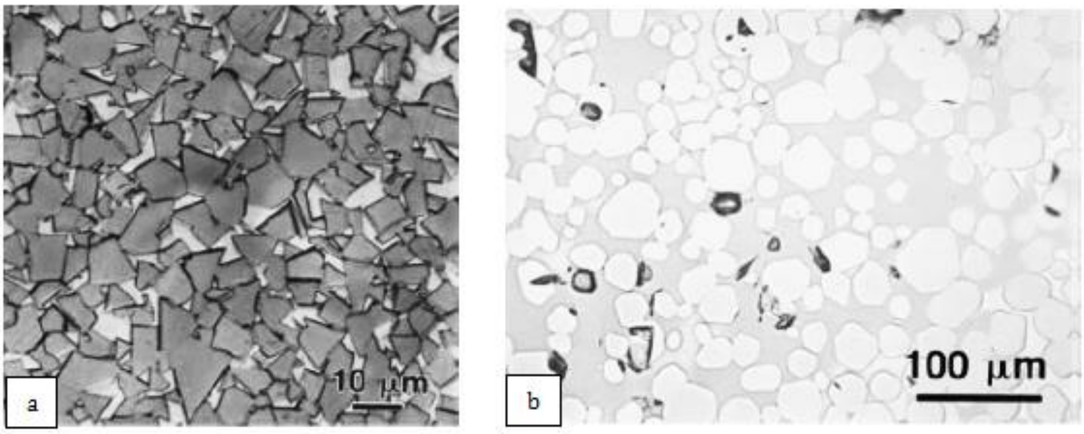

Figure 13 Typical microstructures of alloys densified by LPS: a) WC-Co, b) $MoSi_2$-Cu [2]

using LPS, alloy powder systems such as Cu-Co, Cu-Sn, Fe-Cu, WC-Co, W-Ni-Fe and W-Ni-Co can be densified. The typical microstructures of alloys densified with LPS are shown in Figure 13.

As mentioned above, the liquid is required to wet the solid phase for LPS. The difference between the wetting and non-wetting behavior of a liquid on a solid particle is shown in Figure 14. In the ideal case, the liquid should perfectly wet the surfaces of the solid particle grains, as is shown in Figure 14 [15]. The wetting of liquid on the solid grain increases the densification rate of the whole system due to the enhancement of the diffusion rates. As shown in Figure 15 , in the perfect case, pores shall be entrapped within the liquid phase. This causes a pressure difference across the surface of a spherical pore of radius r in the liquid phase. The pressure difference can be expressed by Equation 4 [15]:

$$\Delta p = -\frac{2\gamma_{lv}}{r} \tag{4}$$

where Δp is pressure difference, γ_{lv} is liquid-vapor surface energy and r is radius of the spherical pore.

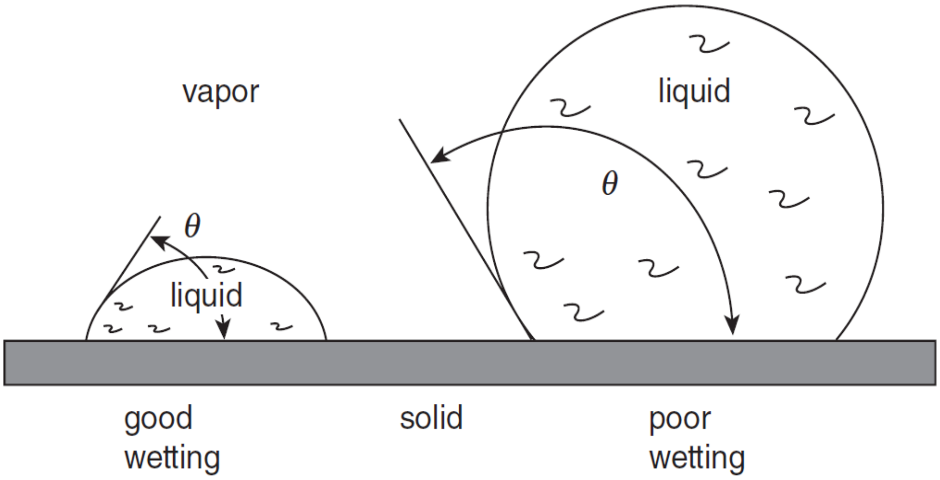

Figure 14 Good and poor wetting of liquid on solid; θ is the wetting angle [15]

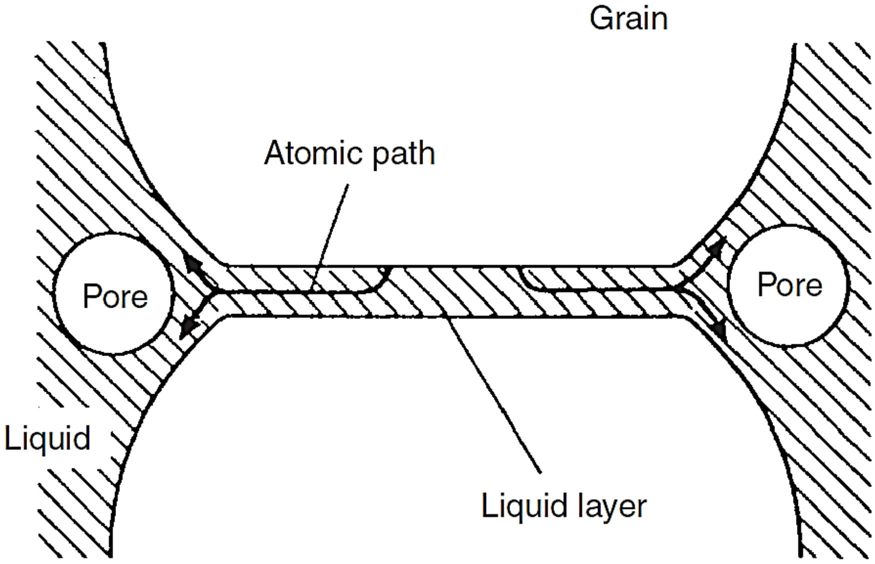

Figure 15 Schematic drawing showing the ideal case for liquid phase sintering [15]

In the course of LPS, mixed powders and pores interact with each other during heating. At a certain stage during sintering, the liquid phase forms and wets the solid particles and this helps the whole system to densify. At the later stages of LPS, coarsening of the particles can be observed owing to the solubility differences between small and large particles. In many systems, the presence of the liquid causes an increase in the grain shape change rate, which facilitates pore elimination.

The microstructural changes that occur during LPS are divided into three stages as;

1. Particle rearrangement
2. Solution and reprecipitation
3. Solid phase sintering

The variation of the densification behavior during the course of these three stages is shown in Figure 16, and microstructural changes occurring during these stages are depicted in Figure 17. In what follows, the general characteristics of these three stages are discussed briefly.

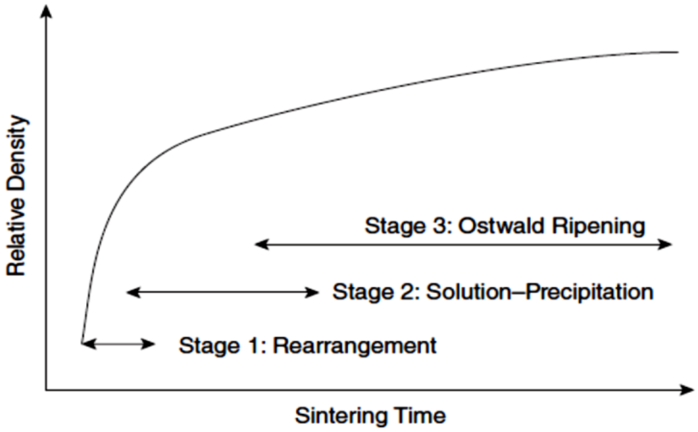

Figure 16 Schematic drawing of the densification behaviour observed during the course of the three stages of LPS [9]

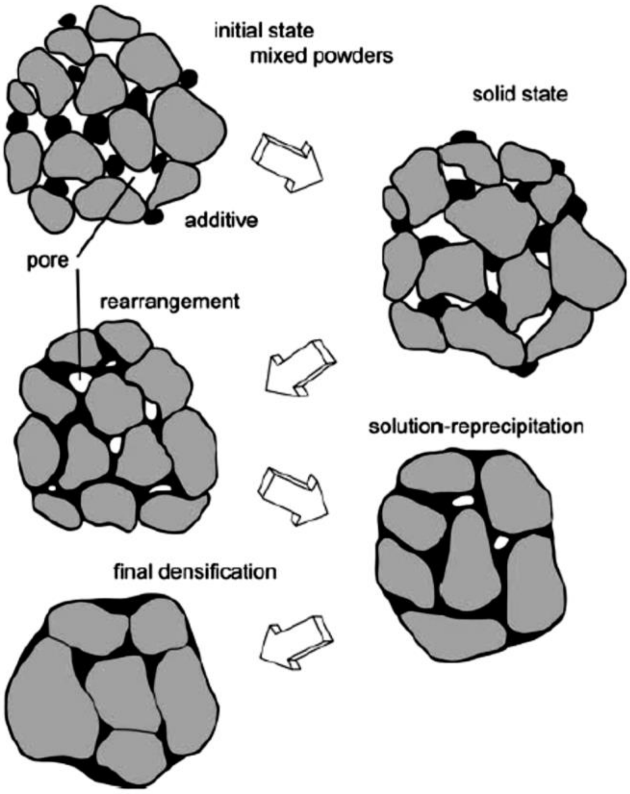

Figure 17 Microstructural changes during liquid phase sintering stages [2]

- **Particle Rearrangement**

In the course of the particle rearrangement stage, the liquid forms and wets the solid particles due to capillary forces. This capillary action makes particles to become closer. Closed particles make particle clusters. In addition, the liquid phase aids in the particle surface smoothing. Another aid of the liquid formation is that it enhances the distribution of small and big particles [16] [17]. Particle size, wetting ability, dihedral angle, green density and porosity are important factors that affect the densification behavior in the rearrangement stage.

There are quite a few studies on the modeling of the rearrangement stage. Hwang and coworkers [18] have developed a theory that includes the effect of the wetting angle. However, this theory does not explain the time dependency of the shrinkage. In the rearrangement stage, low dihedral and contact angles make shrinkage higher. Rough particle size and shape may result in mechanical interlocking, which makes the structure more porous. In this context, Hupmann et al [19] claimed that, in W-Cu system, the main parameter that affects the rearrangement stage is the uniformity of particle mixing and packing.

- **Solution-Reprecipitation**

After the liquid formation, the solid particles get closer to each other. If there is no solubility of solid particles in the liquid, the densification will be limited, resulting in a porous final structure. If the solid particles can dissolve in the liquid, however, densification can be enhanced predominantly via the solution-reprecipitation process. The solution-reprecipitation process takes place mainly in three stages;

- Solid particles dissolve in the liquid phase,
- Dissolved solid diffuses into the liquid phase,
- Dissolved solid precipitates on larger grains or concave regions [2].

In the solution-reprecipitation stage, grain size, grain shape and bulk density dramatically change. In most of the cases, the solution-reprecipitation stage is diffusion controlled. During this stage, grains tend to acquire new shapes more suited for closer packing through a process called grain shape accommodation. Conceptual model of grain shape accommodation is given in Figure 18.

In the discovery era of the LPS, Kingery [20] offered a thin film concept to explain the solution-reprecipitation process. In this concept, the thin film is proposed to wet the spherical solid particles completely. He claimed that the driving force for this process is the difference between chemical potentials. This chemical potential difference comes from the pressure change between the thin film at the particle surface and the liquid surrounding on the solid particles. In a latter work, Messing et. al [21] have added the dihedral angle and volume fraction of liquid into the explanation of solution-reprecipitation analysis.

After the grain shape accommodation step, grains continue to coarsen. In order to explain microstructural coarsening, Ostwald ripening theory can be used. Ostwald ripening theory says that smaller grains become smaller whereas larger grains become larger as time passes, so as to reduce the total surface energy. In practice, grain coarsening can be expressed as a power law with time, as given in Equation 5.

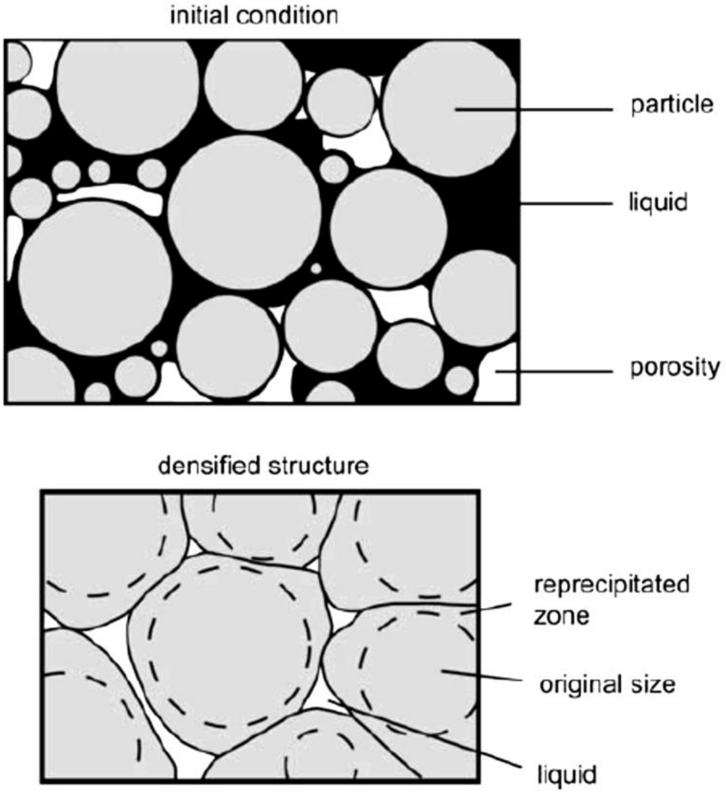

Figure 18 Schematic drawing of densification and grain shape accommodation processes in the solution-reprecipitation stage [2]

$$G^n - G_0^n = Kt \tag{5}$$

where G_0 is the initial grain size, G is grain size during LPS, K is growth rate constant and t is sintering time. n is changing from 2 to 4 and equals to 3 for diffusion controlled growth processes [17].

- **Solid State Sintering**

In the solid state sintering stage, liquid and connected solid particles can be found between the grains. In this stage, the system is rigid and grains continue to grow. However, trapped gas in the pores can inhibit the densification. Sintering under vacuum or low weight gas can help to decrease the porosity and obtain full densification [2].

2.3 Powder Metallurgy of W Based Alloys

Typical WHAs contain 90 to 98 wt% tungsten in their composition. Common WHA systems are W-Ni-Cu, W-Ni-Fe and W-Ni-Co as stated before. In the W-Ni-Cu system, WHAs with Ni/Cu binder ratio ranging from 1/1 to 4/1 are common; similarly, W-Ni-Fe alloys contain binder with Ni/Fe ratio ranging from 3/2 to 4/1. Common W-Ni-Co alloys, on the other hand, contain Ni/Co ratio 9/1 and 8/1. Fundamentally, these alloys are fabricated by LPS, but SSS and activated sintering are also used in the alloy production. Due to their composite structure, WHAs can have good machinability.

Powders for WHAs are selected between 1 and 10 μm average particle size for full sintering and uniform structure. Powders can be blended with or without polymeric addition. The choice of polymeric addition depends on the consolidation shape and structure. For die-cavity filling, the powder may need to be mixed with a polymeric binder such as about 1 to 2 wt% paraffin and should be granulated. This operation requires a de-binding step before sintering.

Mixed powders are needed to be compacted in order to give the required shape. Die pressing or cold isostatic pressing can be used for powder compaction. Pressed WHA powders reach 50-65% theoretical density in their green state.

As an example, typical W-Ni-Fe alloys are sintered at nearly 1420-1440°C in the solid state. For some alloys, LPS was performed at temperatures between 1470 and 1570°C. For all sintering processes, the sintering atmosphere affects the density and porosity content of WHAs [22]. Generally, H_2 is used as the sintering gas for WHA production. In addition, Ar and N_2 can be used during sintering. However, these insoluble and low diffusivity gases may become trapped in the pores while sintering progresses to the densification stage. This adverse manner decreases the density of sintered parts [23].

Addition of Ni, Co, Fe, Cu and other metals generally alter the magnetic character, corrosion resistance and mechanical properties of WHAs. First examples of WHAs were W-Ni-Cu alloys that were developed for electrical applications. Lately, W-Ni-Fe alloys are developed and nowadays they are widely used in industrial applications. Latest investigations of WHAs are replacing Fe with Co. W-Ni-Co alloys have superior mechanical properties after post sintering processes such as heat treatment and swaging.

Many studies have been carried out on WHAs from 1930's up to now. The discovery of the liquid phase sintering of WHAs has caused an increase in the scientific studies on this area. Mondal et. al [24] investigated the effect of heating mode and temperature on the sintering of 90W-7Ni-3Fe alloys. In this study, the heating rate was changing from 10°C/min to 112°C/min. The higher heating rate was obtained by the microwave sintering method and for smaller heating rate, conventional furnaces were used. Specimens were sintered at temperatures ranging from 1200°C to 1500°C with 50°C increments. In Figure 19, the sintered density of 90W-7Ni-3Fe alloys changing with temperature is given.

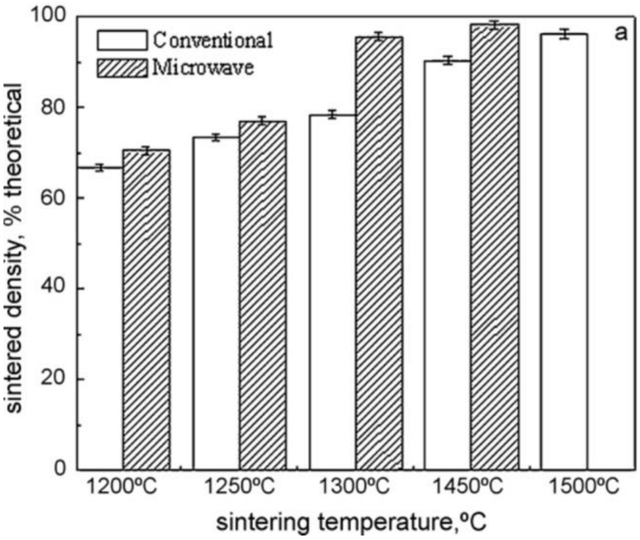

Figure 19 Effect of sintering temperature on the density of 90W-7Ni-3Fe alloy [24]

It is clearly seen in Figure 19 that increasing temperature has increased the sintered density of the investigated WHA. Also, higher heating rate has increased the sintered density and decreased the processing time. Furthermore, higher heating rates have made the grain size smaller compared to those sintered in conventional furnaces.

2.4 Mechanical Properties of W Based Alloys

W based alloys have high strength and high ductility when produced properly. It is known that the strength and ductility of WHAs can reach up to 1700 MPa and 30%, respectively [25]. In order to obtain higher mechanical properties, the production process should be controlled in terms of:

- Quality of powders
- Powder mixing
- Sintering cycle and atmosphere
- Post-sintering deformation and heat treatments

The presence of pores greater than 0.5% or improper sintering can reduce the mechanical properties such as toughness, ductility and strength significantly. In addition, micro-pores forming at the cooling step of the sintering cycle, trapped sintering gas, insufficient sintering time, prolonged sintering times etc. affect the mechanical properties in an adverse way [26].

Hydrogen is generally used as the sintering gas for liquid phase sintering of WHAs. The usage of inert gases such as Argon during sintering decreases the mechanical properties. Moon et. al. [27] stated in their work that coarsening of the W particles more rapidly than the neck growth has caused incomplete densification under inert gas atmosphere. On the other hand, the usage of dry hydrogen as the sintering gas may cause hydrogen embrittlement due to the dissolution of a high amount of gas in the binder matrix. Vacuum can also be used for the sintering of WHAs. The mechanical properties obtained under vacuum conditions are quite reasonable and close to those obtained under hydrogen atmosphere. In many cases, the period of sintering affects the mechanical properties. It can be better to choose shorter sintering times like 30 minutes than longer times. For longer sintering time, W grains coarsen and decrease the strength of the sintered product. For WHAs, the variation of properties with sintering time under different sintering atmospheres is given in Figure 20 [23].

Typical WHAs consist of pure W grains and a binder matrix phase in their microstructure. The composition of WHAs also affects the mechanical properties of products. With higher W contents in the alloy, higher strength values are obtained. However, higher W content also decreases the ductility of the alloy. In addition, the solubility of W in the binder matrix phase may cause the formation of brittle intermetallic phases. For example, in order to prevent the intermetallic formation in the W-Ni-Fe system, Ni/Fe ratio can be selected at 2.33 (7/3). However, this is not the composition that provides higher mechanical properties. In Figure 21, percent elongation and tensile strength variation with Ni/Fe ratio under vacuum annealing

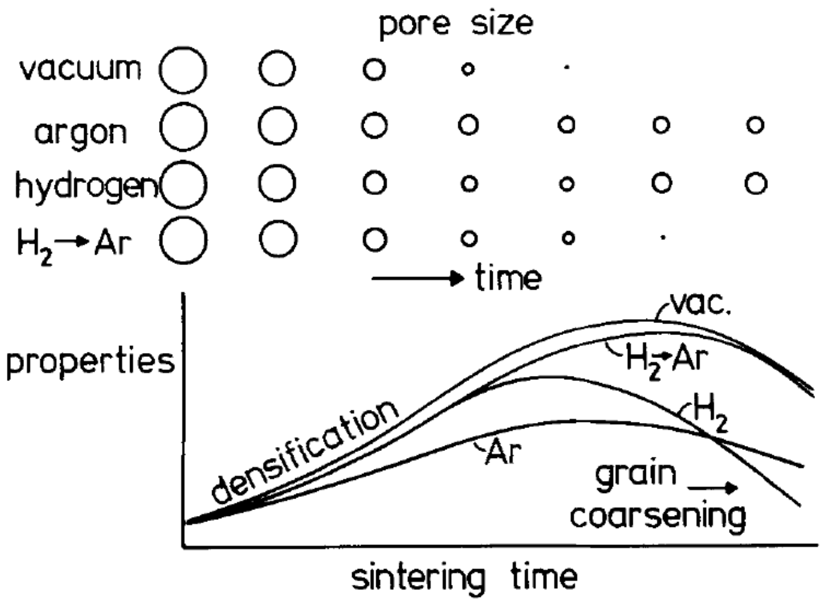

Figure 20 Schematic drawing of pore size and properties varying with sintering time and atmosphere for W-Ni-Fe alloys [23]

(VA) and vacuum annealing and quench (VA+Q) conditions is presented for 93W-Ni-Fe alloys. It is clearly seen in Figure 21 that higher mechanical properties were obtained for VA condition with Ni/Fe ratio of 4 and for VA+Q condition with Ni/Fe ratio of 14 [28].

Mechanical properties not only depend on Ni/Fe ratio for the W-Ni-Fe alloy system, but also on alloy W content as well. In Table 4, the effect of alloy W content on the mechanical and physical properties of selected W-Ni-Fe alloys with 2.33 Ni/Fe ratio is shown [28]. It is seen in Table 4 that density increases with increasing W content, whereas % elongation decreases. For maximum tensile strength values, W content need to be 93% for such investigated W-Ni-Fe alloys.

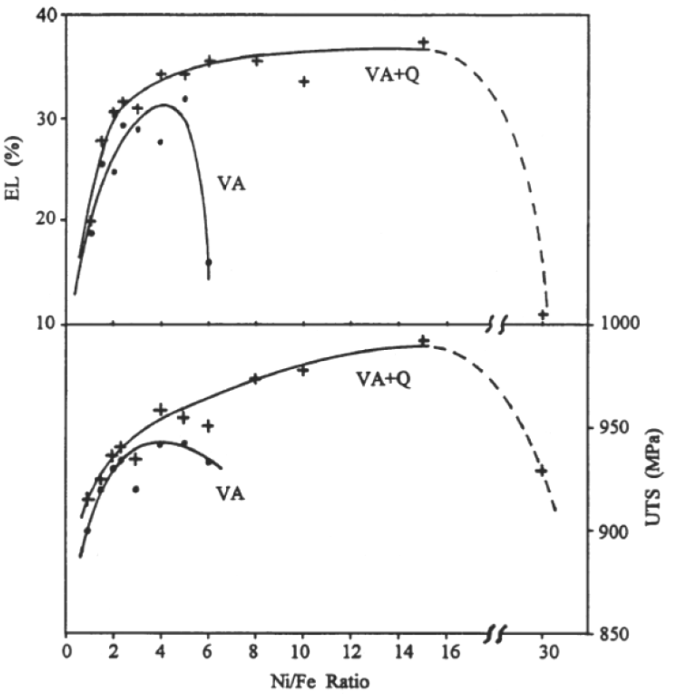

Figure 21 Tensile strength and % elongation variation with Ni/Fe ratio for 93W-Ni-Fe alloys under VA and VA+Q condition [28]

Table 4 Mechanical and Physical Properties of W-Ni-Fe Alloys with 2.33 Ni/Fe Ratio Sintered at 1500°C for 30 min and Vacuum Annealed at 1100°C for 8 Hours [28]

Properties of the Alloys	**Alloy Composition Investigated (wt%)**		
	88W-8.4Ni-3.6Fe	93W-4.9Ni-2.1Fe	95W-3.5Ni-1.5Fe
Density (g/cm3)	16.60	17.52	17.98
Tensile Strength (MPa)	894	996	916
Elongation (%)	30	23	11

It is possible to increase the mechanical properties of WHAs with thermomechanical treatments. W-Ni-Fe and W-Ni-Co are suitable alloy systems for deformation and heat treatment. It is reported that after thermomechanical treatments WHAs can reach about 1650 MPa tensile strength with 50 HRC hardness values [7]. Figure 22 presents the plot of tensile strength and percent elongation for 91W-Ni-Fe and 91W-Ni-Co in unworked and thermomechanical treated conditions. If one have greater initial unworked properties, it is possible to get more processing options. In order to increase the strength and hardness of WHAs, rotary swaging is used, which is a rapid short-stroke hammering process [7]. With this swaging operation, the product increases in length and decreases in width. Also, the swaging operation changes the microstructure of WHAs. In Table 5, the maximum allowable percentages of reduction in area or deformation percent with swaging is given for some selected WHAs.

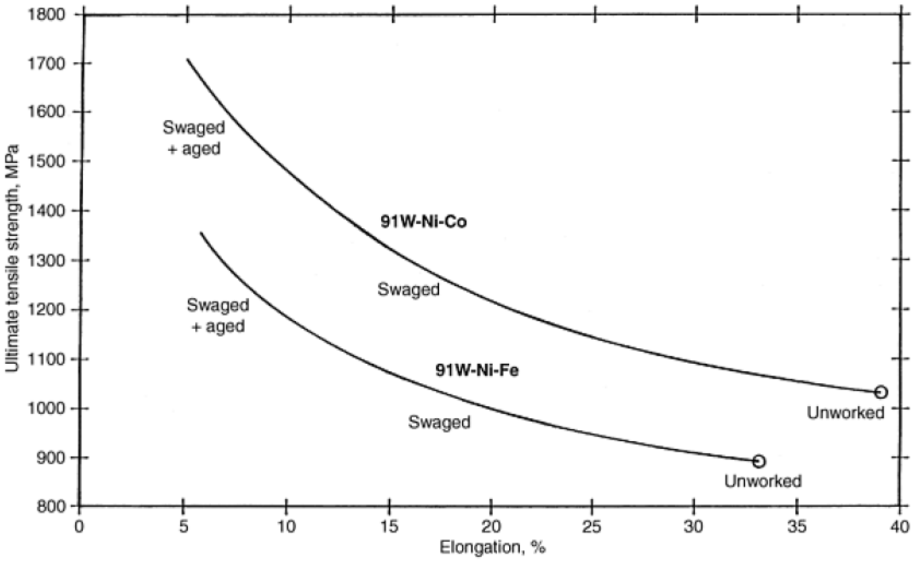

Figure 22 Tensile strength and percent elongation variation with unworked, swaged and swaged after aged condition for 91W-Ni-Fe and 91W-Ni-Co alloys [7]

Table 5 Swaging Limitations for Selected WHAs [7]

Alloy Family	**Maximum % Reduction in Area for Swaging**
W-Ni-Fe (2.3≤Ni/Fe≤4)	25
W-Ni-Fe-Co (typical)	30
W-Ni-Co	40

Kiran et. al [29] has investigated the effect of swaging and heat treatment on the mechanical properties 90W-6Ni-2Fe-2Co alloys. They used elemental powders and mixed them in a ball mill. The addition of Co was found to increase the strength and ductility when the specimens were deformed at different swaging rates and aged at different temperatures. It is concluded that higher deformation rates increase the tensile strength and decrease the percent elongation, as it is shown in Figure 23. It is known that higher Co contents tend to make brittle intermetallic phases. These brittle intermetallic phases decrease the mechanical properties of W-Ni-Co alloys. In the literature, W-Ni-Co alloys that contain Ni/Co ratio between 2/1 to 9/1 were preferred.

Kennedy et. al [30] investigated and characterized the influence of microstructure and strain rate on the fracture and tensile behaviour for 93W-4.9Ni-2.1Fe and 91W-6Ni-3Co alloys. In their experiments, rod specimens were swaged and aged. Tensile test were applied to the specimens at different strain rates and fracture surfaces were investigated with scanning electron microscope (SEM). As a result, Ni-Co alloy was found to have higher tensile strength than the Ni-Fe one. Lower W content, higher percentage of binder matrix and lower average grain size (by the aid of Co in matrix) enhanced the work hardenability of the alloy during swaging, as it is seen in Figure 24 [30].

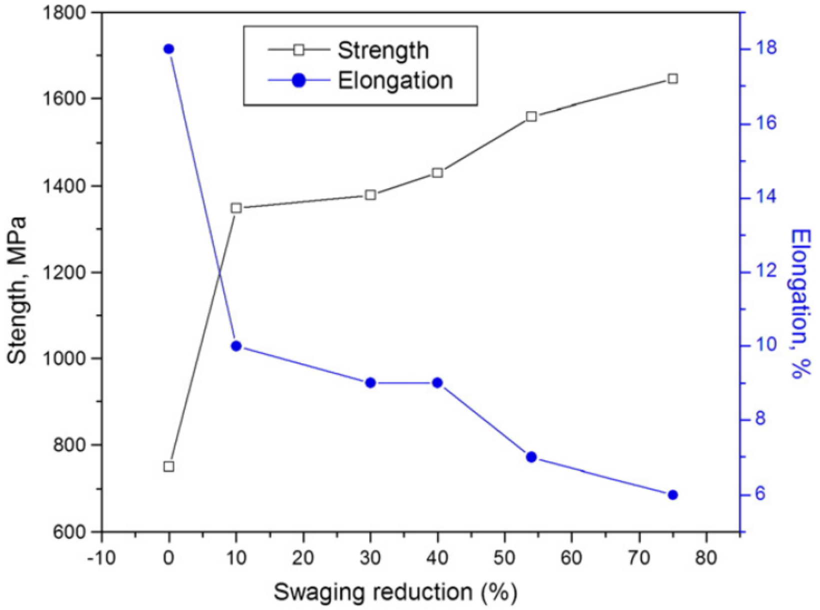

Figure 23 Variation of strength and percent elongation with swaging reduction for 90W-6Ni-2Fe-2Co alloys [29]

Katavic et. al. [31] investigated the effect of swaging and heat treatment on mechanical properties of 91W-6Ni-3Co alloy. In the experiments, specimens were deformed with 10, 20 and 25 % reduction in area, heat treated and aged with different temperature and time. In order to characterize the mechanical properties of the specimens, tensile and toughness tests were performed. When compared to swaged ones, swaged and heat treated alloys showed decreased strength, ductility and partially toughness. Strain aged specimens, on the other hand, showed increased strength and hardness but decreased ductility and toughness.

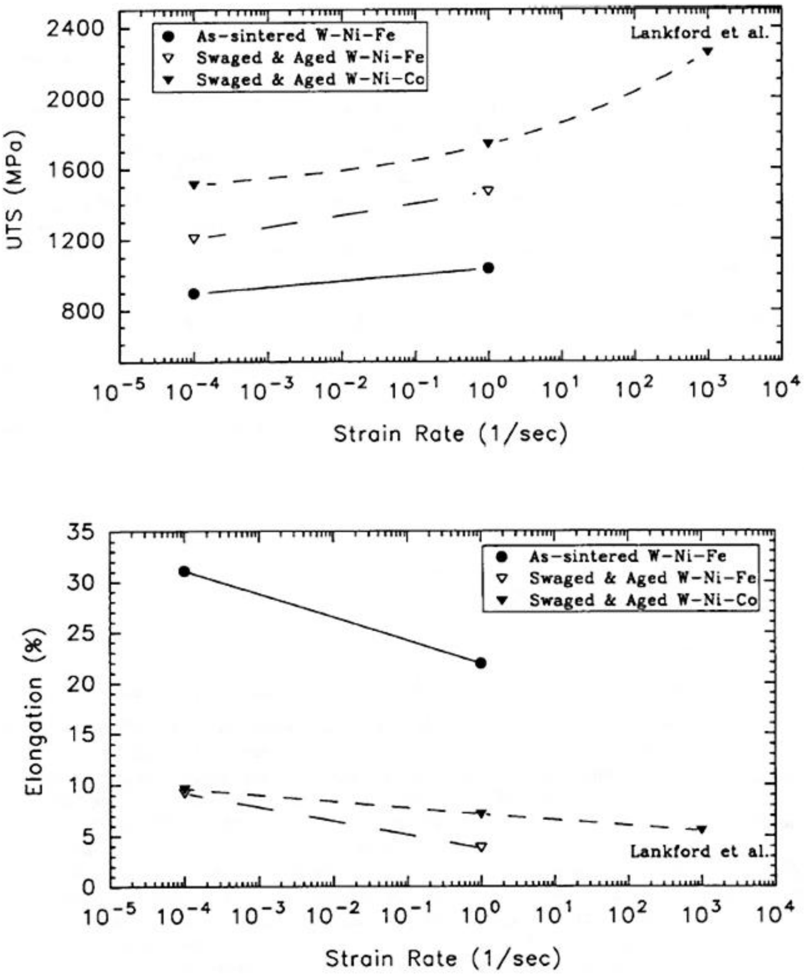

Figure 24 Strength and percent elongation variation with strain rate for unworked W-Ni-Fe and thermomechanical treated W-Ni-Fe and W-Ni-Co alloys [30]

CHAPTER 3

EXPERIMENTAL PROCEDURE

In this work, the effects of composition and sintering variables on the microstructural characteristics of selected W-Ni-Co alloys were studied. The alloys selected for the study were W-rich compositions ranging between 90 and 97 wt% W. The investigated alloys were produced by applying conventional powder metallurgy methods and procedures. Raw W, Ni and Co elemental powders were mixed in a Turbula mixer and compacted by cold isostatic pressing. Compacted specimens were sintered in a horizontal tube furnace under flowing hydrogen (H_2) atmosphere. Sintered specimens were then subjected to microstructural and mechanical characterization by using suitable techniques. Specimen preparation and structural characterization techniques applied in the study will be explained in the following subsections in detail.

3.1 Alloy Preparation

3.1.1 Raw Materials

In order to prepare the investigated tungsten based heavy alloys, elemental W, Ni and Co powders were used. The general properties of the powders used in the study, namely, the average particle size (APS), shape, purity and source of the powders are given in Table 6. These data were taken from the Certificate of Analysis (COA) document given by the suppliers of the metal powders. SEM micrographs showing the general morphologies of the W, Ni and Co powders used in this study are given in Figure 25.

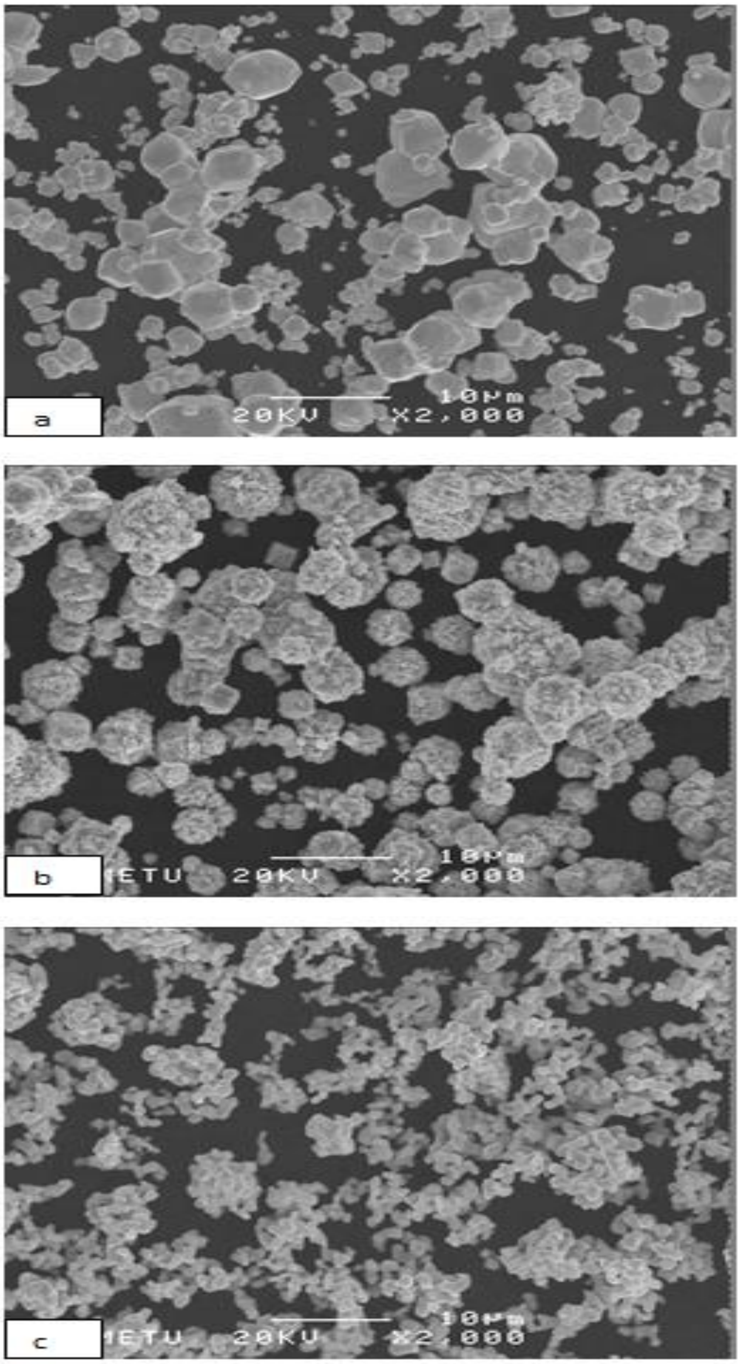

Figure 25 General morphology of the elemental powders used in the study, SEM images, x2000: a) W, b) Ni, c) Co

Table 6 General Properties of the Powders Used In the Study

Element	Average Particle Size (µm)	Shape	Purity (wt%)	Source
W	4.8	Polygonal	99.9+	Eurotungstene AW2123
Ni	4.3	Polygonal	99.9	William Rowland Vale 123
Co	6.0	Polygonal	99.9+	Eurotungstene CO610A25

3.1.2 W-Ni-Co Alloys Investigated

In this thesis work, several selected W-Ni-Co alloys were investigated having compositions ranging from 90 to 97 wt% W with different Ni/Co mass ratios. In the alloy systems studied, the W content was fixed at 90, 92, 95 and 97 wt% and the Ni/Co mass ratio was varied for each fixed W concentration. Within the scope of the thesis work, 90 and 95 wt% W alloy systems were studied in relatively more detail. For these alloy systems, alloys with Ni/Co ratio 6/1, 4/1, 3/1, 1/1 and 1/4 were investigated. 92 and 97 % W alloys with 4/1 and 1/1 Ni/Co ratio were studied to provide further information about the effect of composition on the microstructural characteristics of W-rich W-Ni-Co alloys. Owing to experimental difficulties encountered in sintering and microstructural evaluation studies, Co-rich compositions with Ni/Co ratio above 1/1 were not investigated at all for these alloys.

The W-Ni-Co alloys studied are listed in a compact form in Table 7, together with the alloy codes, Ni/Co mass ratios and theoretical densities. To provide a visual comparison, the alloy systems studied are also shown schematically on a W-Ni-Co composition triangle in Figure 26.

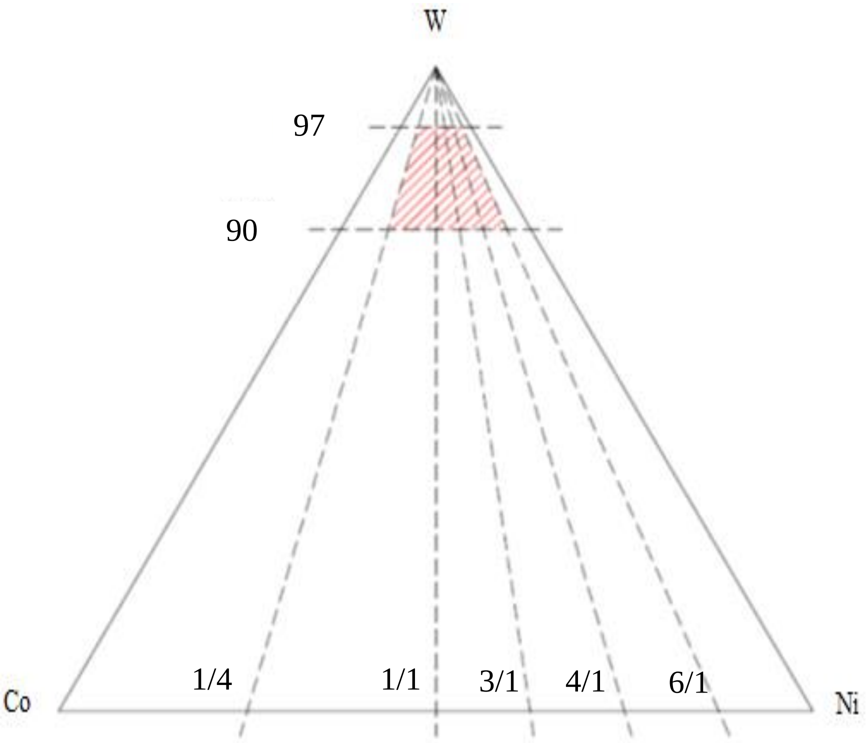

Figure 26 Compositional region of the W-rich alloy systems investigated shown on a schematic W-Ni-Co composition triangle

Table 7 Compositions, Ni/Co Ratios and Theoretical Densities (TD) of the W-Ni-Co Alloys Investigated

Alloy Code	W (wt%)	Ni (wt%)	Co (wt%)	Ni/Co ratio	TD (g/cm^3)
0W14	90	2	8	1/4	17.32
0W11	90	5	5	1/1	17.32
0W31	90	7.5	2.5	3/1	17.32
0W41	90	8	2	4/1	17.32
0W61	90	8.6	1.4	6/1	17.32
2W11	92	4	4	1/1	17.69
2W41	92	6.4	1.6	4/1	17.69
5W14	95	1	4	1/4	18.28
5W11	95	2.5	2.5	1/1	18.28
5W31	95	3.75	1.25	3/1	18.28
5W41	95	4	1	4/1	18.28
5W61	95	4.3	0.7	6/1	18.28
7W11	97	1.5	1.5	1/1	18.69
7W41	97	2.4	0.6	4/1	18.69

3.1.3 Powder Mixing and Compaction

For the mixing of the powders, elemental W, Ni and Co powders were weighted in a Sartorius CP3200S Model Precision Balance to ± 0.01 g accuracy. Powders were weighted separately and put into a high density polyethylene container sequentially by adding W powder first, and Co the last. For each mixing operation, the total amount of the powders prepared was fixed at 500 or 1000 g. Powders have filled approximately half of the volume of the respective container with these amounts. All alloys were then mixed in a Turbula® Shaker Mixer (Model T2F Glenn Mills Inc.) at a speed of 80 rpm for 40 minutes.

Mixed powders were compacted by cold isostatic pressing (CIP). Cylindrical specimens with approximately 18 mm height and 10 mm diameter were prepared with a CIP42260 model Flow AutoClave Engineers cold isostatic press having 400 MPa compaction capacity. Pressing operations were done in elastic polymeric dies under 310 MPa (45000 psi). Powders were weighted and poured into the polymeric dies. The dies were then closed by their lids and covered with another polymeric bag in order to prevent leakage of the pressing liquid inside. Compressed samples were cut into small disk-shaped specimens having approximately 6 mm height and 10 mm diameter by a suitable cutter. With the aid of an emery paper, all specimens were ground gently to get rid of surface irregularities.

3.1.4 Sintering Studies

In order to investigate the effect of sintering variables on microstructural characteristics, W-Ni-Co alloys studied were sintered at different temperatures. The sintering temperatures applied for all of the alloys were 1450, 1475, 1500, 1525, 1550 and 1600°C. All sintering experiments were carried out under flowing H_2 atmosphere for 1 hour.

The sintering experiments were conducted in a horizontal tube furnace (Protherm PTF17/75/400). The temperature uniformity of the furnace was ± 10°C along approximately 120 mm of the hot zone area. The furnace was controlled with a proportional integral derivative (PID) controller and had a B type thermocouple for temperature measurement. In all sintering experiments, an additional S type thermocouple was used to determine the temperature in the near vicinity of the specimens. The flow of high purity H_2 and N_2 gases were controlled with AALBORG GFC 2000 H_2 and N_2 flow meters. Before each sintering experiment, N_2 gas was purged into the furnace for 10 min starting with 0.5 l/min flow rate to obtain an oxygen free atmosphere. During all sintering steps, dry H_2 was purged with 0.5 l/min into the tube furnace. A gas bubbler unit checked the continuity of the gas flow. The schematic drawing of the sintering furnace setup is given in Figure 27. All sintering experiments were performed by applying the same temperature-time profile shown in Figure 28.

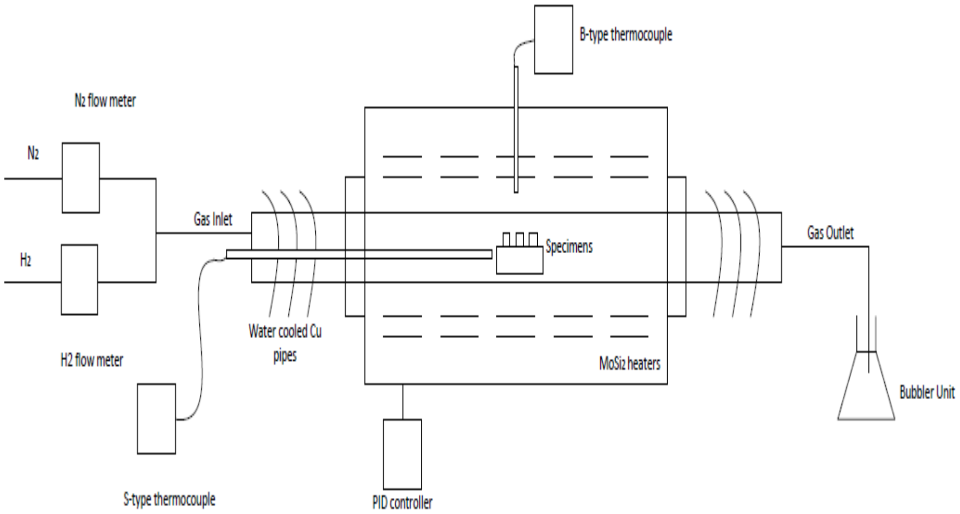

Figure 27 Schematic drawing of the sintering furnace setup

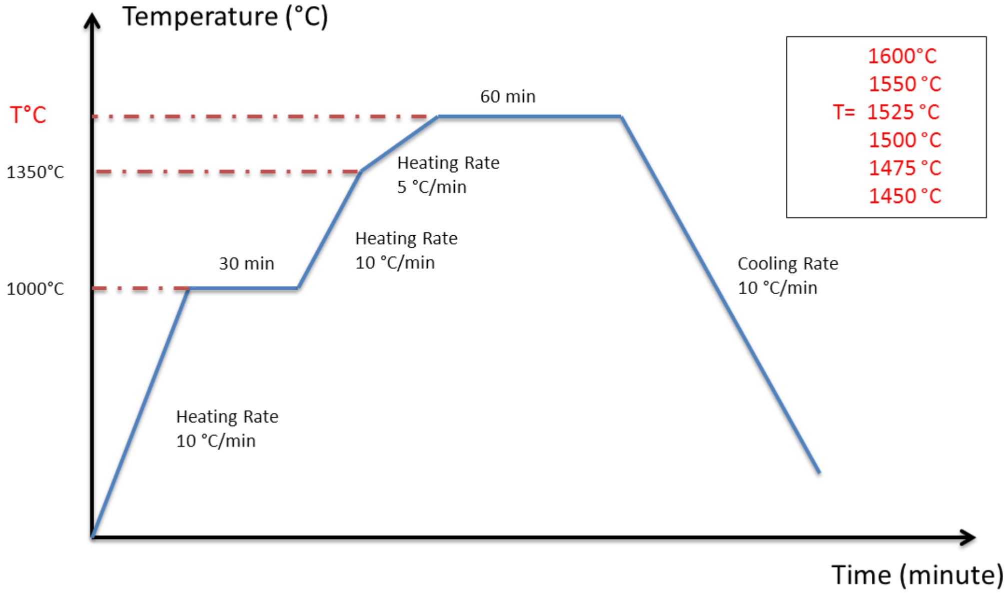

Figure 28 Temperature-time profile applied for the sintering experiments

3.2 Characterization Studies of W-Ni-Co Alloys

W-Ni-Co alloys investigated in the study were analyzed by using suitable structural, physical and mechanical characterization techniques. For structural characterization, metallographic preparation and microstructural examination studies were done. Metallographically prepared specimens were examined both under an optical microscope and in a scanning electron microscope (SEM). Microstructure images were used to analyze the average W grain size and aerial phase percentages. For other structural, physical and mechanical characterization studies, density, hardness and X-ray diffraction measurements were applied to the sintered specimens. The details of the characterization studies applied on the investigated alloys are described in the following subsections.

3.2.1 Microstructural Characterization

3.2.1.1 Metallographic Sample Preparation

Sintered W-Ni-Co alloy specimens were prepared for microstructural characterization by applying conventional metallographic methods. Specimens were mounted into 30 mm diameter bakalite disks separately with a hot mounting machine (Struers LaboPress-1) in order to obtain uniformity of specimens.

Mounted specimens were ground with resin bonded diamond discs with 220 and 1200 grit. Polishing was done with 0.3 μm alumina for about 15 minutes on a suitable textile disc. All grinding and polishing steps were carried out in a Struers Tegramin-25 semi-automatic metallographic preparation system.

As the etchant, Murakami’s solution was used. Murakami’s solution was prepared by using 10 g $K_3Fe(CN)_6$ (potassium ferricynanide), 10 g NaOH and 100 ml H_2O in accordance with the recipe given in ASTM 98C. Specimens were swabbed into the etchant for 2 to 15 seconds to get a suitable surface, rinsed with water and alcohol and then dried with hot air.

3.2.1.2 Microstructural Examination

Microstructural examination of the sintered W-Ni-Co alloy samples were carried out for the following purposes:

a. to reveal and identify the microstructural constituents
b. to determine the aerial percentages of the constituent phases
c. to determine the average size of the W grains

The microstructures of the specimens were examined with both an optical microscope and SEM. Metallographic examinations were done by a Zeiss Axioskop 2 Mat optical microscope using different magnifications ranging from 50 to 1000x.

AxioCam MRC-S camera and AxioVision software were used to take colored and black-white micrographs of the specimens.

SEM analyses were carried out in a JEOL 6400 JSM SEM operated at 20 kV. Secondary and backscattered electron imaging modes were applied to get topographical and compositional contrast, respectively. Energy dispersive spectroscopy (EDS) analyses were done for all the samples by using the Northern Tracor EDS system equipped within the SEM. For selected samples, line scan analysis were done with the EDS analyzer with 2500x magnified images on a 30 -35 µm length line which encompassed the different constituent phases.

Multiphase analyses were performed with a Zeiss AxioVision software in accordance with ASTM E112 standard. To determine the percent area of the binder matrix phase, the software analyzes the different colors on the micrographs and calculates the percent phase content separately.

Grain size analyses were performed by using Jefferies (Planimetric) method based on ASTM E112 standard. According to this method, a circle is drawn on the microstructural image that has 5000 mm^2 area. The image should be resized to 10000 mm^2 without changing the aspect ratio, which is 4:3. The circle is placed on the resized image randomly and both inside and intercept grains were counted. In order to calculate the number of grains per square millimeter at 1x magnification, N_A, Equation 6 given below should be used.

$$N_A = f\left(N_{inside} + \frac{N_{intercept}}{2}\right) \tag{6}$$

In Equation 6, N_{inside} is the number of grains inside the circle completely, $N_{intercept}$ is the number of grains that intercept the circle and f is the Jefferies' multiplier. In this study, the grain size analyses were performed at 200x magnification and f for this magnification is 8.0. The average grain area, Ā, is calculated from the following equation, Equation 7;

$$\bar{\text{A}} = \frac{1}{N_A} \tag{7}$$

In order to calculate the mean grain diameter in millimeters, d; one should take the square root of Ā. Average grain size measurements were done three times for each microstructural images.

Within the scope of the thesis study, an attempt has also been made to determine the W grain size distribution of selected alloy samples. For this purpose, the distribution of the W grain sizes was measured from randomly selected 80 grains on a SEM image at 300X magnification, for each selected alloy sample. The diameter of these grains were measured in millimeters with a ruler and then converted to the micron value in accordance with the scale of the SEM image. The grain size distribution curves for the investigated alloy samples were constructed based on 5 µm grain size intervals.

3.2.1.3 X-Ray Diffraction Analyses

X-ray diffraction (XRD) analyses were applied to selected Ni-rich and Ni/Co ratio 1/1 alloys in order to determine the crystal structure and lattice parameter of the constituent phases. X-ray diffractograms were taken from a Rikagu X-Ray Diffractometer operated at 40 kV with Cu K_{α} X-ray beam source. XRD experiments were performed by applying a continuous scan between 5° and 90° 2θ angles at a scan rate of 2°/min.

The lattice parameters of the constituent phases were determined by using Bragg's law, which is given in Equation 8 below:

$$n\lambda = 2d\sin\theta \tag{8}$$

In Equation 8, n is the order of diffraction, λ is X-ray wavelength ($\lambda_{Cu.K\alpha}$ is 1.5406 nm), d is interplanar spacing and θ is diffraction angle. For cubic crystal system, interplanar spacing (d) can be written as:

$$d_{hkl} = \frac{a_0}{\sqrt{h^2+k^2+l^2}} \tag{9}$$

where a_0 is the lattice parameter. By using Equation 9, Bragg's law can be rewritten in a different form as:

$$\lambda^2 = 4d^2 sin^2\theta = \frac{4a_0^2}{(h^2+k^2+l^2)} sin^2\theta \tag{10}$$

and Equation 10 can be turned into:

$$\frac{sin^2\theta}{(h^2+k^2+l^2)} = \frac{\lambda^2}{4a_0^2} \tag{11}$$

where $(h^2 + k^2 + l^2)$ is always equal to an integer and $\frac{\lambda^2}{4a_0^2}$ is constant for a given crystal structure. For cubic crystal system which includes simple cubic (SC), body centered cubic (BCC), face centered cubic (FCC) and diamond cubic structures, characteristic line $(h^2 + k^2 + l^2)$ sequences are given in Table 8. For the alloys investigated in the study, Bragg's law was used to determine the lattice parameters of the constituent phases that were found to have a cubic crystal structure, based on the above discussion. No attempt has been made to determine the lattice parameters of the constituent phases having other crystal structures.

Table 8 Characteristic Line Sequences for Cubic Crystal System

Crystal Structure	Characteristic Line $(h^2 + k^2 + l^2)$ Sequence
Simple Cubic	1, 2, 3, 4, 5, 6, 8, 9, 10, 11, 12, 13, 14, 16….
Body Centered Cubic	2, 4, 6, 8, 10, 12, 14, 16,……
Face Centered Cubic	3, 4, 8, 11, 12, 16, 19, 20, 24, 27, 32,…….
Diamond Cubic	3, 8, 11, 16, 19, 24, 27, 32,…….

3.2.2 Physical and Mechanical Characterization

3.2.2.1 Density Measurements

The density measurements were carried out to determine the relative densities as well as the densification parameters of the sintered W-Ni-Co alloy samples. The densities of the specimens were measured by making use of the fundamental Archimedes' principle. For these measurements, a Sartorius CP224S Precision Balance with a density measurement kit was used, which has 0.1 mg readability capacity. The density measurements were performed by using xylene liquid instead of water to get rid of air bubbles and acquire higher wetting capacity. Xylene has 0.865 g/cm^3 density at room temperature. The density measurement steps are described below;

- The sintered specimen is lightly ground with coarse emery paper in order to eliminate occasional surface contaminants coming from the sintering tray,
- The mass of the cleaned specimen is determined in air (m_{air}),
- The specimen is held for one day in xylene so that all of the open pores become saturated with liquid,
- After saturation of the open pores, the specimen is fully immersed into xylene in order to measure the buoyancy force (m_{liquid}),
- The specimen is cleaned with a napkin quickly and then weighed again to determine the saturated mass ($m_{liquid-air}$),
- The density of the specimen can be calculated by using Equation 12 given below.

$$\rho = \frac{m_{air}}{(m_{liquid-air} - m_{liquid})} x \, \rho_{xylene} \tag{12}$$

The relative density of the alloy samples can be calculated by dividing the measured density by theoretical density. For the calculation of the theoretical density, the general rule of mixtures can be used by applying some simple assumptions such as all specimens are homogenous and have no pores in their microstructures. With these assumptions, the theoretical density can be calculated from Equation 13 given below, where W_{wf}, Ni_{wf}, Co_{wf} donate the weight fractions of W, Ni and Co respectively:

$$\frac{1}{\rho_{theo}} = \frac{W_{wf}}{\rho_W} + \frac{Ni_{wf}}{\rho_{Ni}} + \frac{Co_{wf}}{\rho_{Co}} \tag{13}$$

In addition, the densification parameter (Ψ) of the samples can be calculated by using sintered, green and theoretical densities and applying Equation 14 given below:

$$\Psi = \frac{Sintered\ density - Green\ density}{Theoretical\ density - Green\ density} \tag{14}$$

The theoretical densities of the investigated W-Ni-Co alloys were determined by using Equation 13 and were presented in Table 7 earlier.

3.2.2.2 Hardness Tests

Hardness tests were applied to the sintered specimens in a Struers Duramin 500 Universal Hardness Tester with Vickers diamond indenter. Hardness tests were performed at 98.10 N load for 5 seconds. A 320.5X camera lens was used to observe the traces of the indents. Three measurements were taken for each alloy specimen and the average value of the hardness results were reported with HV10 scale.

CHAPTER 4

RESULTS AND DISCUSSION

In this study, the effects of composition and sintering parameters on the microstructure and characteristics of selected W-rich W-Ni-Co heavy alloys were investigated. The effects of these variables were evaluated in terms of their influence on selected material characteristics, namely; density, average W grain size, solubility of W in the binder phase, binder percent area, and hardness. These material characteristics were determined by applying suitable characterization techniques whose procedures are described in detail in Chapter 3. In what follows, the results of the thesis study are presented and discussed.

The W-Ni-Co alloys investigated were prepared with different W contents; namely 90, 92, 95 and 97 % W. For 90 and 95 % W, alloys with 1/4, 1/1, 3/1, 4/1 and 6/1 Ni/Co ratio were prepared. Moreover, Ni/Co ratio 1/1 and 4/1 alloys were prepared for 92 and 97 % W in order to investigate the effect of W content further. The investigated alloys were fabricated by applying powder metallurgy techniques. Alloy samples were compacted with cold isostatic pressing under 310 MPa, and then sintered at different temperatures ranging from 1450°C to 1600°C for 1 hour under H_2 atmosphere.

The green and sintered densities of the alloy specimens were measured with Archimedes method, as described in the previous chapter in detail. For each alloy composition, two specimens were prepared and their densities were measured in both green and sintered condition. The relative density (% RD) of the alloy samples were determined by dividing the measured density with the theoretical density, and multiplying by 100. The calculated % RD of the investigated alloys which were sintered at different temperatures are listed altogether in Table 9. In addition, measured green and sintered densities are given in Appendix A. The variation of % RD with sintering temperature and Ni/Co ratio for 90 % and 95 % W alloys are given in Figures 29 and 30, respectively.

Table 9 Relative Densities (%RD) of the Investigated W-Ni-Co Alloys

Alloy Code	**Sintering Temperature (°C)**					
	1450	1475	1500	1525	1550	1600
	Relative Density (%)					
0W14	78.0	81.9	82.0	87.3	92.3	100
0W11	98.5	100	100	98.5	99.9	99.4
0W31	98.8	99.5	99.3	100	99.9	99.2
0W41	98.4	99.2	97.1	98.4	99.6	100
0W61	97.9	99.7	99.2	99.9	99.9	99.0
2W11	97.9	99.7	99.1	99.4	99.7	99.8
2W41	99.5	99.1	97.7	99.4	99.5	99.5
5W14	80.9	82.8	86.0	89.2	92.9	100
5W11	95.5	99.3	100	99.3	99.6	100
5W31	96.9	99.4	99.2	100	99.8	99.7
5W41	94.0	97.1	99.9	98.8	99.4	99.8
5W61	95.3	99.5	99.4	99.9	99.8	99.2
7W11	95.5	99.9	99.3	99.8	99.4	99.9
7W41	99.3	99.5	99.4	99.7	99.2	99.8

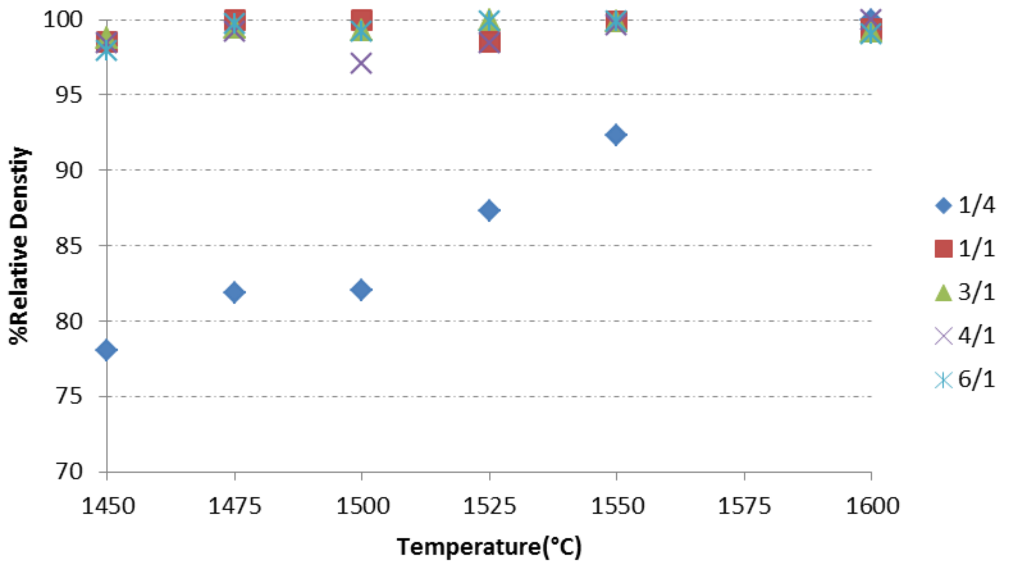

Figure 29 The variation of the relative density with sintering temperature and Ni/Co ratio for 90 % W alloys.

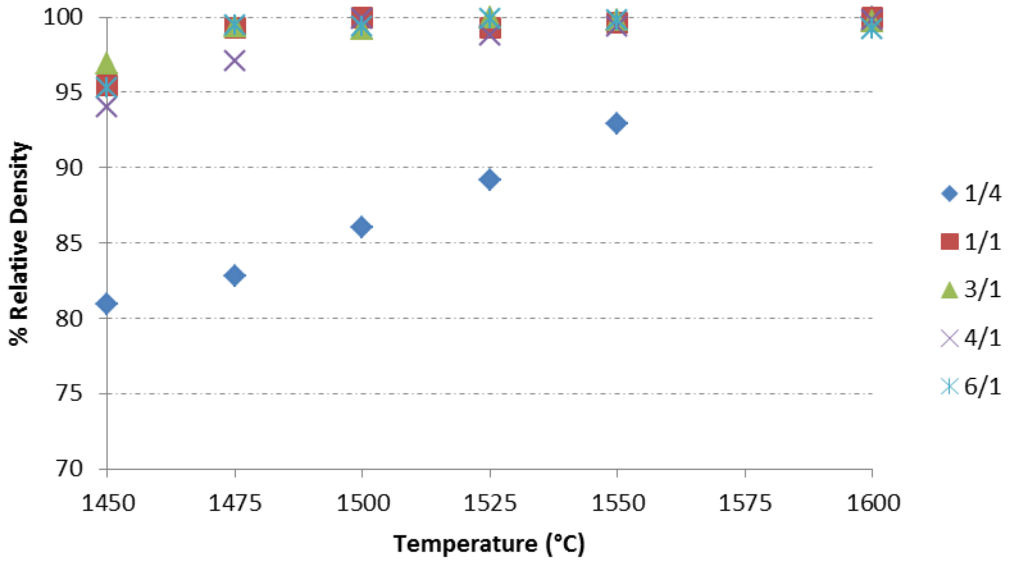

Figure 30 The variation of the relative density with sintering temperature and Ni/Co ratio for 95 % W alloys.

As can be seen clearly in Table 9 and Figures 29 and 30, the densification of Co-rich alloys with Ni/Co ratio 1/4, namely alloys 0W14 and 5W14, is limited, when sintered at and below 1550°C. However, for both 90 and 95 % W, the density of these Co-rich alloys was observed to increase with increasing sintering temperature and reach full density when sintered at 1600°C. On the other hand, all Ni-rich and Ni/Co ratio 1/1 alloys were seen to reach almost full density when sintered at and above 1475°C, independent of alloy W content and sintering temperature.

As can be seen in Table 9 and Figures 29 and 30, the densification of Co rich alloys with Ni/Co ratio 1/4 is strongly dependent on the sintering temperature, and slightly but obviously dependent on the alloy W content. In order to provide visual comparison, the variation of % RD with sintering temperature and alloy W content is given in Figure 31 for these alloys. Figure 31 shows that the relative density of both 90 and 95 % W alloys (alloys 0W14 and 5W14) increases monotonously with increasing sintering temperature. In addition, the density of the 95 % W alloy (alloy 5W14) is seen to be greater at all sintering temperatures except 1600°C, when compared to the 90 % W alloy (alloy 0W14). The reason for this behavior might be explained as follows: Sintering is, in general, a diffusion controlled process. Temperature and composition have a strong influence in determining the kinetics of any diffusional process. In general, the temperature dependence of diffusional processes is exponential, meaning that increasing the temperature has a significant effect in enhancing the rate of such processes. Therefore, the densification rate in a sintering operation is expected to increase with increasing temperature, and this is the case observed in the study for the 90 and 95 % W Co-rich alloys. For these alloys, the interpretation of the compositional dependence of the densification behavior on alloy W content is not straightforward. This is because the sintering process in these alloys is somewhat complex due to the simultaneous or sequential occurrence of diffusional homogenization, intermetallic compound formation and other sintering mechanisms. However, a reasonable explanation for this behavior might be suggested within the scope of the study as follows. Alloy 5W14 has higher W content when compared to alloy 0W14. This means that there will be much more W powder particles per unit volume in alloy 5W14 both in the green condition, and during the initial stages of sintering. Moreover, based on phase diagram considerations, the total amount and volume percentage of the solid binder phase is expected to be lower in

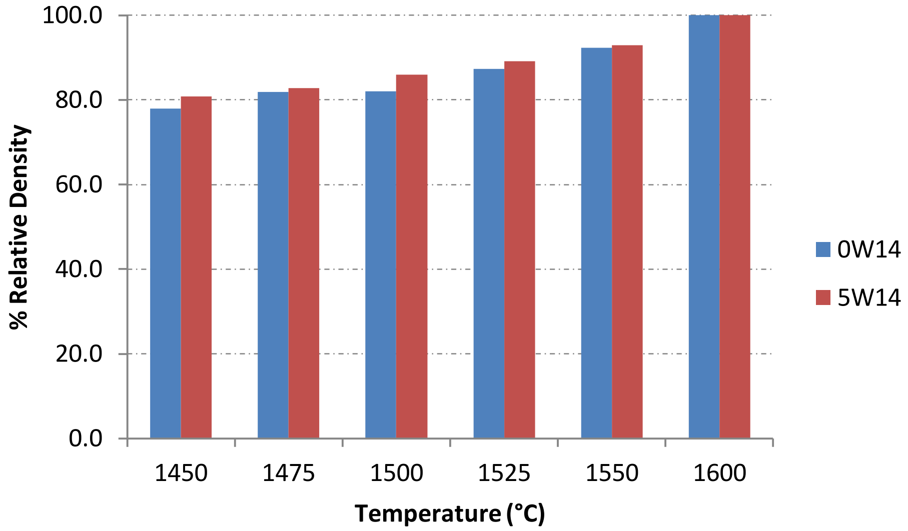

Figure 31 The variation of the relative density with sintering temperature and alloy W content for 0W14 and 5W14 cobalt-rich alloys

alloy 5W14 when compared to alloy 0W14, at any given temperature. These two facts together imply that, at any given sintering temperature, the mean free path among the W particles will be shorter, and that contact and neck formation among W and Ni or Co particles may be easier in alloy 5W14. As a result, all diffusional mass transport processes might take place over shorter distances in alloy 5W14, and this might enhance the rate of such processes. This may be the reason why alloy 5W14 gets more densified when compared to alloy 0W14 at a given sintering temperature.

Green and sintered densities of samples were measured for all compositions and sintering temperatures covered in this study. By using these density measurements, the densification parameter can be calculated as German stated in his book [5]. From Equation 14 given in Chapter 3, the densification parameters were calculated for 90 % W alloys sintered at temperatures ranging between 1450°C and 1600°C and the results are given in Figure 32. As can be seen in Figure 32 and Figure 29, the variations of the relative density and densification parameter with sintering temperature and alloy composition show similar characteristics for 90 % W alloys. This is because all 90 % W alloys were isostatically compacted at 310 MPa and have had approximately 60-65% of theoretical density on their green condition. This is also valid for all the other alloys investigated in the study. Since the green density value is almost invariable for all of the 90 % W alloys, the only variable that determines the variation of both relative density and densification parameter is the measured sintered density. As a result, the general trend for the variation of these two parameters remains similar to each other. Since it provides no supplementary information, densification parameter determinations for the other investigated alloys are not presented in the thesis manuscript.

General microstructural features of the investigated W-Ni-Co alloys showed different characteristics. Basically, three different kinds of microstructure have been observed in the alloy samples, as given in Figure 33 to Figure 35. In addition optical microstructural images of all alloys sintered at different sintering temperatures are given in Appendix B.

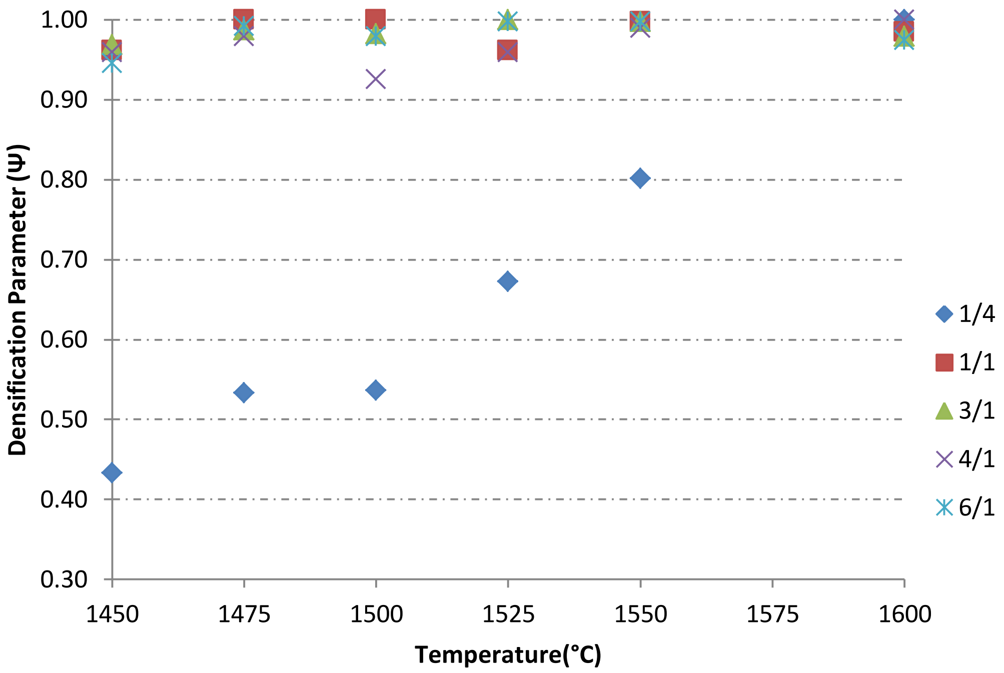

Figure 32 The variation of the densification parameter with sintering temperature and Ni/Co ratio for 90%W alloys

Firstly, Co-rich alloys which contain 1/4 Ni/Co ratio metallic addition have a completely different microstructure when compared to all other alloys investigated in the study. As it is seen in Figure 33, the microstructure of these alloys does not resemble that of usual liquid phase sintered WHAs. By considering the phase diagram characteristics, it is possible to say that higher Co content changes the sintering characteristics of the W-Ni-Co heavy alloys from LPS to solid state sintering. Microstructural examination studies have implied that Co-rich alloys have been sintered in the solid state at all the sintering temperatures applied in the study.Owing to several problems encountered in sample preparation and structural characterization, these Co-rich alloys were not studied in detail compared to Ni-rich equivalents.

Secondly, equal Ni/Co addition (1/1 ratio) was found to cause a difference in terms of the constitution of the binder matrix. For all alloys which consist of 1/1 Ni/Co ratio, the microstructure was found to consist of a two-phase binder matrix, although these alloys were sintered by LPS. As will be discussed later, this two-phase binder matrix was found to affect one material property of the W-Ni-Co alloys significantly, namely the hardness. The representative microstructure for the Ni/Co ratio 1/1 alloys is given in Figure 34.

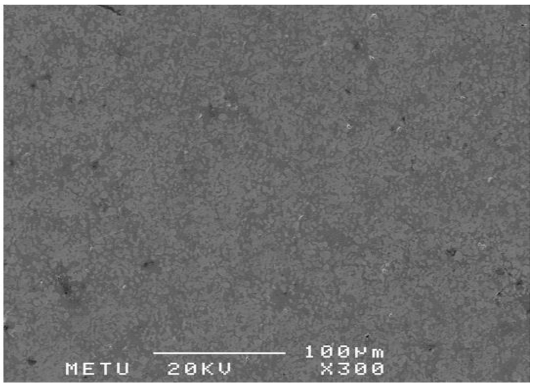

Figure 33 Typical microstructure of Co-rich alloys: Microstructure of 0W14 alloy sintered at 1500°C, SEM secondary electron image, 300x

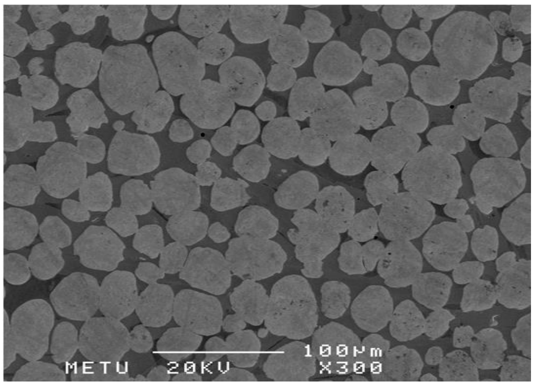

Figure 34 Typical microstructure of Ni/Co ratio 1/1 alloys: Microstructure of 2W11 alloy sintered at 1500°C, SEM secondary electron image, 300x

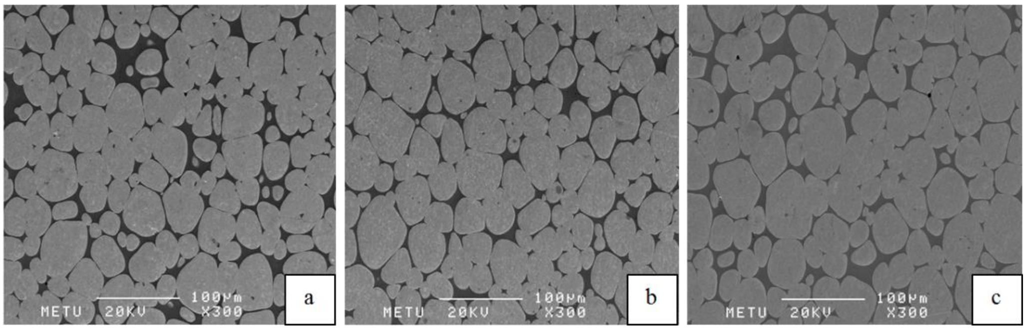

Figure 35 Typical microstructures of Ni-rich alloys: Microstructures of; a) 5W31, b) 5W41, c) 5W61 alloys sintered at 1500°C, SEM secondary electron images, 300x

Finally, the microstructure of the Ni-rich alloys, namely the alloys with Ni/Co ratio 3/1, 4/1 and 6/1, was typical of LPS sintered WHAs. The composite microstructure in these alloys contains nearly pure, rounded W grains and a W dissolved Ni-Co binder matrix phase. The typical microstructures for the Ni-rich alloys are given in Figure 35. Ni-rich and Ni/Co ratio 1/1 alloys sintered at and above 1475°C were observed to have microstructures typical of liquid phase sintered tungsten heavy alloys (WHAs). This strongly implies that these alloys were sintered in the presence of a liquid binder matrix phase at these sintering temperatures. Therefore, with the aid of microstructures and relative density results of the study strongly suggest that liquid phase sintering (LPS) dramatically enhances the densification behaviour of W-rich W-Ni-Co alloys, when compared to solid state sintering.

The compositions of the constituent phases were determined with EDS analysis for the investigated alloys. EDS analysis cannot be applied to the alloys sintered at 1450°C successfully due to the fineness and complexity of the observed microstructures. The EDS analyses results of the investigated W-Ni-Co alloys are presented in Table 10 and Table 11. In these tables, only the analysis results of the binder matrix phases were given. The EDS results have shown that the W grains existing in the microstructure of the investigated alloys were almost pure W in all cases, therefore the analysis results for this constituent phase were not presented in Tables 10 and 11.

In Table 11, the EDS data for the Ni/Co ratio 1/1 alloys is given separately, because these alloys were found to consist of a two-phase binder matrix, as also mentioned before. Within the thesis manuscript and Table 11, the two phases of the binder matrix of these alloys were termed as “gray” and “black” respectively, mainly based on their appearance in the SEM backscattered electron images. As known, in the SEM backscattered electron imaging mode, image contrast is mainly determined by compositional differences. In this mode, regions of the microstructure that are composed of “heavier” atoms produce “brighter” contrast when compared to other regions. In this context, the phase termed as “gray” in the manuscript contains the “heavy” element W more than the “black” phase, as also seen in Table 11.

Some difficulties were faced while analyzing the binder matrix phases for higher W content alloys due to the lower quantity of the binder matrix phase. Therefore, due to the difficulty in distinguishing the phases in the microstructure, EDS measurements cannot be performed for some of those alloys.

When the results of the EDS analyses are evaluated together with the microstructural examination results, it can be seen from Table 10 that the binder matrix phase of the investigated Ni-rich alloys (alloys with Ni/Co ratio 3/1 to 6/1) consists of a Ni-Co-W solid solution. For Co-rich alloys with Ni/Co ratio 1/4, on the other hand, the wt% W in the binder phase is almost invariably constant around 75 %, independent of the sintering temperature or alloy W content. The binder phase composition of these alloys given in Table 10 in wt% corresponds to the Co_7W_6 intermetallic compound phase in atomic percentages (at%), which contains approximately 5 wt% Ni in it, seeming to substitute Co in the crystal structure. Based on phase diagram data, the binder phase in the Co-rich W-Ni-Co alloys is expected to include the Co_7W_6 phase, and the EDS analyses data obtained in the thesis study has shown that this is the case. Finally, for the alloys with Ni/Co ratio 1/1, EDS analyses data given in Table 11 have shown that the “black” phase of the binder matrix of these alloys is a Ni-Co-W solid solution, and the “gray” phase is Co_7W_6 intermetallic compound with 10-12 wt% Ni in it, seeming to substitute Co in the crystal structure.

Compiled from the EDS analyses results given in Tables 10 and 11, the graph of wt% W in binder phase changing with sintering temperature and Ni/Co ratio for 90 and 95 % W alloys are given in Figure 36 and Figure 37, respectively. In these figures, only the data pertaining to the “black” phase has been presented for the Ni/Co ratio 1/1 alloys. As it is seen in these figures, there is a small change in the wt% W in the binder phase with increasing sintering temperature. The values are ranging between 35 to 43 % W, except for the Co-rich Ni/Co ratio 1/4 alloys. As mentioned before, the wt% W in the binder phase is almost invariably constant around 75 % for these alloys, and this value corresponds to the W content of the Co_7W_6 phase.

Figure 36 and Figure 37 also reveal that the variation of wt% W in the binder phase is small for changing Ni/Co ratio for Ni-rich and Ni/Co ratio 1/1 alloys. In Figure 38, the variation of dissolved wt% W in the binder phase with Ni content is depicted for

90% W Ni-rich and Ni/Co ratio 1/1 alloys. It is again found that, for the same alloy composition, for example 0W61, increasing the sintering temperature does not change the W content of the binder matrix phase dramatically. The EDS analyses results imply that the dissolution of W in the binder phase was completed during the sintering process, and that further increment in temperature has a slight effect on the solubility of W in the binder phase.

In order to check whether there were non-uniform compositional variations within the microstructure or not, EDS line scan analyses were performed on selected Ni-rich and Ni/Co ratio 1/1 alloys. EDS line scan analysis of 0W61 and 0W11 alloys sintered at 1500°C are shown in Figure 39 and Figure 40, respectively. For 0W61 alloy, EDS line scan analysis were taken through W grains and binder matrix phase. In Figure 39, some background noise has been observed due to the limitations of the EDS detection system. Owing to the scattering nature of X-Rays near the analyzed field, some Ni and Co were artificially observed in W grains. This is known to be in contradiction with the EDS point analysis of W grain that is pure W, and does not represent the real case. On the other hand, EDS line scan analysis has proven that the

Table 10 Composition of the Binder Matrix Phase in Co-Rich and Ni-Rich W-Ni-Co Alloys Determined by EDS Analyses

	Sintering Temperature (°C)														
	1475			1500			1525			1550			1600		
	Composition (wt%)														
Alloy	W	Ni	Co	W	Ni	Co	W	Ni	Co	W	Ni	Co	W	Ni	Co
0W14	76.70	4.68	18.62	76.70	4.68	18.62	73.75	5.07	21.19	75.10	4.86	20.04	73.12	5.27	21.61
0W31	39.06	45.55	15.39	38.90	45.66	15.45	43.10	43.12	13.78	42.23	43.28	14.49	41.11	43.88	15.02
0W41	39.27	48.34	12.40	39.56	48.36	12.08	36.71	49.40	13.89	39.56	48.01	12.43	42.11	46.13	11.76
0W61	38.56	52.57	8.87	38.11	53.03	8.86	41.13	50.37	8.50	40.15	51.14	8.71	39.86	51.42	8.72
2W41	35.70	52.12	12.18	37.43	49.51	13.06	34.70	51.77	13.52	41.48	46.61	11.91	38.35	48.77	12.87
5W14	72.40	5.80	21.80	77.25	4.37	18.38	74.33	5.19	20.48	75.19	5.00	19.51	75.07	5.39	19.54
5W31	38.74	46.27	15.00	35.90	48.45	15.66	40.56	45.37	14.07	41.34	44.42	14.24	41.49	44.15	14.36
5W41	36.78	50.34	12.89	38.91	49.05	12.04	32.98	53.00	14.02	42.08	46.41	11.51	42.82	45.51	11.67
5W61	35.53	55.46	9.01	36.24	54.63	9.13	41.63	50.13	8.24	41.08	50.86	8.06	41.85	50.21	7.95
7W41	36.61	49.68	13.70	36.73	49.94	13.32	32.39	53.59	14.02	39.51	48.41	12.08	40.27	47.83	11.90

Table 11 Composition of the Binder Matrix Phase in Ni/Co Ratio 1/1 W-Ni-Co Alloys Determined by EDS Analyses

		Temperature (°C)														
		1475			1500			1525			1550			1600		
		Composition (wt%)														
Alloy	Phase	W	Ni	Co	W	Ni	Co	W	Ni	Co	W	Ni	Co	W	Ni	Co
0W11	gray	74.72	10.04	15.24	74.36	9.54	16.10	75.14	10.36	14.50	74.66	10.28	15.05	73.81	10.49	15.71
	black	41.10	38.08	20.82	42.09	34.60	23.31	39.68	41.91	18.41	41.83	32.78	25.39	43.35	30.21	26.44
2W11	gray	74.69	12.14	13.17	74.57	11.72	13.72	74.31	11.41	14.28	74.90	10.72	14.39	74.51	9.42	16.07
	black	40.14	41.29	18.57	36.65	45.29	18.07	39.34	40.47	20.19	41.72	33.81	24.47	41.47	34.08	24.45
5W11	gray	74.88	10.93	14.19	73.62	11.31	15.06	75.19	12.59	12.22	75.10	11.13	13.77	-		
	black	42.01	35.04	22.95	42.81	34.50	22.70	34.60	47.13	18.26	35.75	45.41	18.84	42.44	32.49	25.07
7W11	gray	73.65	11.02	15.32	-			75.12	12.29	12.59	74.96	10.25	14.79	73.84	10.76	15.40
	black	35.99	43.55	20.46	37.71	43.98	18.31	38.34	43.44	18.22	-			39.32	35.69	24.99

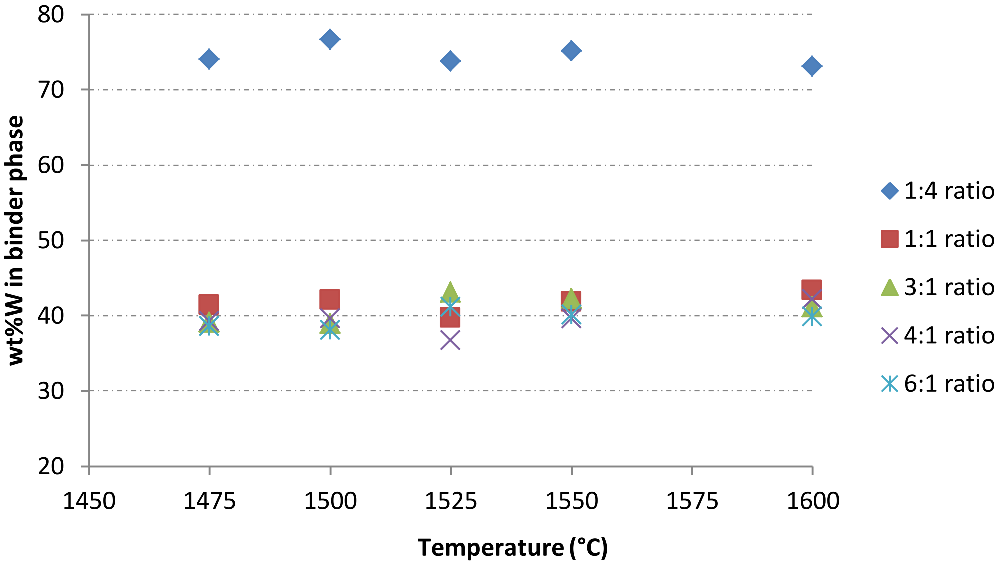

Figure 36 wt% W in binder phase variation with sintering temperature and Ni/Co ratio for 90%W alloys

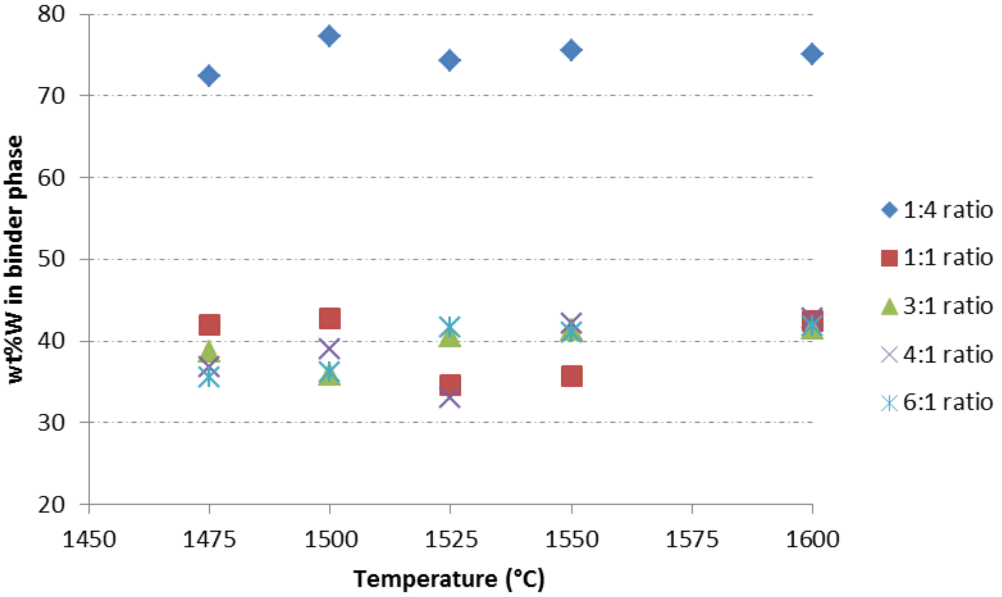

Figure 37 wt% W in binder phase variation with sintering temperature and Ni/Co ratio for 95%W alloys

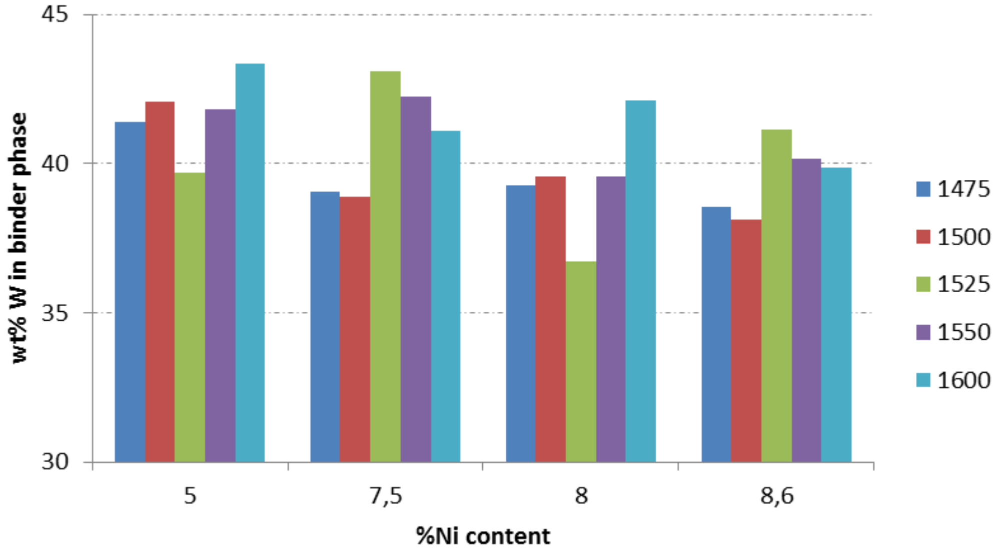

Figure 38 The variation of the wt % W in binder phase with % Ni content for 90% W alloys for different sintering temperatures

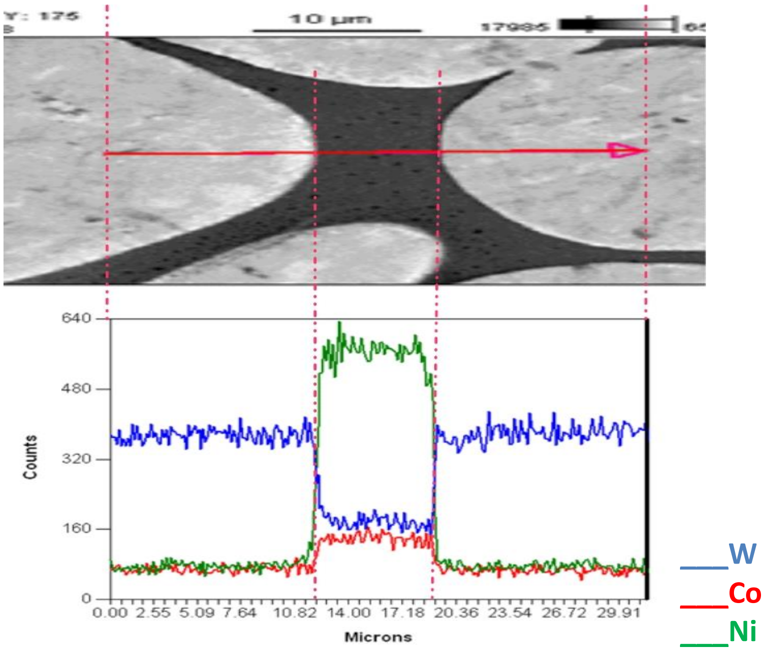

Figure 39 EDS line scan for 0W61 alloy sintered at 1500°C, 2500x magnification

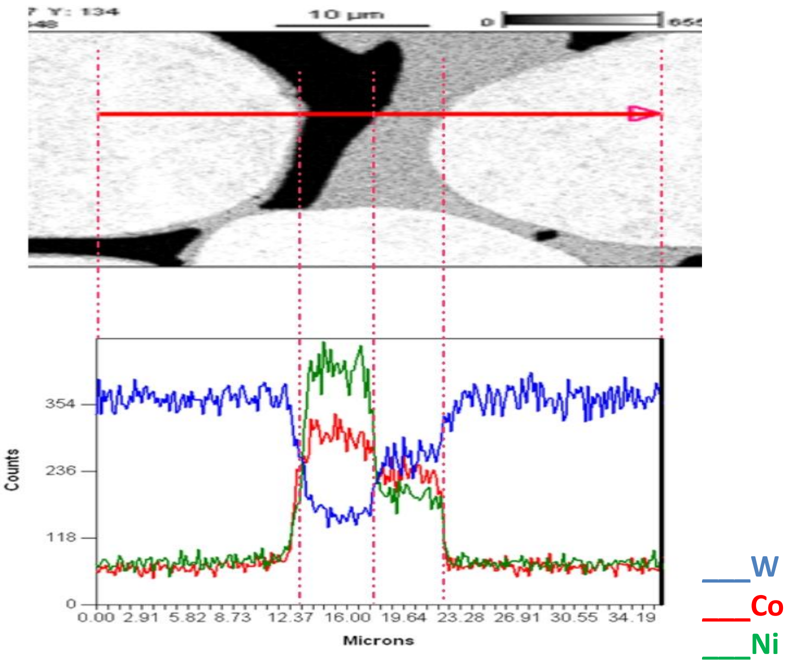

Figure 40 EDS line scan for 0W11 alloy sintered at 1500°C, 2500x magnification

dissolved W in the binder matrix phase was distributed homogeneously. In addition, across the line on the binder matrix, there were no sharp compositional gradients for either Ni or Co, meaning that these elements were also distributed homogeneously within the binder phase. As can be seen in Figure 40, EDS line scan analysis for 0W11 alloy has different characteristics compared to 0W61 due to the existence of the two-phase binder matrix. Line scan analysis for 0W11 was taken through two W grains and black and gray constituents of the binder phase. This line scan analysis also has background noise. It is clearly seen in Figure 40 that the black phase of the binder matrix contains higher amounts of Ni and Co in it. Through the gray phase, on the other hand, the amount of W has increased. As expected, this result is also supported with the EDS point analysis of black and gray phases of the binder matrix that were given in Table 11. In addition, the EDS analysis of the two-phase binder matrix has shown that W, Ni, and Co were distributed uniformly within the black and gray phases.

Another important characteristic for sintering of heavy alloys is % binder phase volume/area variation. In Figure 41 and Figure 42, the graph of % binder phase area variation with sintering temperature and Ni/Co ratio can be seen for 90 and 95% W Ni-rich alloys. In addition binder phase area measurements for selected alloys are given in Appendix C. Owing to the limitations of the software used, it was not possible to determine the % binder phase area accurately for the Co-rich and Ni/Co ratio 1/1 alloys. Therefore, these alloys were not subjected to detailed % binder phase area analyses. As can be seen in Figures 41 and 42, the % binder phase area is smaller in 95% W alloys at all sintering temperatures and Ni/Co ratios when compared to 90% W alloys. This result is expected based on solution thermodynamics and phase diagram considerations. For both 90 and 95% W alloys, the general case is that the % binder phase area increases with sintering temperature up to around 1525°C and then, with increasing temperature, the area of the binder matrix phase decreases and/or levels around a certain value. However, from thermodynamics and phase diagram considerations, for both 90 and 95% W alloys, the amount of the binder matrix phase is expected to increase monotonously with increasing temperature, even above 1525°C. It is thought that increasing the sintering temperature beyond 1525°C might distort the shape of the bulk specimens and cause “elephant leg” formation. This phenomenon can be observed in liquid phase sintered WHAs containing relatively large amounts of the liquid phase. The reason for this behavior is that there is a large difference between the densities of W grains and the liquid binder matrix phase in WHAs. Owing to this density difference, during sintering, W grains in a WHA sample can move down due to gravity and tend to agglomerate and the liquid binder phase can become exuded from the structure. In this case, microstructural examinations to be carried out within the sample may misleadingly show a structure with a lower amount of the binder matrix phase. This is thought to be the case confronted within the thesis study. Therefore, the % binder phase area results of the

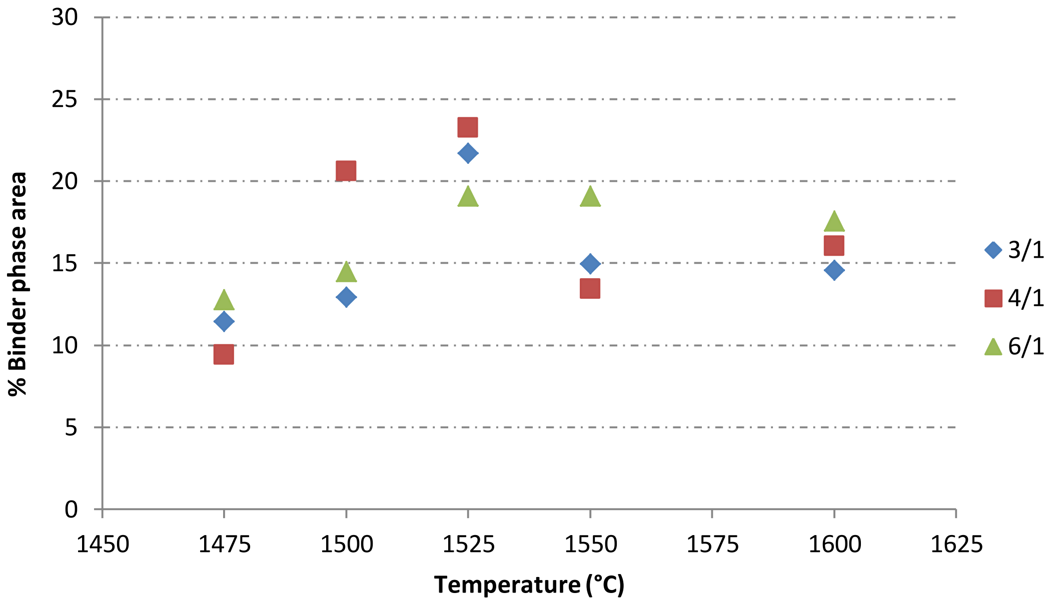

Figure 41 % binder phase area change with sintering temperature and Ni/Co ratio for 90 % W Ni-rich alloys

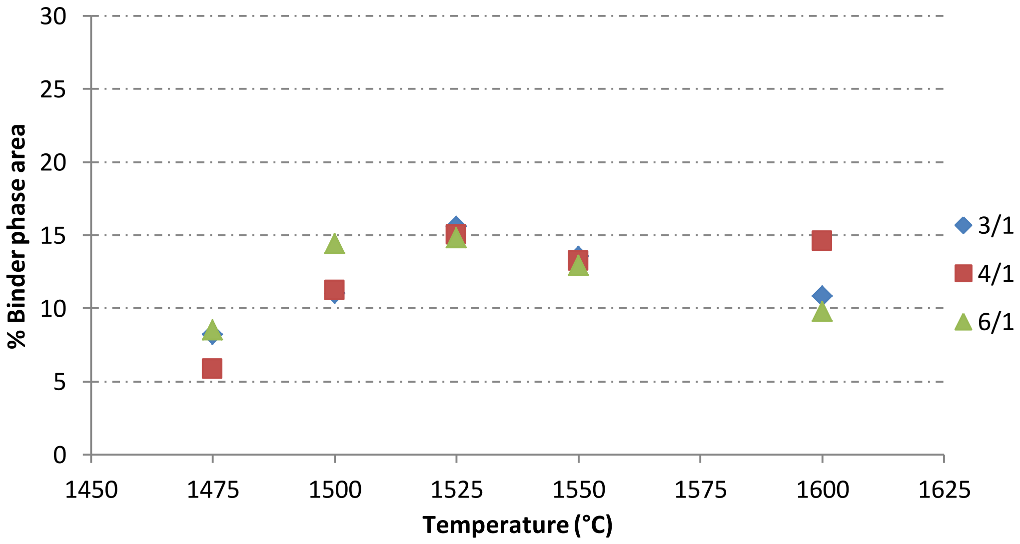

Figure 42 % binder phase area change with sintering temperature and Ni/Co ratio for 95 % W Ni-rich alloys

alloy specimens sintered beyond 1525°C in the study are believed not to reflect the real case. In this context, what is interesting is that solid-liquid segregation due to density differences is even seen in alloys with relatively high amounts of W (i.e. 95% W alloys) beyond a certain sintering temperature. This fact is important from a technological point of view, and implies that W-rich W-Ni-Co alloys should not be sintered at unnecessarily high temperatures in practical applications.

In Ni/Co ratio 1/1 alloys, microstructural examination studies have implied that the relative amounts of the “gray” and “black” phases in the two-phase binder matrix were changing both with alloy W content and sintering temperature. For providing visual comparison, representative microstructures showing the observed dependence on W content and sintering temperature are given for selected Ni/Co ratio 1/1 alloys in Figures 43 and 44 respectively. In Figure 43, it can be seen that the portion of the black part of the matrix decreases when the W content increases from 90 to 97% for the Ni/Co ratio 1/1 alloys sintered at 1500°C. This trend is generally similar for these alloys for the other sintering temperatures, especially above 1500°C. In Figure 44, the variation of the ratio of the gray and black phases with sintering temperature is depicted for the representative 0W11 alloy. As seen in the figure, the relative amount of the gray phase decreases with increasing sintering temperature for this alloy. A similar behaviour was observed for the other Ni/Co ratio 1/1 alloys investigated in the study. In conclusion, the results of the thesis study imply that the gray/black phase proportion increases with increasing W content for a given sintering temperature, and decreases with increasing sintering temperature for a given W content.

In order to understand the reason of this behavior, the ternary phase diagram characteristics of the W-Ni-Co alloy system should have to be taken into consideration. In this context, for providing visual comparison, the binary phase diagrams of Co-W, Ni-W and Co-Ni alloy systems are given in Figures 45, 46 and 47

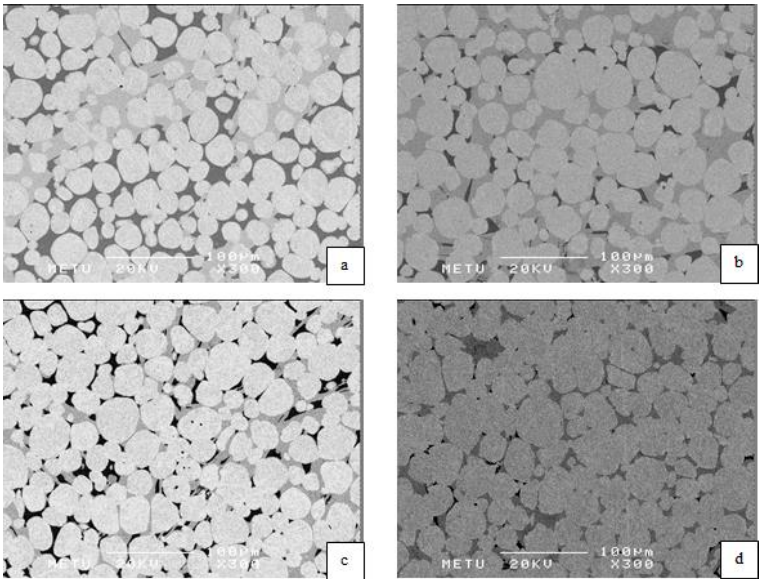

Figure 43 The variation of the gray and black phase proportions in the binder matrix with W content in Ni/Co ratio 1/1 alloys: Microstructures of; a) 0W11, b) 2W11, c) 5W11, and d) 7W11 alloys sintered at 1500°C, SEM backscattered electron images, 300x

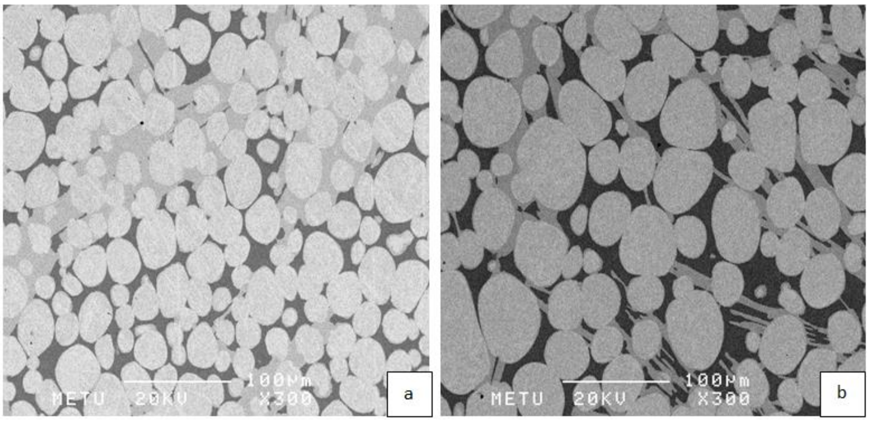

Figure 44 The variation of the gray and black phase proportions in the binder matrix with sintering temperature in Ni/Co ratio 1/1 alloys: Microstructure of 0W11 alloy sintered at; a)1500°C, b) 1600°C, SEM backscattered electron images, 300x

respectively. Unfortunately, ternary phase diagram data for the W-Ni-Co alloy system is very limited in the literature. In this respect, the phase diagram study of Gupta on this alloy system is highly valuable [32]. Gupta reported that there is no ternary intermediate phase found for the W-Ni-Co alloy system. Gupta also has given the isothermal section of W-Ni-Co alloy system at 1300°C in his work, which is shown here in Figure 48. However, isothermal sections at higher temperatures like 1400, 1500 and 1600°C cannot be found in the literature. In spite of this limitation, the results of the present thesis study strongly imply that the general appearance of the isothermal sections for higher temperatures will be very similar to the 1300°C section in the vicinity of the (α-μ-γ) three phase field, at least up to 1600°C. Therefore, the 1300°C isothermal section given in Figure 48 can cautiously be used in the interpretation of the results of the thesis study. From the 1300°C isothermal section, it can be understood that the investigated Ni/Co ratio 1/1 alloys all fall into the (α-μ-γ) three phase field, which is marked with a yellow triangle in Figure 48. In this figure, "α" corresponds to the almost pure W phase, "μ" corresponds to the Co_7W_6 phase, and "γ" corresponds to the Ni-Co-W solid solution phase. At a certain temperature higher than 1300°C, the Ni-Co-W solid solution γ phase shown in Figure 48 will be replaced with a liquid phase. Within the (α-μ-γ) three phase field, the relative amounts of the α, μ and γ phases for a given alloy composition can be found by applying phase amount calculation rules relevant to the ternary phase diagrams. In this respect, the form of the three phase triangle given in Figure 48 suggests that the relative amounts of the μ and γ phases might change with changing alloy W content. However, the proof of this suggestion requires exact phase amount determinations. For a temperature higher than 1300°C, the EDS analyses results obtained in this study imply that the composition points on the α and μ side of the three phase triangle remain approximately constant. However, the composition point on the γ (or liquid phase) side might change with increasing temperature (please refer to EDS results given in Table 11). This, in turn, might result in a change in the relative

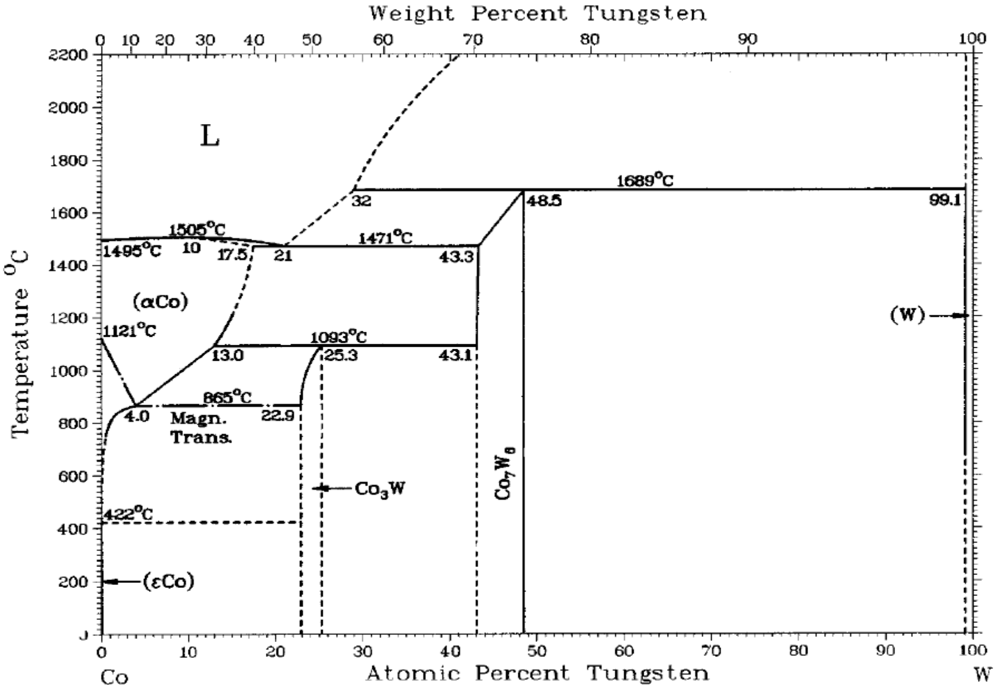

Figure 45 Co-W binary phase diagram

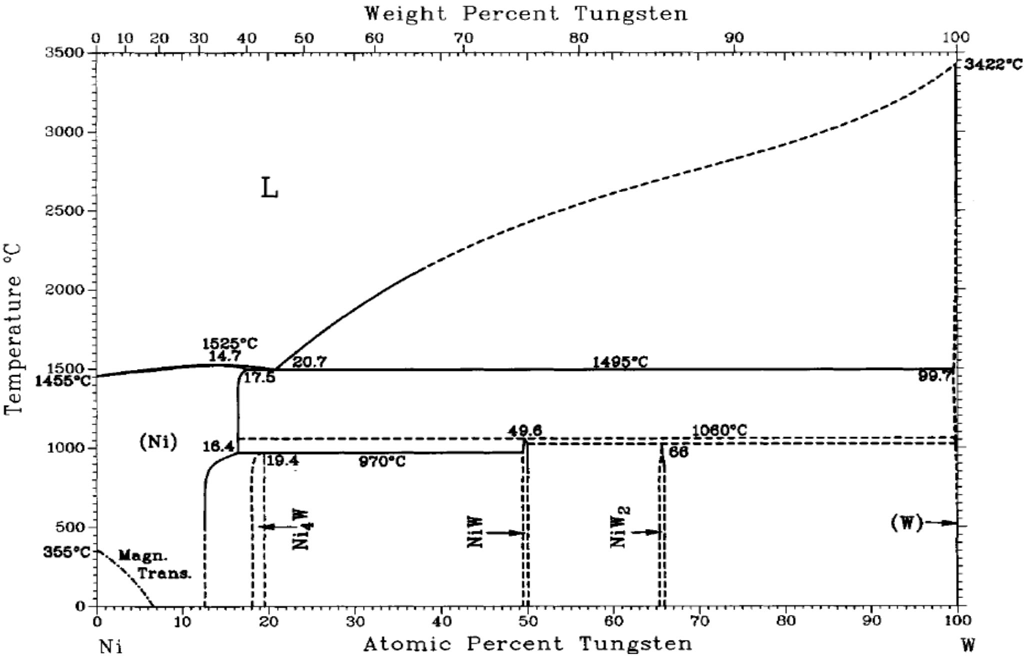

Figure 46 Ni-W binary phase diagram

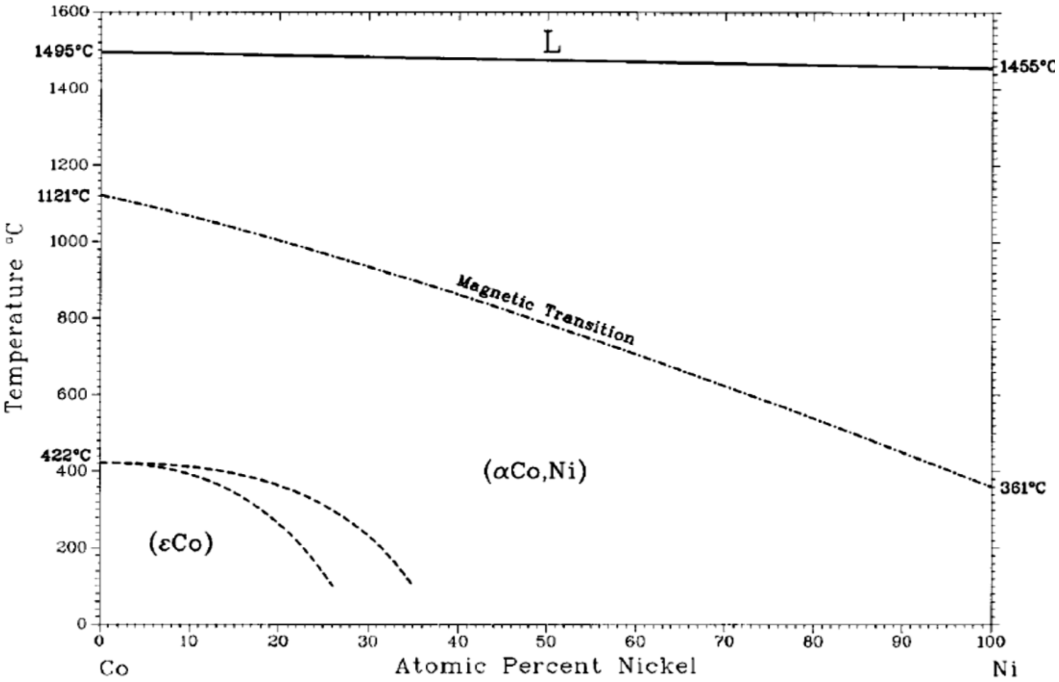

Figure 47 Co-Ni binary phase diagram

amounts of the μ and γ (or liquid) phases with increasing temperature for a given alloy composition. This suggested ternary phase diagram behaviour might explain the reasons of the gray/black phase proportion variation observed in the Ni/Co ratio 1/1 alloys. However, it should be mentioned here that the phase proportion variations observed in the thesis study were obtained in a limited sintering time interval and therefore might not represent the equilibrium case. To determine the exact nature of the phase proportion variations with either alloy composition or sintering temperature, detailed phase diagram construction experiments must be conducted, which is beyond the scope of the present study.

As mentioned before, for the Ni/Co ratio 1/1 W-Ni-Co alloys, microstructural examination studies have shown that these alloys were sintered in the presence of a two-phase binder matrix. On the other hand, the available phase diagram data

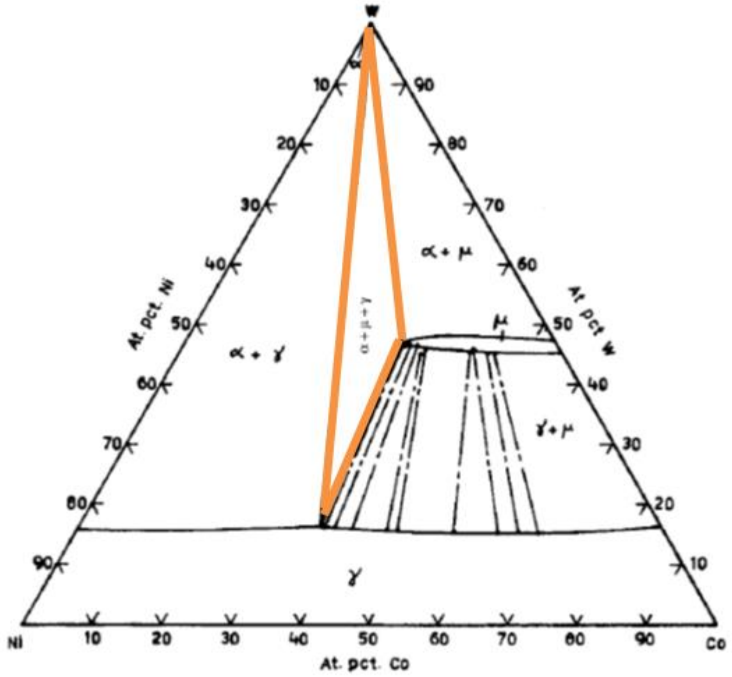

Figure 48 Isothermal section of W-Ni-Co ternary alloy system at 1300°C [32]

suggests that one phase of the binder matrix is in the liquid state, and the other in the solid state, during the sintering process at most of the sintering temperatures applied in the study. Although having been sintered under the simultaneous presence of one liquid and one solid binder phase, these alloys were found to exhibit microstructural features typical of LPS sintered WHAs. It may be suggested that this interesting sintering characteristics of these alloys deserves detailed future work.

In order to determine the crystal structure and lattice parameter of the constituent phases, X-ray diffraction method was used with Cu K_α X-ray source between 5° and 90° 2θ angle with 2 degree/min scan speed. X-ray diffraction measurements were carried out on selected Ni-rich and Ni/Co ratio 1/1 alloys. In Figure 49, X-ray diffractograms of 0W31 and 0W61 alloys sintered at 1600°C is given. As expected, X-Ray diffraction has shown that these Ni-rich alloys have consisted of almost pure

BCC W and FCC Ni-Co-W solid solution. In order to identify the nature of the gray and black phases of the binder matrix in Ni/Co ratio 1/1 alloys, X-ray diffractograms of 0W11, 2W11, 5W11 and 7W11 alloys sintered at 1500°C were used. The diffraction patterns for these alloys are presented in Figure 50 and Figure 51. It can be seen in Figure 50 and Figure 51 that the gray phase of the binder matrix is tetrahedrally close packed Co_7W_6 and the black phase is FCC Ni-Co-W solid solution. From Figure 49, Figure 50 and Figure 51, the lattice parameters of pure W grains and Ni-Co-W solid solution binder matrix phase were calculated with Bragg's law as described in Chapter 3 in detail. The lattice parameters of the Co_7W_6 intermetallic phase could not be calculated due to its complex crystal structure. The calculated and literature lattice parameter and crystal structure data for elemental W, Ni, Co, Ni-Co-W solid solution binder matrix and Co_7W_6 is given in Table 12. The lattice parameter of BCC W is found as 3.16 Angstroms and this value is identical to literature value.

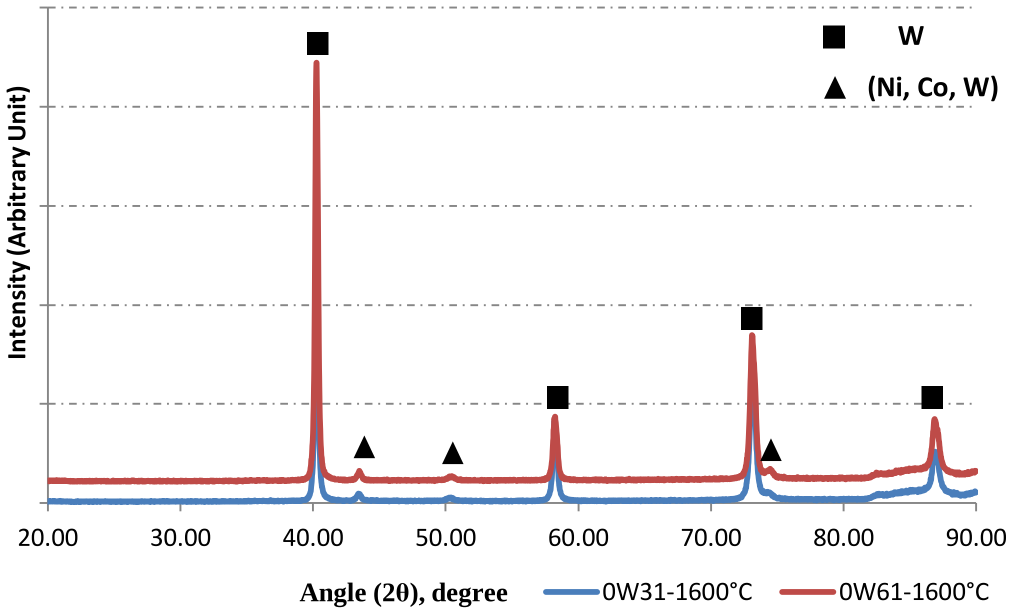

Figure 49 X-ray diffraction patterns of 0W31 and 0W61 alloys sintered at 1600°C

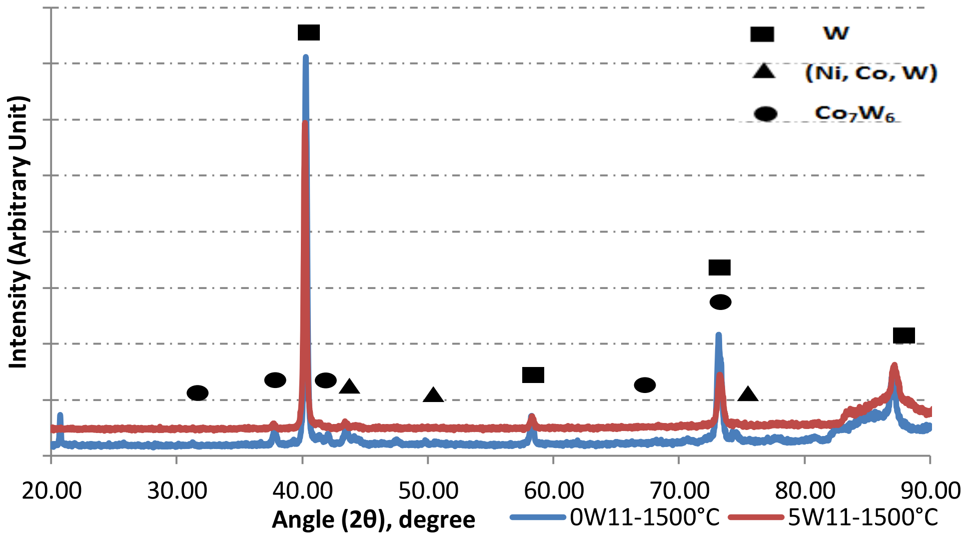

Figure 50 X-ray diffraction patterns of 0W11 and 5W11 alloys sintered at 1500°C

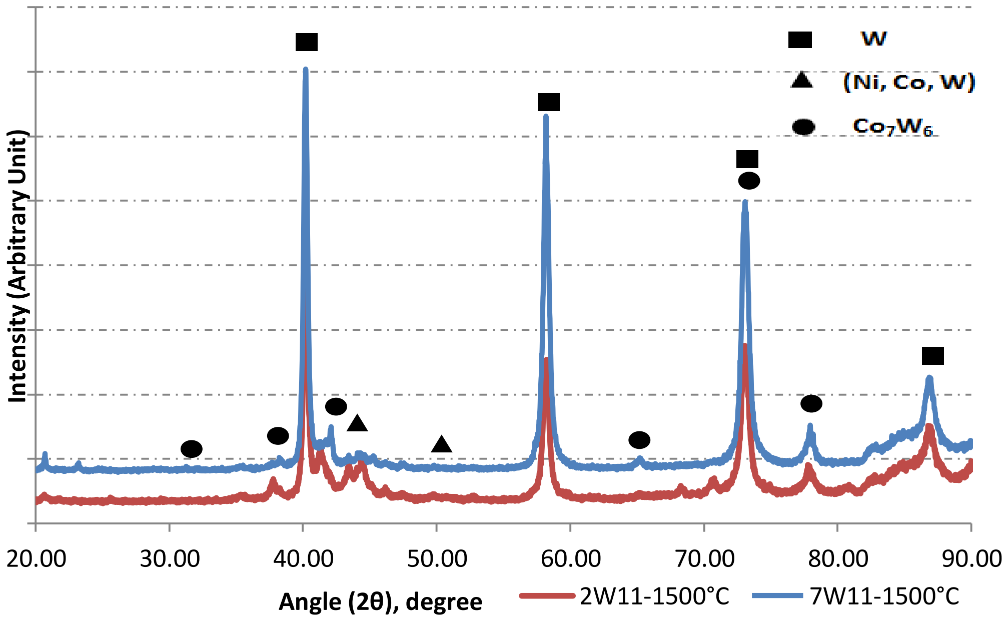

Figure 51 X-ray diffraction patterns of 2W11 and 7W11 alloys sintered at 1500°C

Table 12 Crystal Structure and Lattice Parameter Data for the Investigated W-Ni-Co Alloys

Materials	**Lattice Parameter (Angstroms)**		**Crystal Structure**
	Literature	**Calculated**	
W	3.16	3.16	BCC
Ni	3.52	-	FCC
Co	a: 2.50 c: 4.06	-	HCP
Co_7W_6 [33]	a: from 4.72 to 4.75 c: from 25.48 to 25.67	-	Tetrahedrally Closed Packed
Ni-Co-W binder phase	-	3.60	FCC

The average W grain size (AGS) of the investigated alloys was measured with Planimetric method as described in detail in Chapter 3. AGS measurements were applied to all alloys except those having Ni/Co ratio 1/4 and those sintered at 1450°C. The results of the AGS measurements are given in a compact form in Table 13 and all measurements are given in Appendix D. It can be argued that the AGS measurement method applied in the study, namely the Planimetric method, might not be suitable for WHA composite structures. This is because the Planimetric method is best suited for single-phase materials with a homogeneous grain structure, whereas the investigated WHA microstructures contain the combination of small and large W grains together with a binder matrix phase. However, Planimetric method was found to be used in this type alloy system in the literature [34] [35], and hence it is also applied in the present study as a simple means to determine the AGS.

Various properties of the W-Ni-Co WHAs, for example the mechanical properties, might also be affected by the W grain size distribution. This distribution, on the other hand, might be dependent on various composition and sintering variables. However, the nature of the W grain size distribution is not reflected in the AGS parameter. For example, for two grain size distributions with widely different distribution characteristics, the AGS parameter might yield a very similar value.

Table 13 Average W Grain Size (AGS) of the Investigated W-Ni-Co Alloys

Specimen Code	Sintering Temperature (°C)					
	1450	1475	1500	1525	1550	1600
	AGS (μm)					
0W14	-	-	-	-	-	-
0W11	-	24.8∓0.3	25.3∓0.6	31.7∓0.1	29.3∓0.4	35.7∓0.5
0W31	-	28.6∓1.1	29.6∓0.8	29.6∓0.6	31.3∓0.7	33.8∓0.4
0W41	-	24.0∓0.7	26.7∓0.6	29.2∓0.7	29.8∓0.1	32.2∓0.3
0W61	-	29.8∓0.4	28.1∓0.3	28.4∓0.4	30.6∓0.4	32.6∓0.1
2W11	-	23.6∓0.5	28.9∓0.4	27.9∓0.2	29.8∓0.1	35.6∓0.8
2W41	-	28.6∓0.2	31∓1.1	30.7∓0.2	30.8∓0.2	32.8∓0.9
5W14	-	-	-	-	-	-
5W11	-	23.3∓0.6	27.6∓0.1	30.7∓0.4	34∓0.6	34.3∓0.2
5W31	-	28.3∓0.5	27.8∓0.3	28.4∓0.3	31.5∓0.2	35.3∓0.7
5W41	-	24.6∓0.6	27.4∓0.4	30.2∓0.5	31.3∓0.4	35.7∓0.3
5W61	-	27.4∓0.6	28.1∓0.4	30.1∓0.4	31.5∓0.3	38.1∓0.2
7W11	-	23.6+0.6	29.8+0.5	30.6∓0.8	30.3∓0.5	39.5∓1.8
7W41	-	29.2∓0.4	31.2∓0.1	32∓0.6	31.3∓0.4	39.0∓0.8

When the AGS results given in Table 13 is investigated in detail, it can be seen that there is no straightforward correlation between AGS and Ni/Co ratio for the Ni-rich and Ni/Co ratio 1/1 alloys. However, detailed microstructural examination studies have implied that the W grain size distribution might vary with Ni/Co ratio. For

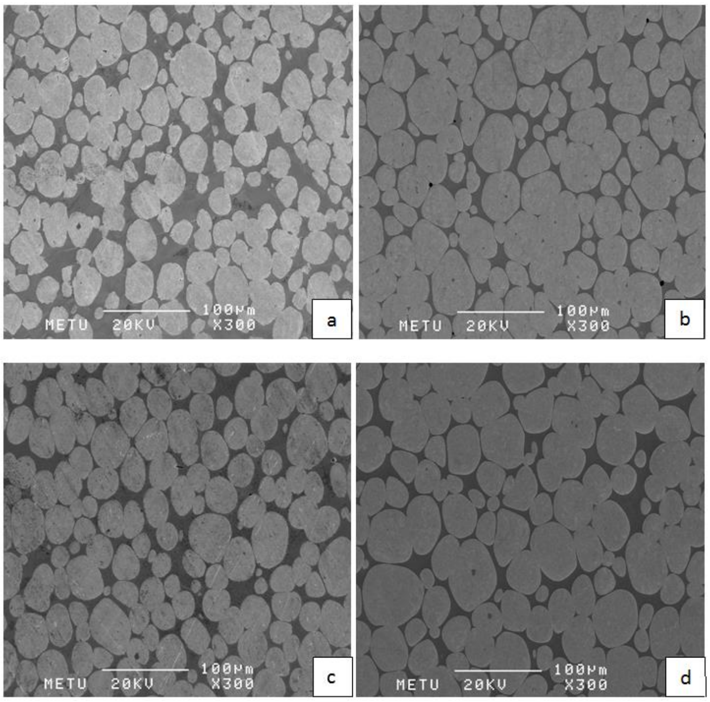

Figure 52 The variation of W grain size distribution with Ni/Co ratio: Microstructures of; a) 0W11, b) 0W31, c) 0W41 and d) 0W61 alloys sintered at 1500°C, SEM secondary electron images, 300x

illustrative purposes, the microstructures of 90% W Ni-rich and Ni/Co ratio 1/1 alloys are shown in Figure 52. As seen in Figure 52, the co-existence of very small and very large W grains in the microstructures imply that the W grain size distribution might not be uniform for these alloys. In the microstructures given in Figure 52, small W grains are about 5-15 μm and the bigger ones are up to 60 μm in size. In addition, the appearance of the microstructures imply that increasing the Ni/Co ratio in the investigated alloys causes a decrease in the number of small grains and make large W grains larger, for a given sintering temperature and alloy W content.

To determine whether the W grain size distribution has a dependence on alloy composition or not, the W grain size distribution of selected Ni-rich W-Ni-Co alloys

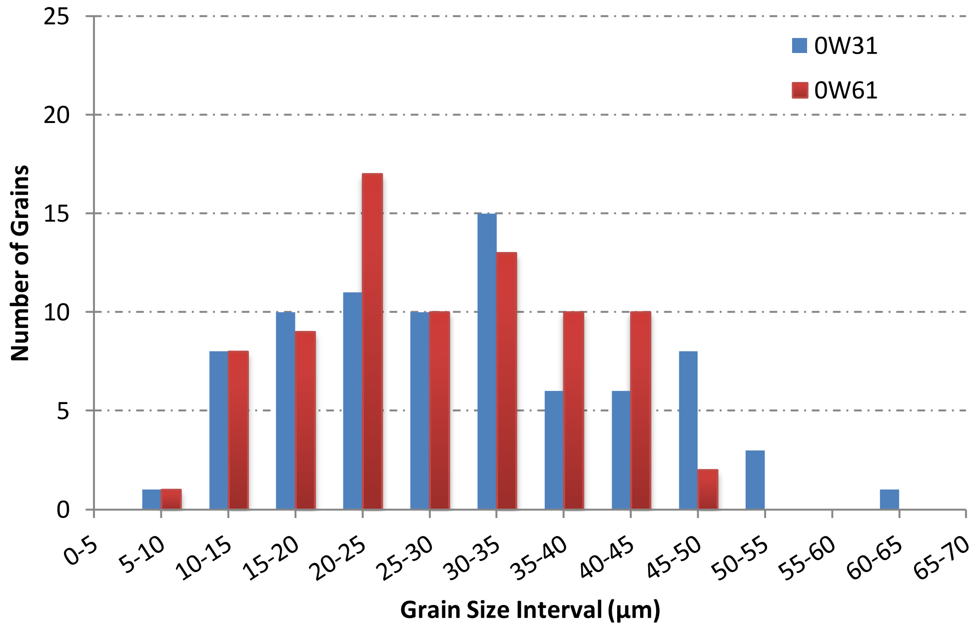

Figure 53 Grain size distribution of 0W31 and 0W61 alloys sintered at 1500°C

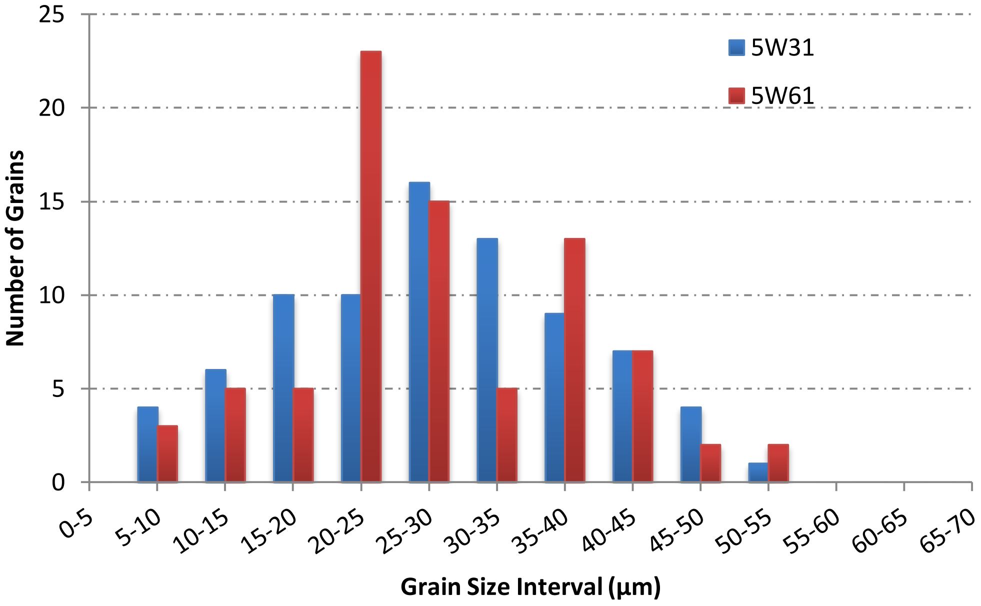

Figure 54 Grain size distribution of 5W31 and 5W61 alloys sintered at 1500°C

were tried to be determined tentatively. For this purpose, W grain size distributions were measured on 80 randomly selected grains of 0W31, 0W61, 5W31 and 5W61 alloys sintered at 1500°C, as described in Chapter 3, Section 3.2.1.2. The results of these tentative measurements are given in Figure 53 and Figure 54. In Figure 53 and Figure 54, it is seen that the W grain size distribution might be multi-modal for some investigated alloys, and might vary both with Ni/Co ratio and alloy W content. However, to determine the exact relationship between the W grain size distribution and composition and sintering variables, further detailed study is required. Such kind of an investigation may be suggested as a subject for future work on W-Ni-Co alloys.

Compiled from the AGS results given in Table 13, the variation of AGS with sintering temperature and Ni/Co ratio are given for 90 and 95% W Ni-rich and Ni/Co ratio 1/1 alloys in Figure 55 and Figure 56, respectively. For providing visual comparison for the data, the representative microstructures of Ni-rich 0W61 and 0W31 alloys sintered at different temperatures are given in Figures 57 and 58. The

AGS results given in Table 13 and Figures 55 and 56 suggest that there is no straightforward correlation between AGS and Ni/Co ratio for the investigated alloys. On the other hand, as can be seen from Figures 55 to 58, the AGS of the investigated alloys was found to increase with increasing sintering temperature, especially when sintered at and above 1525°C, for both 90 and 95% W. This temperature dependence of AGS is in fact expected, because the sintering process of the investigated alloys was mainly diffusion controlled. Owing to this diffusion control, the investigated alloys sintered at higher temperatures have had higher sintering and coarsening rates when compared to those sintered at lower temperatures. The grain growth mechanism is thought as Ostwald ripening due to observation of larger grains at relatively high temperatures. Because of this fact, these alloys have coarsened more during the sintering period when compared to the others, and therefore have shown higher AGS values.

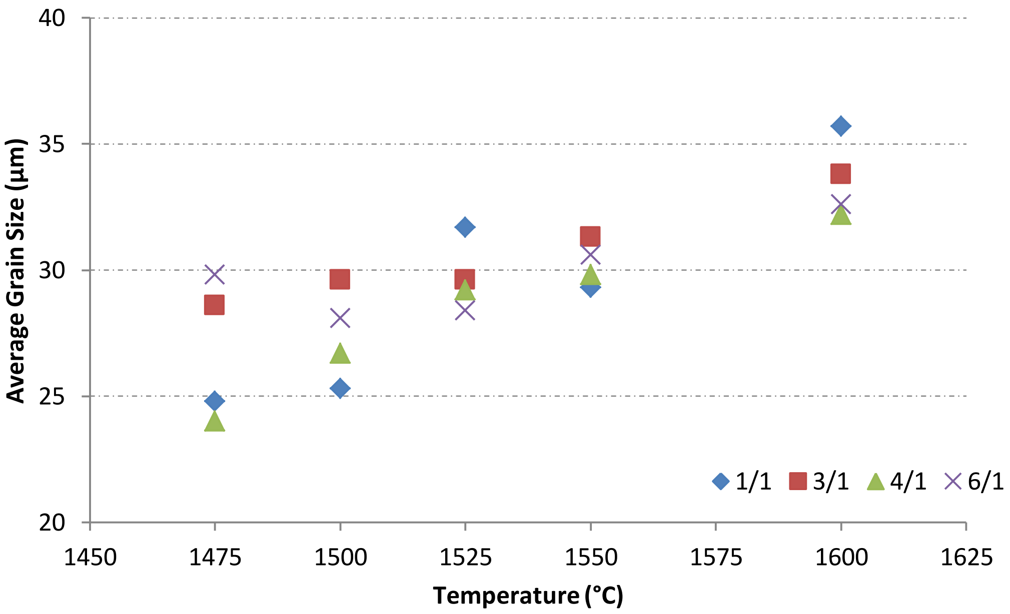

Figure 55 The variation of average grain size with sintering temperature and Ni/Co ratio for 90% W Ni-rich and Ni/Co ratio 1/1 alloys

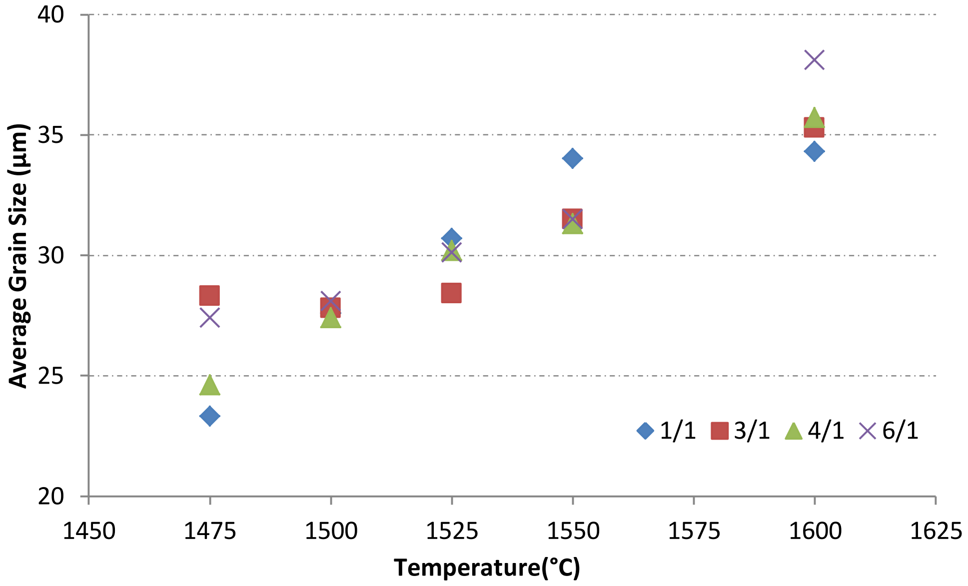

Figure 56 The variation of average grain size with sintering temperature and Ni/Co ratio for 95% W Ni-rich and Ni/Co ratio 1/1 alloys

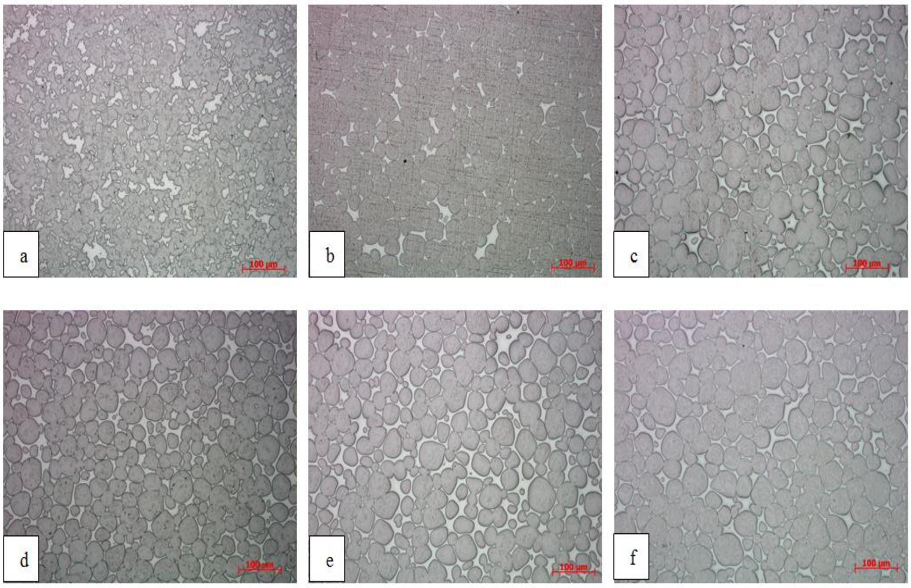

Figure 57 Optical microstructure images of 0W61 alloy, sintered at: a) 1450°C, b) 1475°C, c) 1500°C, d) 1525°C, e) 1550°C, f) 1600°C, 200x

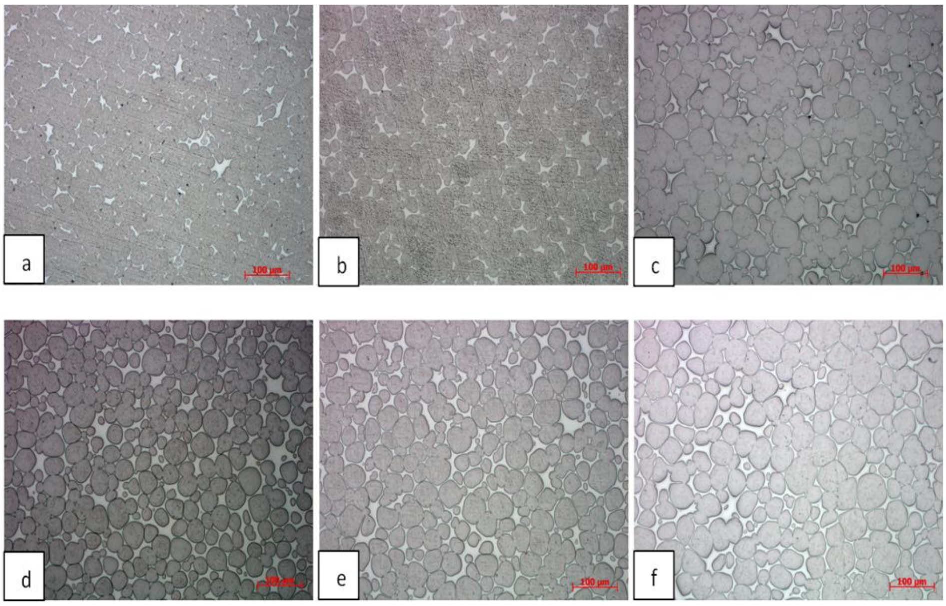

Figure 58 Optical microstructure images of 0W31 alloy sintered at: a) 1450°C, b) 1475°C, c) 1500°C, d) 1525°C, e) 1550°C, f) 1600°C, 200x

Investigation of the data given in Table 13 suggests that there is no evident relationship between AGS and alloy W content for the investigated alloys for low sintering temperatures. However, for the Ni-rich alloys, the AGS was seen to increase with increasing alloy W content for sintering temperatures above 1525°C. To illustrate this dependence, the variation of AGS with alloy W content is given in Figure 59 for Ni/Co ratio 4/1 alloys sintered at 1550°C and 1600°C. For providing visual evidence for this fact, the microstructure images of 0W41 and 7W41 alloys sintered at 1600°C are shown in Figure 60. As can be seen in Figures 59 and 60, the AGS of Ni/Co ratio 4/1 alloys increases with increasing W content for the given sintering temperatures. This general trend almost entirely holds for the other Ni-rich alloys, and partly holds for the Ni/Co ratio 1/1 alloys.

The dependence of the AGS on alloy W content might be explained as follows: In the alloys with higher W content, the amount of W particles will be higher per unit volume. In addition, the phase diagram characteristics of the W-Ni-Co system dictates that the total amount of the binder matrix phase will be lower in these alloys when compared to the alloys having lower W content, at a given sintering temperature. As can be seen from Figures 41 and 42, this latter fact has been confirmed experimentally by the % binder phase area determinations applied in the study. Owing to these two facts, the diffusional path among the W particles will be smaller and all diffusional processes within the binder matrix phase will take place over shorter distances in the alloys with higher W content. As a result, the densification and coarsening rate in these alloys might be higher, and therefore these alloys might show larger AGS than the alloys having lower W content. This compositional dependence of AGS on the W content, however, is not as strong as the temperature dependence. This might be the reason why this compositional dependence becomes pronounced and observable only above certain sintering temperatures.

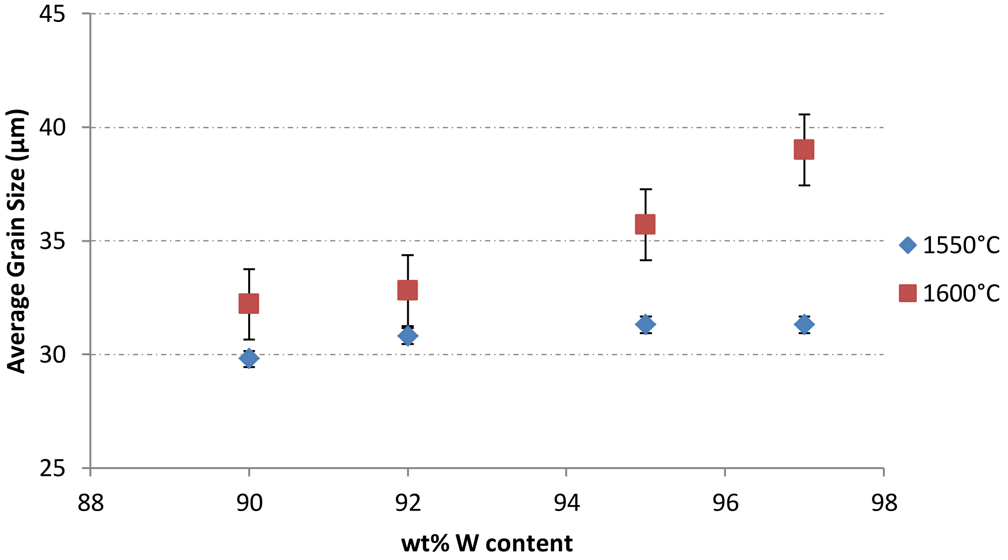

Figure 59 Average grain size variation with W content for Ni/Co ratio 4/1 alloys sintered at 1550 and 1600°C

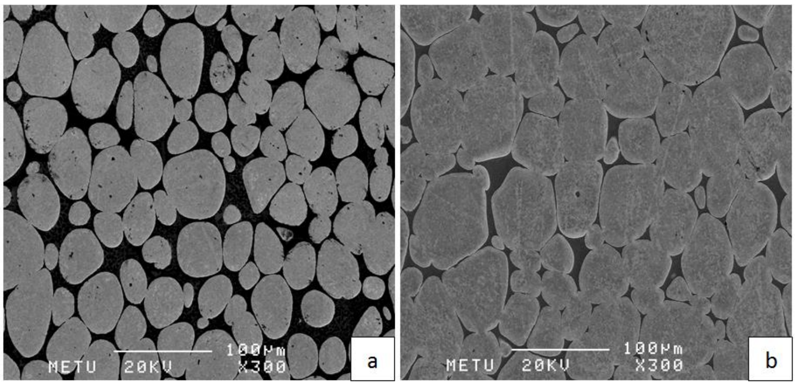

Figure 60 Microstructure images showing the average grain size variation with increasing W content for: a) 0W41, b) 7W41 Ni-rich alloys sintered at 1600°C, SEM secondary electron images, 300x,

Detailed microstructural examinations have shown that Co-rich alloys showed a tremendously increasing AGS while the sintering temperature was changing from 1550 to 1600°C. This observation is shown in Figure 61. As mentioned before, the results of the study suggest that these Co-rich alloys were sintered in the solid state. It is suggested that the extreme increase of AGS in these Co-rich alloys might have resulted in due to enhanced coarsening at higher temperatures.

For the evaluation of the mechanical properties, hardness tests were applied on selected W-Ni-Co alloys with Vickers hardness scale by applying 10 kg load. The W-Ni-Co alloys selected for hardness tests were those sintered at and above 1500°C. Measurement results are given in Appendix E. The hardness variation with sintering temperature and W content for Ni/Co ratio 1/1 and 4/1 alloys is given in Figure 62. For particular illustrative purposes, the variation of hardness with W content and sintering temperature for Ni/Co ratio 1/1 alloys is depicted in Figure 63. Finally, the hardness variation with Ni/Co ratio and W content for 90 and 95% W alloys is shown in Figure 64.

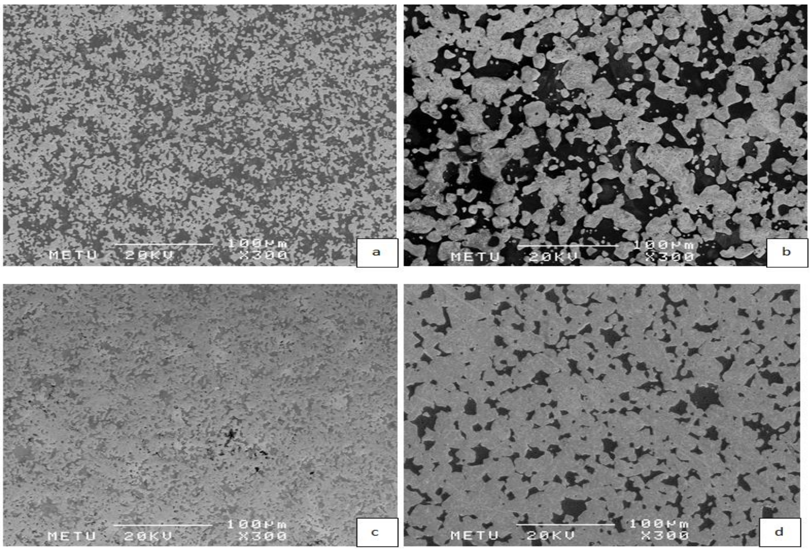

Figure 61 Microstructures of 90 and 95% W Co-rich alloys showing the tremendous increase in the average grain size when sintering temperature has been increased from 1550 to 1600°C: a) 0W14 sintered at 1550°C, b) 0W14 sintered at 1600°C, c) 5W14 sintered at 1550°C, d) 5W14 sintered at 1600°C, SEM secondary electron images, 300x

Before going on further, it should be mentioned that hardness tests were also applied to Co-rich Ni/Co ratio 1/4 alloys sintered at 1500°C. Owing to several experimental limitations, the hardness of these alloys was not determined for the other sintering temperatures. For these alloys, namely alloys 0W14 and 5W14, hardness tests have shown that both 0W14 and 5W14 alloys have lower hardness when compared to all other alloys sintered at 1500°C. The reason for this lower hardness is most probably related to the limited density of these alloys. As also given in Table 9, at 1500°C sintering temperature, densification is limited to around 82% and 86% RD for 0W14 and 5W14 alloys, respectively. Due to presence of the pores, these alloys are soften than fully dense alloys.

When the hardness results given in Figures 62 to 64 are evaluated altogether, the following observations can be made: Firstly, as can be seen in Figures 62 and 64, the hardnesses of the Ni-rich alloys were all lower than those of Ni/Co ratio 1/1 alloys, and were only marginally affected with alloy W content and sintering temperature variations. These figures also show that the hardness of the Ni/Co ratio 1/1 alloys was significantly higher when compared to all other Ni-rich alloys, for all sintering temperatures and alloy W contents. Figures 62 and 63 show that the hardness of these Ni/Co ratio 1/1 alloys was only marginally affected with sintering temperature, similar to the Ni-rich alloys. These alloys, however, have had a strong dependence of hardness on the alloy W content, as can be seen particularly in Figures 62 and 63. In this respect, the hardness of these alloys was found to decrease with increasing alloy W content, except occasional cases. As mentioned before, the main difference between the Ni-rich and Ni/Co ratio 1/1 alloys in terms of their microstructure is that the former alloys consist of a single phase binder matrix, whereas the binder matrix

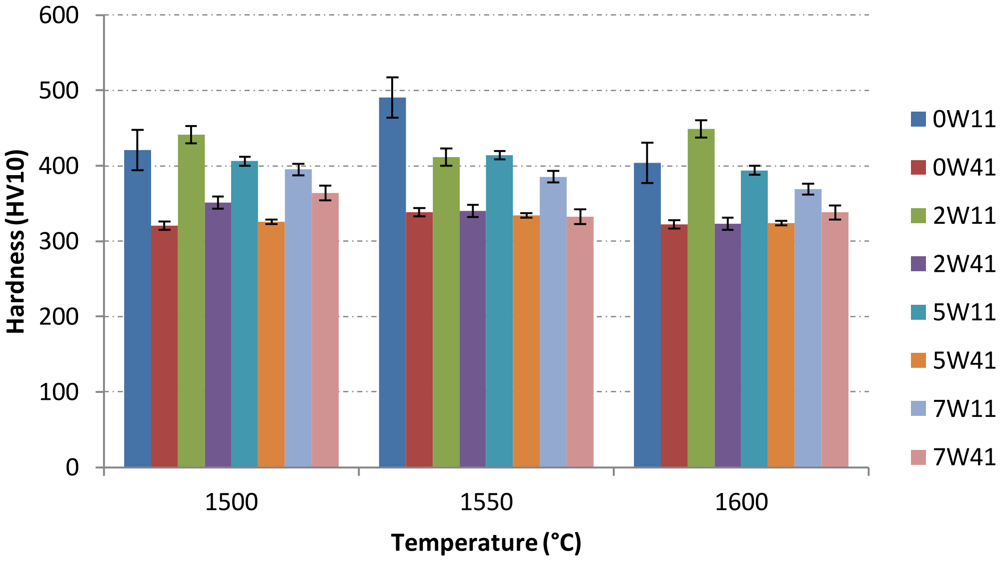

Figure 62 Hardness variation with sintering temperature and W content for Ni/Co ratio 1/1 and 4/1 alloys

of the latter alloys consist of two phases. The hardness results shown in Figures 62 to 64 strongly suggest that the enhanced hardness of the Ni/Co ratio 1/1 alloys is directly related to the existence of a two-phase binder matrix in these alloys. That is, the existence a two-phase binder matrix seems to be more beneficial for hardness enhancement in W-Ni-Co alloys, when compared to a single phase matrix. A strong evidence for this suggestion comes from the fact that the hardness of Ni/Co ratio 1/1 alloys decreases significantly and approaches that of Ni-rich alloys with increasing alloy W content. It is known that the total amount of the two-phase binder matrix in these alloys also decreases with increasing alloy W content, which can be seen in Figure 43 and Figure 44. This direct relationship between the hardness and the two-phase binder amount gives a strong indication that the hardness enhancement in the Ni/Co ratio 1/1 alloys is mainly determined by the two-phase binder matrix.

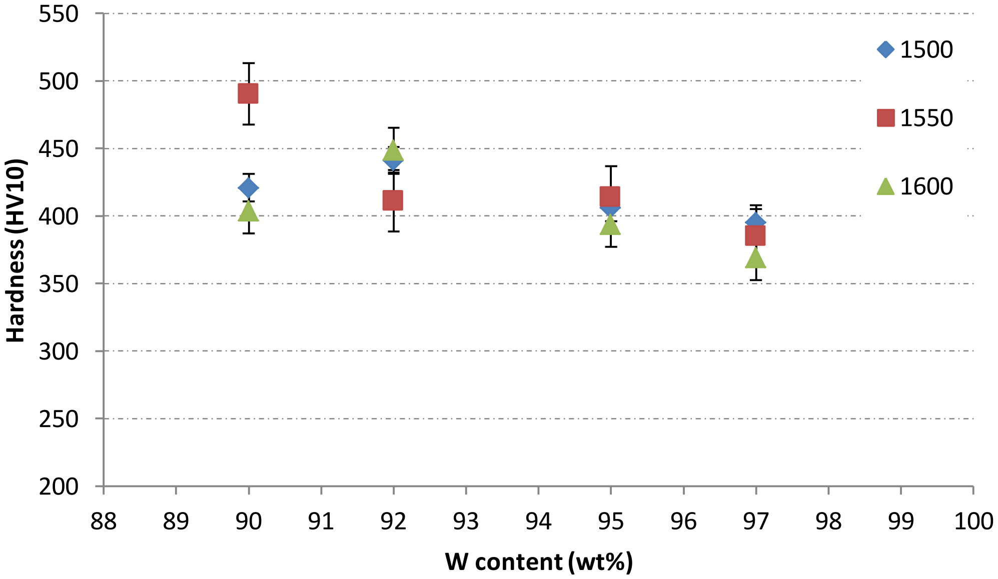

Figure 63 Hardness variation with W content for Ni/Co ratio 1/1 alloys sintered at 1500, 1550 and 1600°C

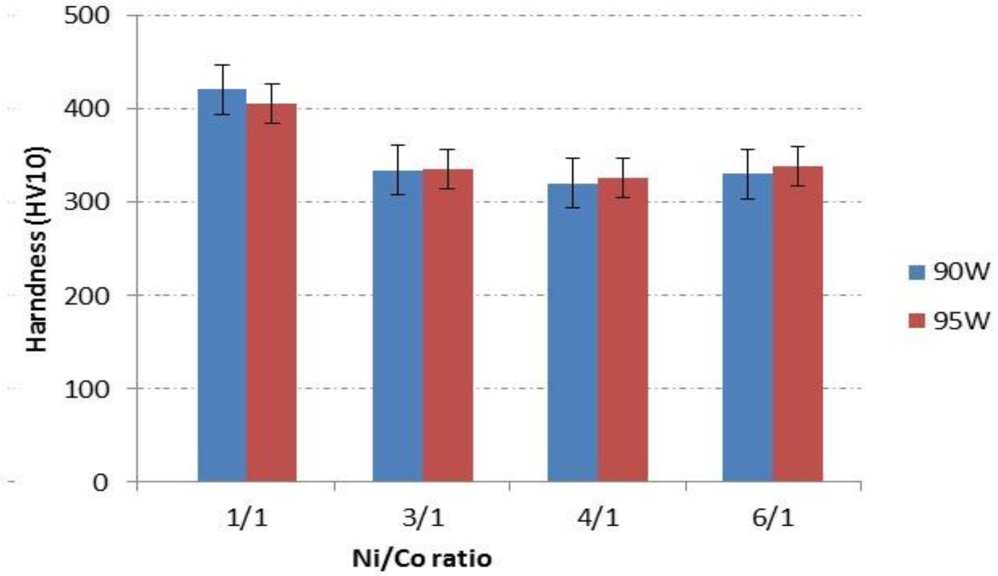

Figure 64 Hardness variation with Ni/Co ratio and W content for 90 and 95 % W alloys sintered at 1500°C

Finally, in order to find a correlation between measured results and compositional and sintering variables, a multiple regression analysis was applied on investigated Ni-rich W-Ni-Co alloys with the aid of IBM SPSS™ statistics software. The analysis was applied among AGS, % W in binder phase, % binder matrix area, % Ni composition, sintering temperature and % relative density. By the aid of this software, data were converted to non-dimensional values in order to get rid of the different units. Normalized values for 90 wt% alloys are given in Appendix F. The aim of running multiple regression analysis is that to find a correlation between AGS and other variables for 90 and 95 wt% W Ni-rich alloys and the relative importance of each parameter. Summarized values of this analysis for 90 wt% W Ni-rich alloys is given in Table 14. It is emphasized that separate interaction between each variables is neglected for easy calculation of multiple regression analysis.

Table 14 Summarized non-dimensional data for 90 wt% alloys

Variable (non-dimensional)	**Coefficient**	**t statistics**	**P value (for t statistics)**
Composition (Ni Content)	-0.177	-1.014	0.335
Temperature	0.883	4.659	0.001
Relative Density	0.300	1.509	0.162
W in Binder Phase	-0.250	-1.105	0.295
Binder Matrix Area	0.013	0.075	0.941
Summarized Regression Statistics			
R^2=0.747	F value = 6.064	P value (for F value)=0.008	

From the multiple regression analysis, an equation for average grain size (AGS) can be written for 90% W alloys as in Equation 15;

$$AGS = -0.177(X_1) + 0.883(X_2) + 0.300(X_3) - 0.250(X_4) + 0.013(X_5) \qquad (15)$$

It is seen that R^2 is equal to 0.747 for statistical model 90 wt% Ni-rich W-Ni-Co alloys. This means that variables in the regression model explains 74.7% of average grain size values. Also, P for F value is used to explain the significancy of the statistical model. In this analysis, this model is significant on 95% confidence level that P (for F value) is equal to 0.008 and 0.008<α=0.05 where ∝ is significance level. Moreover, investigation of significance of each variable, it is found that only temperature has significance on AGS because P value (for t statistics) is 0.001<α=0.05. Other variables cannot affect the AGS as temperature does.

Similarly, multiple regression analysis is used to find a correlation between AGS and other variables for 95 wt% W Ni-rich alloys and the relative importance of each parameters. Summarized values of this analysis for 95 wt% W Ni-rich alloys is given in Table 15.

Table 15 Summarized non-dimensional data for 95 wt% alloys

Variable (non-dimensional)	**Coefficient**	**t statistics**	**P value (for t statistics)**
Composition (Ni Content)	-0.101	1.372	0.200
Temperature	1.068	9.767	0.000
Relative Density	0.204	1.958	0.079
W in Binder Phase	-0.150	-1.309	0.220
Binder Matrix Area	-0.232	-2.358	0.040
Summarized Regression Statistics			
R^2=0.973	F value 35.019	P value (for F value)=0.000	

Similarly, for 95% W alloys, an equation for average grain size (AGS) can be written as in Equation 16;

$$AGS = 0.101(X_1) + 1.068(X_2) + 0.204(X_3) - 0.150(X_4) - 0.232(X_5) \qquad (16)$$

where normalized non-dimensional values are;

- X_1 : Composition (Ni content)
- X_2 : Temperature

- X_3 : Relative Density
- X_4 : W in binder phase
- X_5 : Binder matrix area

It is seen that R^2 is equal to 0.973 for statistical model 95 wt% Ni-rich W-Ni-Co alloys. This R^2 is much higher than for that 90 wt % alloys. This means that variables in the regression model explain 97.3 % of average grain size values. In addition, P for F value is used to explain the significancy of the statistical model. In this analysis, this model is significant on 95% confidence level that P (for F value) is equal to 0.000 and $0.000<\alpha=0.05$ where $\propto$ is significance level. Besides, investigation of significance of each variable, it is found that temperature and binder matrix area have significance on AGS because P values (for t statistics) are $0.000<\alpha=0.05$, $0.040<\alpha=0.05$ respectively. Other variables cannot affect the AGS as temperature and binder matrix area does.

CHAPTER 5

CONCLUSIONS

In this work, several selected alloys were studied on the W-rich side of the W-Ni-Co alloy system. The effects of sintering temperature and composition on the microstructural characteristics were investigated for these alloys. The major conclusions that can be drawn from the study are as follows:

1. Increasing sintering temperature has increased the relative densities to almost full density for all alloy compositions studied, except Co-rich alloys. Co-rich alloys have reached full density only when sintered at 1600°C. In addition, these Co-rich alloys could not be densified with LPS due to the lack of the liquid phase.

2. For the Ni-rich alloys with Ni/Co ratio changing between 3/1 and 6/1, microstructural examination has revealed that the alloys investigated have a typical microstructure consisting of rounded, nearly pure W grains and a W-Ni-Co binder matrix phase. On the other hand, a microstructure consisting of nearly pure W grains and a two-phase binder matrix has been observed in all of the alloys with Ni/Co ratio 1/1.

3. The binder matrix phase in the Ni-rich alloys was found to dissolve relatively large amounts of W homogeneously. The amount of W dissolved in this phase has reached up to 43 wt %.

4. For the Ni-rich alloys with Ni/Co ratio changing between 3/1, 4/1 and 6/1, the areal percentage of the binder matrix phase was determined to increase with increasing sintering temperature, and to decrease with increasing alloy W content. For these alloys, decrease in the percent binder phase area observed above a certain sintering temperature (nearly 1525°C) is not considered to

represent the natural behavior. This misleading behavior is attributed to the physical collapse of the alloy samples under gravity during LPS, which leads to the agglomeration of W grains and exuding of the liquid phase owing to the large density differences.

5. For the Ni-rich alloys with Ni/Co ratio ranging between 3/1 and 6/1, and for sintering temperatures above 1525 °C, the average W grain size (AGS) was found to increase with increasing sintering temperature and alloy W content. This trend also generally holds for the alloys with Ni/Co ratio 1/1 and 1/4. Tentative analysis has implied that the grain size distribution might be multi-modal for some of the Ni-rich alloys.

6. The hardness of the alloys with Ni/Co ratio 1/1 was found to be greater than all of the remaining alloys. This beneficial behavior was attributed to the presence of a two-phase binder matrix in these alloys.

7. The hardness of the alloys with Ni/Co ratio 1/1 was observed to decrease with increasing alloy W content. In these alloys, the relative amount of the two-phase binder matrix was also found to decrease with increasing W content. These findings support that the two-phase binder matrix in these alloys resulted in high hardness after liquid phase sintering.

8. The results of the study revealed that it is possible to tailor the microstructural characteristics of W-Ni-Co alloys by changing the composition and sintering parameters. It is suggested that novel W-Ni-Co alloys with enhanced properties can be designed and developed for industrial applications through control of these variables.

REFERENCES

[1] Wu; YunXin; German, Randall M.; Marx, Brain; Suri, Pavan; Bollina, Ravi;, "Comparison of Densification and Distortion Behaviors of W-Ni-Cu and W-Ni-Fe Heavy Alloys in Liquid Phase Sintering," no. 10, pp. 2271-2281, 2003.

[2] German, Randall M.; Suri, Pavan; Park, Seong Jin;, "Review: Liquid Pahase Sintering," *Journal of Material Science,* pp. 1-39, 2009.

[3] K. Chattopadhyay, "Microstructural Characterization of Sintered W-Ni-Cu Alloys," April 2003.

[4] H. I. Sanderow, "Powder Metallurgy Methods and Design," in *ASM Metals Handbook, Vol. 7, Powder Metallurgy,* ASM, 1998, pp. 10-23.

[5] R. M. German, Powder Metallurgy Science, New Jersey: Metal Powder Industries Federation, 1984.

[6] W. D. Jones., Fundamental Principles of Powder Metallurgy, London: Edward Arnold Publishers, 1960, p. 600.

[7] B. L. Fergusson and S. G. Caldwell, "ASM Handbook Vol.7," in *Powder Metal Technologies and Applications*, ASM International, 1998, pp. 2297-2310.

[8] R. M. German, Sintering Theory and Practice, New York: John Wiley& Sons, 1996.

[9] R. M. German, Powder Metallurgy Science, New Jersey: Metal Powder Industries Federation, 1984.

[10] Shimosaka, A.; Ueda, Y.; Shirakawa, Y.; Hidaka, J.;, "Sintering Mechanism of Two Spheres Forming a Homogeneous Solid Solubilitiy Neck," *KONA Powder and Particle Journal*, vol. 21, pp. 219-233, 2003.

[11] "Department of Materials Science and Engineering of Michigan University," [Online]. Available: www.mse.mtu.edu/...html/Sinter%201Y.ppt. [Accessed 27 October 2013].

[12] R. Coble, "Sintering Crystalline Solids. I. Intermediate and Final State Diffusion Model," no. 32, pp. 787-792, 1961.

[13] J. Luo, "Liquid-like interface complexion: From activated sintering to grain boundary diagrams," no. 12, 2008.

[14] A. L. Prill, H. W. Hayden and J. H. Brophy, "The Role of Phase Relationships in the Activated Sintering of Tungsten," vol. 230, 1964.

[15] Bordia, Rajendra K.; Camacho-Montes, Hector;, "Densification," in *Sintering: Fundamentals and Practice*, pp. 3-37.

[16] Huppmann, W. J.; Rieger, H.;, "Liquid Phase Sintering of Model System W-Ni," *International Journal of Powder Technology*, vol. 13, pp. 243-247, 1977.

[17] R. M. German, Liquid Phase Sintering, NY: Plenum Press, 1985.

[18] Hwang, K. S.; German, R. M.; Lenel, F. V.;, "Capillary forces between spheres during agglomeration and liquid phase sintering," *Metallurgical Transactions A*, vol. 18(1), pp. 11-17, 1987.

[19] W. J. Huppman, H. Rieger, W. A. Kaysser, V. Smolej and S. Pejovnik, "The Elementary Mechanism of Liquid Phase Sintering I. Rearrangement," *Zeitschrift*

für Metallkunde, vol. 70, pp. 707-713, 1979.

[20] W. D. Kingery, "Densification During Sintering in the Presence of a Liquid Phase I Theory," *Journal of Applied Physics,* vol. 30, pp. 301-306, 1959.

[21] Gessinger, G. H.; Fishmeister, H. F.; Lukas, H. L.;, "A Model for Second Stage Liquid Phase Sintering with Partially Wetting Liquid," *Acta Metallurgica,* vol. 21, pp. 715-724, 1973.

[22] German, R. M.; Bose, Animesh; Mani, S. S.;, "Sintering Time and Atmosphere Influences on Microstructure and Mechanical Properties of Tungsten Heavy Alloys," *Metallurgical Transactions A,* vol. 23(1), pp. 211-219, 1992.

[23] German, R. M.; Churn, K. S.;, "Sintering Atmosphere Effects on Ductility of W-Ni-Fe Heavy Metals," *Metallurgical and Materials Transactions A,* vol. 15A, pp. 747-754, 1984.

[24] Mondal, Avijit; Upadhyaya, Anish; Agrawal, Dinesh;, "Effect of heating mode and sintering temperature on the consoldation of 90W-7Ni-3Fe alloys," *Journal of Alloys and Compounds,* no. 509, pp. 301-310, 2011.

[25] A. Upadhyaya, "Processing Strategy for Consolidating Tungsten Based Alloys for Ordnance Applications," *Materials Chemistry and Physics,* no. 67, 2001.

[26] Bose, A.; German, R. M.;, "Sintering Atmosphere Effects on Tensile Properties of Heavy Alloys," *Metallurgical and Materials Transactions,* no. A.19, pp. 2467-2476, 1988.

[27] Moon, I. H.; Kim, J. H.; Suk, M. J.; Lee, K. M.; Lee, J. K.;, "Observation of W Particle Growth in a W Powder Compact During Sintering in a Non-Reducing Atmosphere," *International Journal of Refractroy Metals and Hard Materials,*

no. 11, pp. 309-315, 1992.

[28] S. G. Caldwell, "Variation of Ni/Fe Ratio in W-Ni-Fe Alloys: A Current Perspective," in *Proceedings of the First International Conference on Tungsten and Tungsten Alloys*, 1992.

[29] Kiran, U. Ravi; Rao, A. Sambasiva; Sankaranarayana, M.; Nandy, T. K.;, "Swaging and heat treatment studies on sintered 90W-6Ni-2Fe-2Co heavy alloys," *International Journal of Refractory Metals and Hard Materials,* pp. 1-9, 2012.

[30] E. W. Kennedy, "Influence of Microstructure on Fracture Characteristics and Tensile Properties of Two Tungsten Heavy Alloys," Virginia, 1994.

[31] B. Katavic, M. Nikacevic and Z. Odanovic, "Effect of Cold Swaging and Heat Treatment on Properties of the P/M 91W-6Ni-3Co Heavy Alloy," no. 40, pp. 319-331, 2008.

[32] K. P. Gupta, "The Co-Ni-W (Cobalt-Nickel- Tungsten) System," vol. 21, no. 4, 2000.

[33] Carvalho, P. A.; Haarsma, H. S.D.; Kooi, B. J.; Bronsveld, P. M.; De Hosson, J.TH. M.;, "HRTEM Studuy of Co7W6 and Its Typical Defect Structure," *Acta Materialia,* vol. 48, pp. 2703-2712, 2000.

[34] N. K. Çalışkan, "Processing and Characterization of High Density Tungsten-Nickel-Iron Alloys," 2013.

[35] Jing-lian, F.; Tao, L.; Hui-chao, C.;, "Preparation of fine grain tungsten heavy alloy with high properties by mechanical alloying and yttrium oxide addition," *Journal of Materials Processing Technology,* no. 208, pp. 463-469, 2008.

APPENDIX A

SPECIMEN DENSITY MEASUREMENTS

Table A.1 Green Densities of Compressed Specimens

Alloy Code	**Green Densities (g/cm3)**	
	Specimens	
	1	**2**
0W14	10.6	10.6
0W11	10.6	10.5
0W31	10.6	10.6
0W41	10.6	10.7
0W61	10.6	10.6
2W11	10.7	10.7
2W41	10.9	10.8
5W14	11,1	11.2
5W11	11.1	11.1
5W31	11.0	11.1
5W41	11.2	11.1
5W61	11.1	11.0
7W11	11.5	11.5
7W41	11.6	11.5

Table A.2 Sintered Densities of Specimens

Alloy Code	**Sintered Densities (g/cm3)**											
	Specimens											
	Temperature (°C)											
	1450		**1475**		**1500**		**1525**		**1550**		**1600**	
	1	**2**	**1**	**2**	**1**	**2**	**1**	**2**	**1**	**2**	**1**	**2**
0W14	13.5	13.6	14.2	14.2	14.2	14.2	15.1	15.1	16.0	16.0	17.3	17.3
0W11	17.1	17.1	17.3	17.3	17.3	17.3	17.1	17.1	17.3	17.3	17.2	17.2
0W31	17.1	17.1	17.2	17.2	17.2	17.2	17.3	17.3	17.3	17.3	17.3	17.2
0W41	17.0	17.0	17.2	17.2	16.8	16.8	17.0	17.0	17.2	17.2	17.3	17.3
0W61	17.0	17.1	17.3	17.3	17.1	17.2	17.3	17.3	17.3	17.3	17.1	17.1
2W11	17.3	17.3	17.6	17.6	17.5	17.5	17.5	17.6	17.6	17.6	17.7	17.7
2W41	17.6	17.5	17.5	17.5	17.3	17.3	17.6	17.6	17.6	17.6	17.6	17.6
5W14	14.8	14.8	15.1	15.1	15.6	15.7	16.3	16.3	17.0	17.0	18.3	18.3
5W11	17.5	17.5	18.1	18.2	18.3	18.3	18.2	18.2	18.2	18.2	18.3	18.3
5W31	17.7	17.7	18.2	18.2	18.1	18.1	18.3	18.3	18.2	18.2	18.2	18.2
5W41	17.2	17.2	17.7	17.7	18.3	18.3	18.1	18.1	18.2	18.2	18.2	18.3
5W61	17.4	17.3	18.2	18.2	18.2	18.2	18.3	18.3	18.2	18.2	18.0	18.1
7W11	17.9	17.9	18.7	18.6	18.6	18.6	18.7	18.7	18.6	18.6	18.7	18.7
7W41	18.6	18.6	18.6	18.6	18.6	18.5	18.6	18.6	18.5	18.5	18.6	18.7

APPENDIX B

OPTICAL MICROSTRUCTURE IMAGES

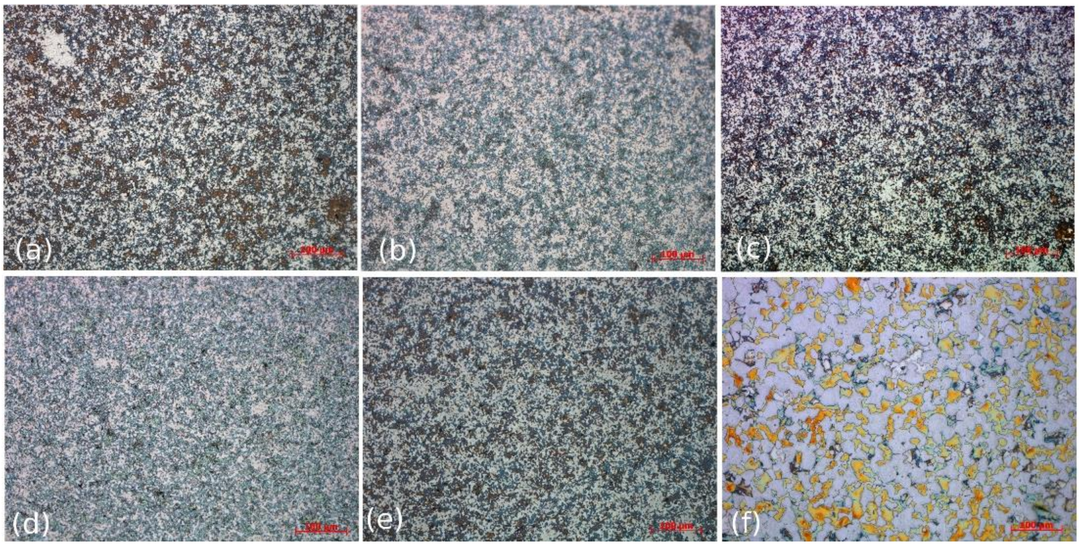

Figure B.1 Optical microstructure images of 0W14 alloy sintered at: a) 1450°C, b) 1475°C, c) 1500°C, d) 1525°C, e) 1550°C, f) 1600°C, 200x

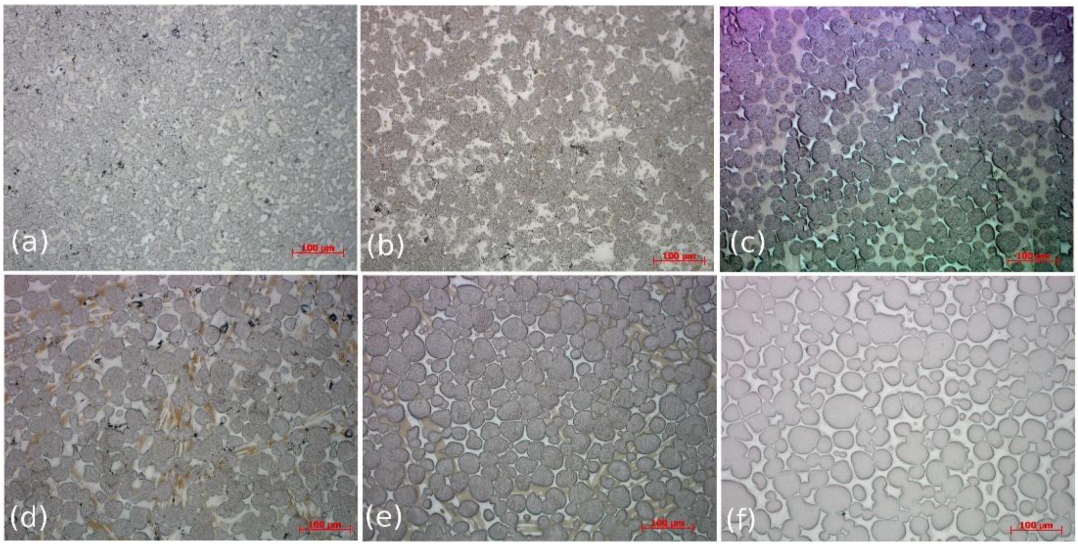

Figure B.2 Optical microstructure images of 0W11 alloy sintered at: a) 1450°C, b) 1475°C, c) 1500°C, d) 1525°C, e) 1550°C, f) 1600°C, 200x

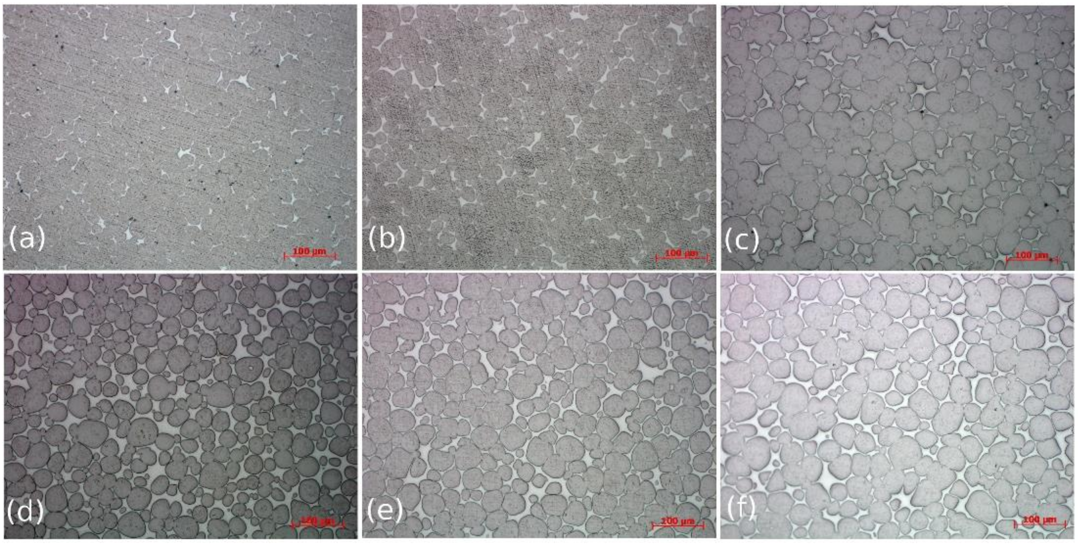

Figure B.3 Optical microstructure images of 0W31 alloy sintered at: a) 1450°C, b) 1475°C, c) 1500°C, d) 1525°C, e) 1550°C, f) 1600°C, 200x

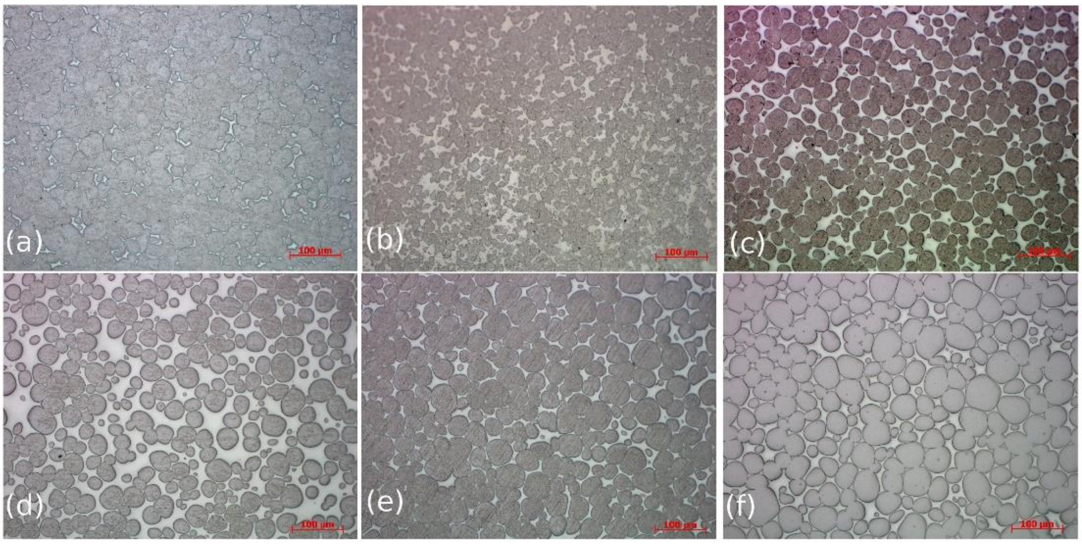

Figure B.4 Optical microstructure images of 0W41 alloy sintered at: a) 1450°C, b) 1475°C, c) 1500°C, d) 1525°C, e) 1550°C, f) 1600°C, 200x

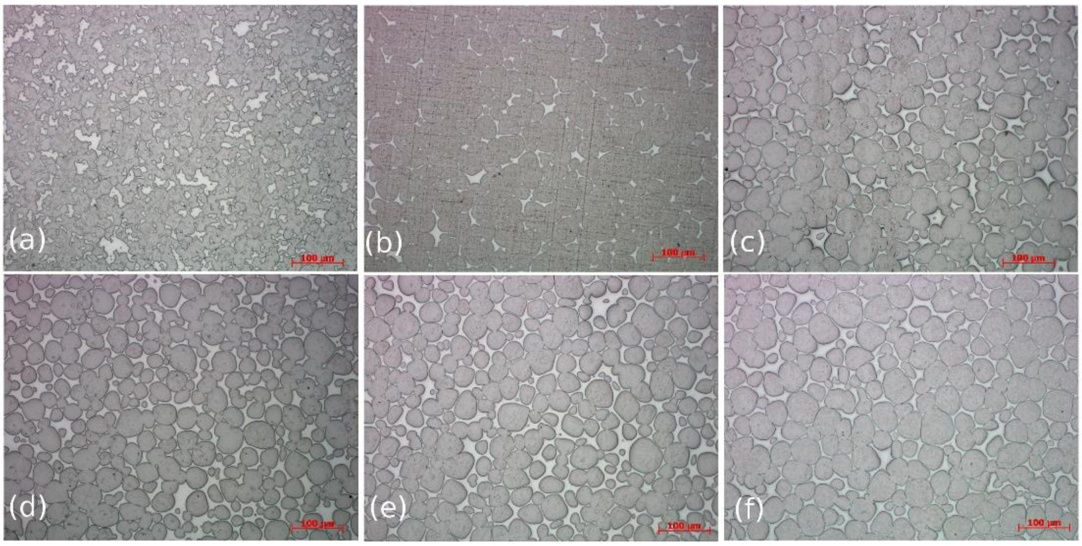

Figure B.5 Optical microstructure images of 0W61 alloy sintered at: a) 1450°C, b) 1475°C, c) 1500°C, d) 1525°C, e) 1550°C, f) 1600°C, 200x

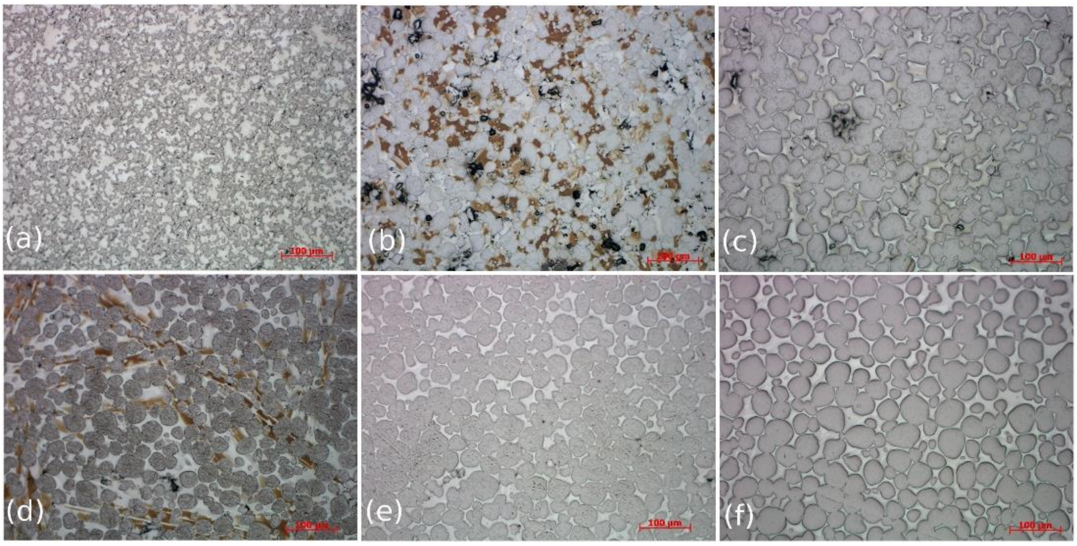

Figure B.6 Optical microstructure images of 2W11 alloy sintered at: a) 1450°C, b) 1475°C, c) 1500°C, d) 1525°C, e) 1550°C, f) 1600°C, 200x

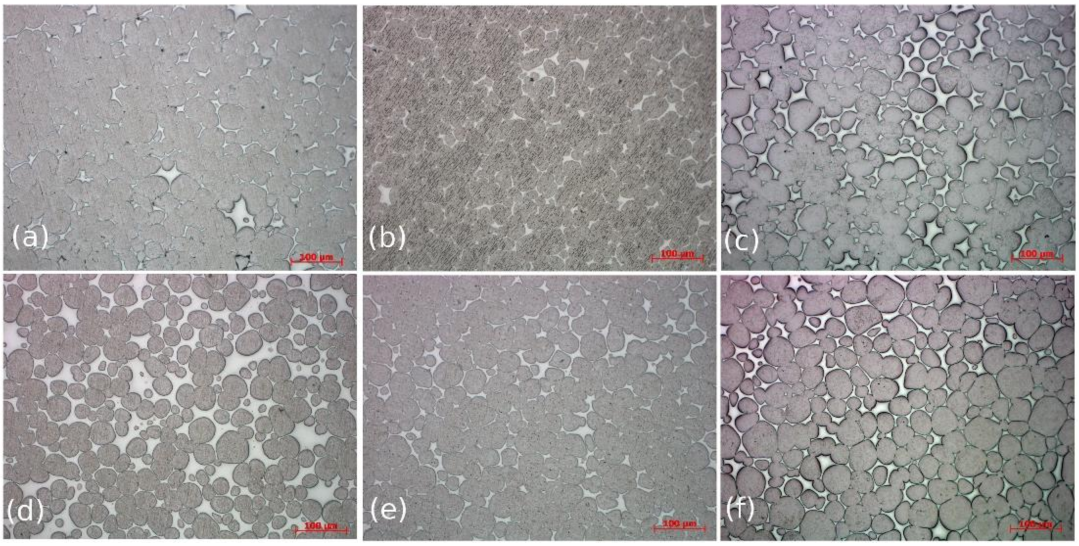

Figure B.7 Optical microstructure images of 2W41 alloy sintered at: a) 1450°C, b) 1475°C, c) 1500°C, d) 1525°C, e) 1550°C, f) 1600°C, 200x

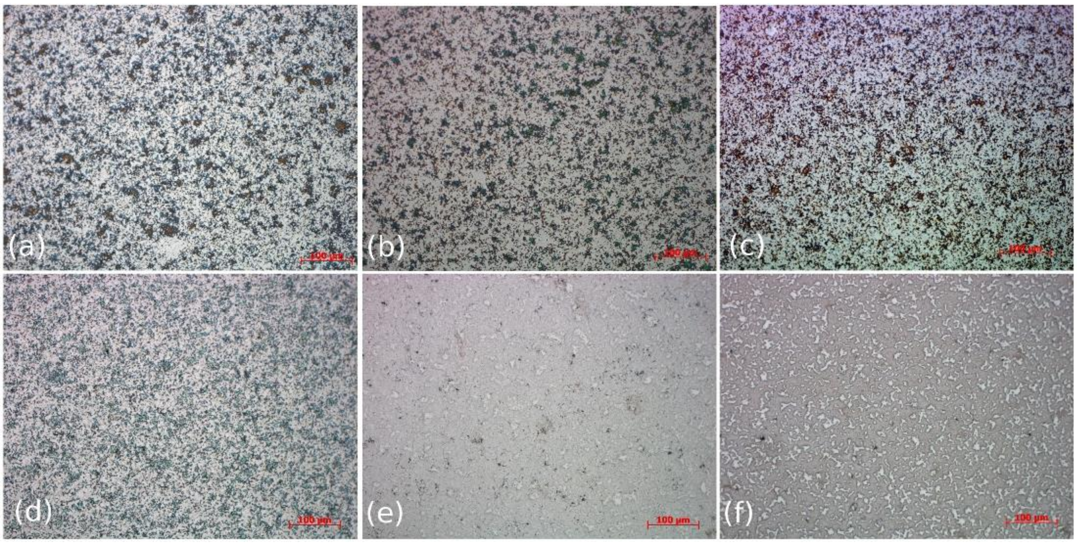

Figure B.8 Optical microstructure images of 5W14 alloy sintered at: a) 1450°C, b) 1475°C, c) 1500°C, d) 1525°C, e) 1550°C, f) 1600°C, 200x

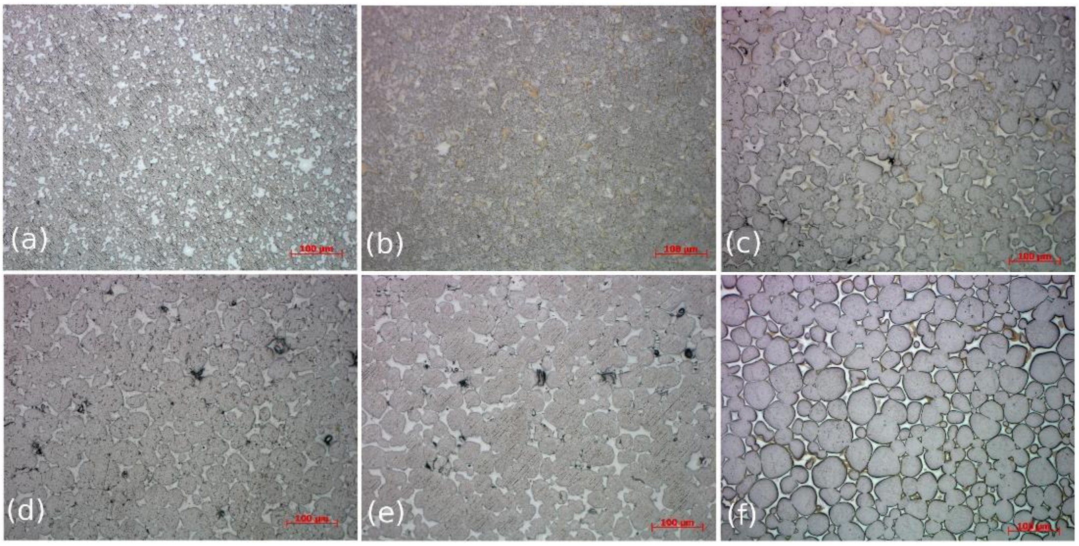

Figure B.9 Optical microstructure images of 5W11 alloy sintered at: a) 1450°C, b) 1475°C, c) 1500°C, d) 1525°C, e) 1550°C, f) 1600°C, 200x

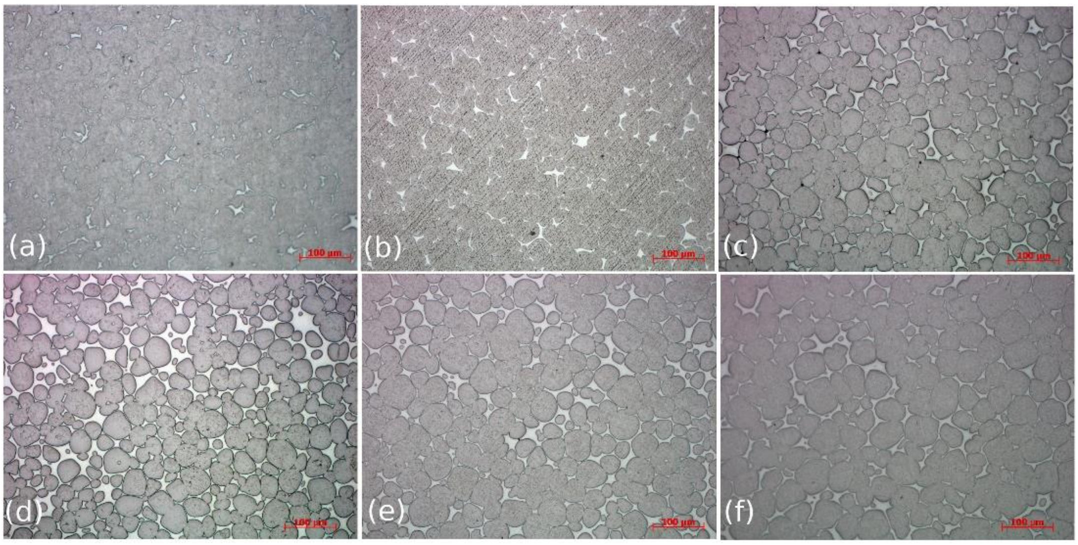

Figure B.10 Optical microstructure images of 5W31 alloy sintered at: a) 1450°C, b) 1475°C, c) 1500°C, d) 1525°C, e) 1550°C, f) 1600°C, 200x

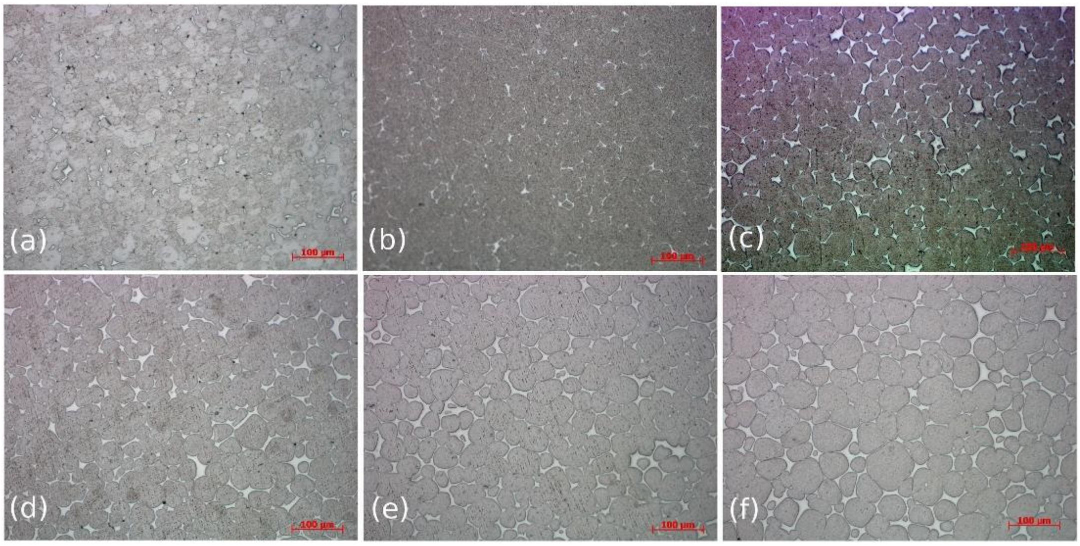

Figure B.11 Optical microstructure images of 5W41 alloy sintered at: a) 1450°C, b) 1475°C, c) 1500°C, d) 1525°C, e) 1550°C, f) 1600°C, 200x

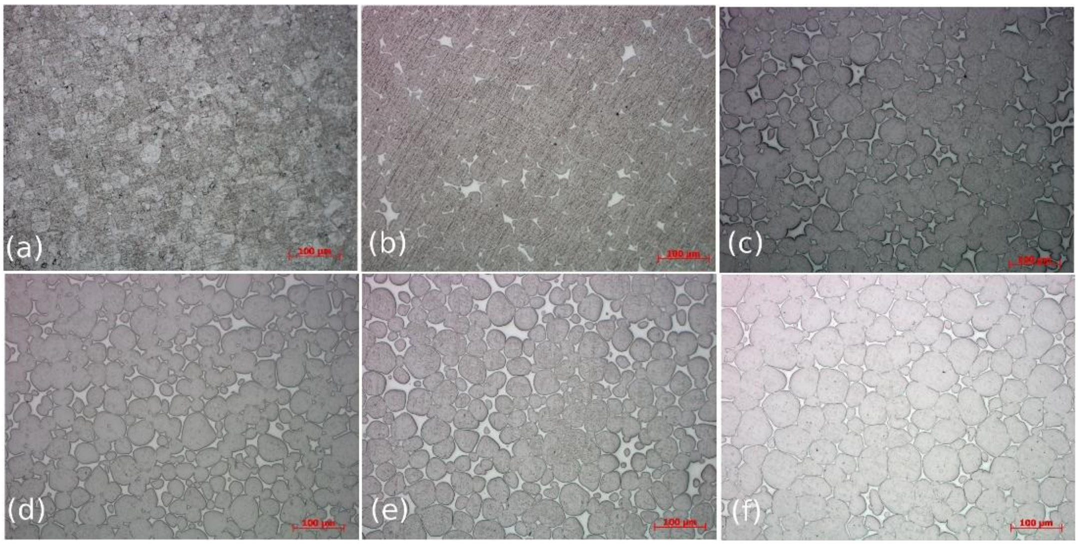

Figure B.12 Optical microstructure images of 5W61 alloy sintered at: a) 1450°C, b) 1475°C, c) 1500°C, d) 1525°C, e) 1550°C, f) 1600°C, 200x

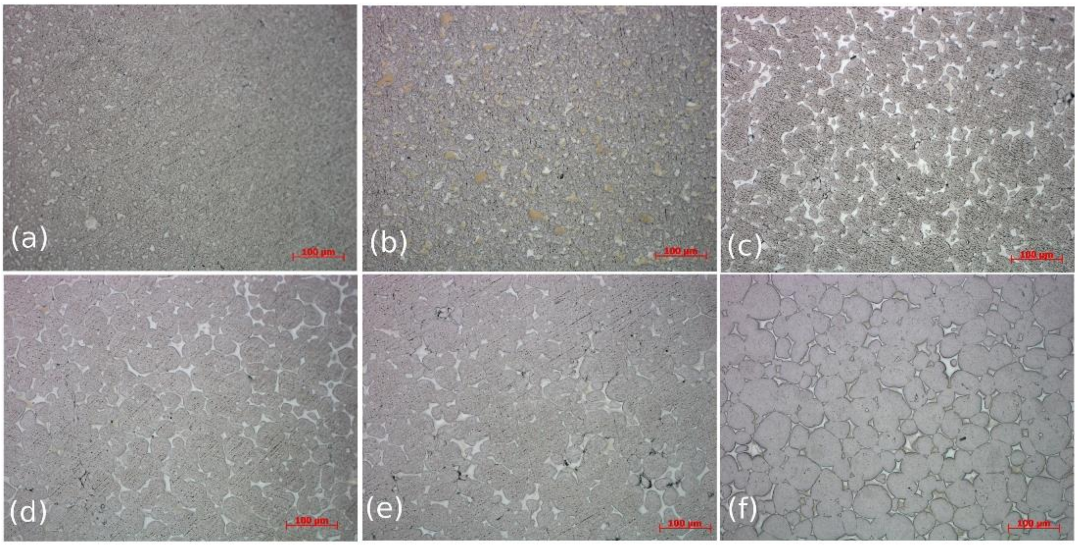

Figure B.13 Optical microstructure images of 7W11 alloy sintered at: a) 1450°C, b) 1475°C, c) 1500°C, d) 1525°C, e) 1550°C, f) 1600°C, 200x

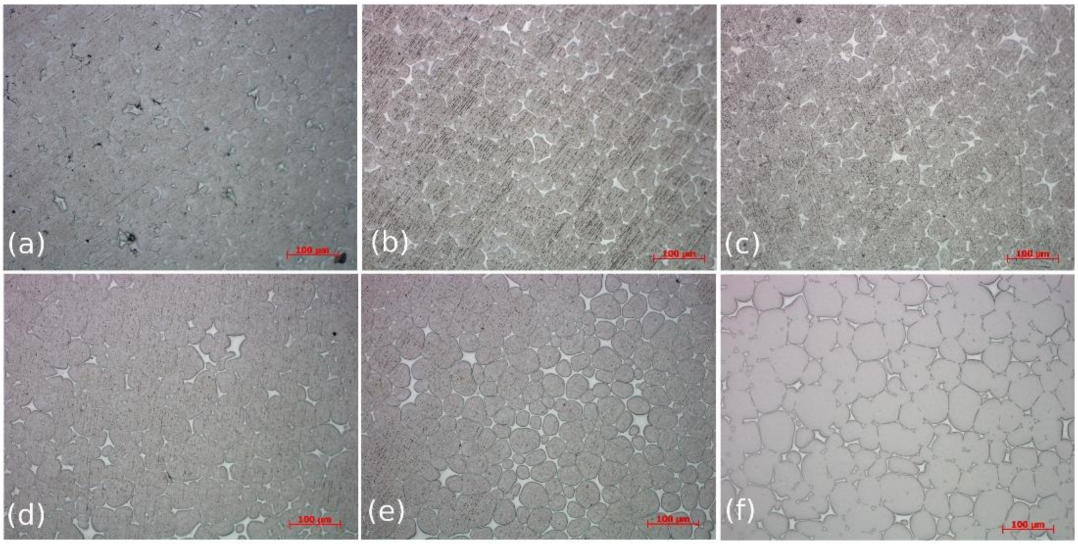

Figure B.14 Optical microstructure images of 7W41 alloy sintered at: a) 1450°C, b) 1475°C, c) 1500°C, d) 1525°C, e) 1550°C, f) 1600°C, 200x

APPENDIX C

BINDER PHASE AREA

Table C.1 Binder Phase Area Measurements for Selected Alloys at Different Sintering Temperature

Alloy Code	**Binder Phase Area (%)**				
	Temperature (°C)				
	1450	**1475**	**1500**	**1550**	**1600**
0W14	-	-	-	-	-
0W11	-	-	-	-	-
0W31	-	11.5	12.9	15.0	14.5
0W41	-	9.4	20.6	13.4	16.1
0W61	-	12.7	14.5	19.1	17.6
2W11	-	-	-	-	-
2W41	-	-	-	-	-
5W14	-	-	-	-	-
5W11	-	-	-	-	-
5W31	-	8.2	11.0	13.6	10.8
5W41	-	5.9	11.3	13.2	14.6
5W61	-	8.5	14.5	12.9	9.8
7W11	-	-	-	-	-
7W41	-	-	-	-	-

APPENDIX D

GRAIN SIZE MEASUREMENTS

Table D.1 Grain Size Measurements for Selected Alloys at Different Sintering Temperature

Alloy Code	Temperature (°C)														
	1475			**1500**			**1525**			**1550**			**1600**		
	AGS Measurements (µm)			**AGS Measurements (µm)**			**AGS Measurements (µm)**			**AGS Measurements (µm)**			**AGS Measurements (µm)**		
0W11	24.6	25.1	24.8	25.3	24.8	25.9	31.8	31.7	31.6	29.3	29.7	29.0	35.5	36.2	35.3
0W31	28.1	29.9	27.9	28.7	29.9	30.3	28.9	29.9	29.9	31.7	31.7	30.5	34.0	34.1	33.3
0W41	24.0	23.3	23,8	26.2	27.3	26.6	28.6	30.0	29.0	29.7	29.8	29.9	32.4	31.8	32.3
0W61	29.3	30.0	30.0	27.8	28.4	28.0	28.3	28.1	28.8	30.9	30.2	30.8	32.6	32.5	32.6
2W11	24.1	23.6	23.2	28.5	29.2	29.0	27.9	28.1	27.8	29.8	29.8	29.9	36.4	35.7	34.8
2W41	28.6	27.9	28.3	30.9	30.0	32.1	30.9	30.7	30.6	30.8	30.9	30.6	32.8	31.9	33.6
5W11	23.3	22.6	23.1	27.7	27.5	27.7	30.2	30.9	30.9	34.4	34.4	33.3	34.0	34.4	34.4
5W31	28.7	27.7	28.4	28.1	27.5	27.7	28.2	28.4	28.7	31.8	31.4	31.4	34.6	35.4	36.0
5W41	24.6	24.0	24.3	27.0	27.4	27.8	30.1	29.8	30.7	31.1	31.1	31.8	35.7	36.0	35.4
5W61	27.4	26.7	27.1	28.0	28.5	27.7	30.0	30.5	29.8	31.4	31.9	31.3	37.9	38.0	38.3
7W11	23.7	22.7	23.4	30.2	29.2	30.0	30.2	31.5	30.0	30.3	29.9	30.8	40.1	37.5	41.0
7W41	29.2	28.5	28.9	31.1	31.3	31.3	32.1	32.5	31.3	31.5	31.6	30.9	39.5	39.4	38.0

APPENDIX E

HARDNESS MEASUREMENTS

Table E.1 Hardness Measurements for Selected Alloys at Different Sintering Temperature

Alloy Code	Temperature (°C)														
	1500					1550					1600				
	Hardness Measurements (HV10)			Average (HV10)	Std. Dev.	Hardness Measurements (HV10)			Average (HV10)	Std. Dev.	Hardness Measurements (HV10)			Average (HV10)	Std. Dev.
0W14	282	244	241	256	23	-	-	-	-	-	-	-	-	-	-
0W11	427	418	418	421	5	505	492	475	491	15	396	412	403	404	8
0W31	331	334	339	335	4	-	-	-	-	-	-	-	-	-	-
0W41	320	326	315	320	6	338	343	334	338	5	312	328	327	322	9
0W61	328	319	344	330	13	-	-	-	-	-	-	-	-	-	-
2W11	430	438	456	441	13	394	424	416	411	16	442	452	452	449	6
2W41	346	360	347	351	8	342	339	339	340	2	324	323	322	323	1
5W14	278	271	275	275	4	-	-	-	-	-	-	-	-	-	-
5W11	392	404	422	406	15	420	416	406	414	7	396	392	394	394	2
5W31	330	340	336	335	5	-	-	-	-	-	-	-	-	-	-
5W41	326	320	331	326	6	341	336	326	334	8	315	328	329	324	8
5W61	336	342	337	338	3	-	-	-	-	-	-	-	-	-	-
7W11	390	402	393	395	6	391	378	387	385	7	368	368	371	369	2
7W41	358	363	370	364	6	329	330	338	332	5	344	335	335	338	5

APPENDIX F

MULTIPLE REGRESSION STUDIES

Table F.1 AGS, Composition, Sintering Temperature, % Relative Density, % W in Binder Phase and % Binder Matrix Area Data for 90% W Ni-rich Alloys

90% W (wt%)					
y	X_1	X_2	X_3	X_4	X_5
Average Grain Size (micron)	Composition % Ni content (wt%)	Temperature (K)	Relative Density (%)	W in Binder phase (wt %)	Binder matrix area (%)
28.6	7.5	1748.0	99.5	39.1	11.5
29.6	7.5	1773.0	99.3	38.9	12.9
29.6	7.5	1798.0	100.0	43.1	21.7
31.3	7.5	1823.0	99.9	42.2	15.0
33.8	7.5	1873.0	99.2	41.1	14.5
24.0	8.0	1748.0	99.2	39.3	9.4
26.7	8.0	1773.0	97.1	39.6	20.6
29.2	8.0	1798.0	98.4	36.7	23.2
29.8	8.0	1823.0	99.6	39.6	13.4
32.2	8.0	1873.0	100.0	42.1	16.1
29.8	8.6	1748.0	99.7	38.6	12.7
28.1	8.6	1773.0	99.2	38.1	14.5
28.4	8.6	1798.0	99.9	41.1	19.1
30.6	8.6	1823.0	99.9	40.2	19.1
32.6	8.6	1873.0	99.0	39.9	17.6

Table F.2 AGS, Composition, Sintering Temperature, % Relative Density, % W in Binder Phase and % Binder Matrix Area Data for 95% W Ni-Rich Alloys

95% W (wt%)					
y	X_1	X_2	X_3	X_4	X_5
Average Grain Size (micron)	Composition % Ni content (wt%)	Temperature (K)	Relative Density (%)	W in Binder phase (wt %)	Binder matrix area (%)
28.3	3.75	1748.0	99.4	38.7	8.2
27.8	3.75	1773.0	99.2	35.9	11.0
28.4	3.75	1798.0	100.0	40.6	15.6
31.5	3.75	1823.0	99.8	41.3	13.6
35.3	3.75	1873.0	99.7	41.5	10.8
24.6	4.0	1748.0	97.1	36.8	5.9
27.4	4.0	1773.0	99.9	38.9	11.3
30.2	4.0	1798.0	98.8	33.0	15.0
31.3	4.0	1823.0	99.4	42.1	13.2
35.7	4.0	1873.0	99.8	42.8	14.6
27.4	4.3	1748.0	99.5	35.5	8.5
28.1	4.3	1773.0	99.4	36.2	14.5
30.1	4.3	1798.0	99.9	41.6	14.8
31.5	4.3	1823.0	99.8	41.1	12.9
38.1	4.3	1873.0	99.2	41.9	9.8

Table F.3 Non-Dimensional Normalized AGS, Composition, Sintering Temperature, % Relative Density, % W in Binder Phase and % Binder Matrix Area Data for 90% W Ni-rich Alloys

90% W (wt%)					
Non-dimensional normalized					
y	X_1	X_2	X_3	X_4	X_5
Average Grain Size	Composition % Ni content	Temperature	Relative Density	W in Binder phase	Binder matrix area
-0.4215	-1.14578	-1.23536	0.22775	-0.52639	-1.14734
-0.00826	-1.14578	-0.67384	-0.03504	-0.61983	-0.79713
-0.00826	-1.14578	-0.11231	0.88471	1.83302	1.40416
0.69424	-1.14578	0.44922	0.75332	1.32493	-0.27183
1.72733	-1.14578	1.57228	-0.16643	0.67084	-0.3969
-2.32239	-0.07161	-1.23536	-0.16643	-0.40375	-1.67265
-1.20665	-0.07161	-0.67384	-2.92568	-0.23438	1.129
-0.17356	-0.07161	-0.11231	-1.21757	-1.89882	1.77938
0.07438	-0.07161	0.44922	0.35914	-0.23438	-0.67206
1.06615	-0.07161	1.57228	0.88471	1.25485	0.00334
0.07438	1.2174	-1.23536	0.49053	-0.8184	-0.84716
-0.62812	1.2174	-0.67384	-0.16643	-1.0812	-0.3969
-0.50415	1.2174	-0.11231	0.75332	0.68252	0.75378
0.40497	1.2174	0.44922	0.75332	0.11018	0.75378
1.23145	1.2174	1.57228	-0.42922	-0.05918	0.37856

Table F.4 Non-Dimensional Normalized AGS, Composition, Sintering Temperature, % Relative Density, % W in Binder Phase and % Binder Matrix Area Data for 95% W Ni-rich Alloys

95% W (wt%)					
Non-dimensional normalized					
y	X_1	X_2	X_3	X_4	X_5
Average Grain Size	Composition % Ni content	Temperature	Relative Density	W in Binder phase	Binder matrix area
-0.56936	-1.14578	-1.23536	0.00932	-0.15089	-1.29498
-0.70623	-1.14578	-0.67384	-0.27017	-1.09199	-0.33574
-0.54199	-1.14578	-0.11231	0.84776	0.45221	1.24017
0.30658	-1.14578	0.44922	0.56828	0.71069	0.55499
1.34676	-1.14578	1.57228	0.42854	0.76039	-0.40425
-1.58217	-0.07161	-1.23536	-3.20473	-0.80038	-2.08294
-0.81572	-0.07161	-0.67384	0.70802	-0.09455	-0.23296
-0.04927	-0.07161	-0.11231	-0.82913	-2.0596	1.03462
0.25183	-0.07161	0.44922	0.00932	0.9559	0.41796
1.45625	-0.07161	1.57228	0.56828	1.20112	0.89758
-0.81572	1.2174	-1.23536	0.14906	-1.2146	-1.19221
-0.62411	1.2174	-0.67384	0.00932	-0.97932	0.86332
-0.07664	1.2174	-0.11231	0.70802	0.80678	0.9661
0.30658	1.2174	0.44922	0.56828	0.62453	0.31518
2.11321	1.2174	1.57228	-0.27017	0.87969	-0.74684

Table F.5 Multiple Regression Analysis Data for 90% W Ni-Rich Alloys

Model Summary										
Model	R	R Square	Adjusted R Square	Std. Error of the Estimate	Change Statistics					Durbin-Watson
					R Square Change	F Change	df1	df2	Sig. F Change	
1	0.865	0.747	0.621	0.59463788	0.747	5.919	5	10	0.008	2.332

Coefficient						
Model		Unstandardized Coefficients		Standardized Coefficients	t	Sig.
		B	Std. Error	Beta		
1	Composition %Ni Content	-0.177	0.174	-0.177	-1.014	0.335
	Temperature	0.883	0.190	0.883	4.659	0.001
	Relative Density	0.300	0.199	0.300	1.509	0.162
	W in Binder Phase	-0.250	0.226	-0.250	-1.105	0.295
	Binder Matrix Area	0.013	0.173	0.013	0.075	0.941

Table F.5 Continued

Model		Sum of Squares	df	Mean Square	F	Sig.
1	Regression	10.528	5	2.106	6.064	0.008[c]
	Residual	3.472	10	0.347		
	Total	14.000	15			

Table F.6 Multiple Regression Analysis Data for 95% W Ni-Rich Alloys

Model Summary				
Model	R	R Square	Adjusted R Square	Std. Error of the Estimate
1	0.973^a	0.946	0.919	0.27502254

Coefficient							
Model		Unstandardized Coefficients		Standardized Coefficients	t	Sig.	
		B	Std. Error	Beta			
1	Composition %Ni Content	0.101	0.074	0.101	1.372	0.200	
	Temperature	1.068	0.109	1.068	9.767	0.000	
	Relative Density	0.204	0.104	0.204	1.958	0.079	
	W in Binder Phase	-0.150	0.115	-0.150	-1.309	0.220	
	Binder Matrix Area	-0.232	0.098	-0.232	-2.358	0.040	

Table F.6 Continued

Model		Sum of Squares	df	Mean Square	F	Sig.
1	Regression	13.244	5	2.649	35.019	0.000
	Residual	0.756	10	0.076		
	Total	14.000	15			